Characterizing Habitable Environments on Mars Using Infrared Spectroscopy from Orbit

Elena Sophia Amador

A dissertation

submitted in partial fulfillment of the

requirements for the degree of

Doctor of Philosophy

University of Washington

2017

Reading Committee:

Joshua L. Bandfield, Chair

David C. Catling

Victoria S. Meadows

Program Authorized to Offer Degree:

Earth and Space Sciences

University of Washington

Abstract

Characterizing Habitable Environments on Mars using Infrared Spectroscopy from Orbit

Elena Sophia Amador

Chair of the Supervisory Committee:
Dr. Joshua L. Bandfield
Department of Earth and Space Sciences

Until recently, the search for habitable environments on Mars has mostly been driven by the motto “follow the water”, as water is thought to be one of the fundamental requirements for life. Over the last several decades, there has been abundant geomorphic and mineralogical evidence for surface and near-surface liquid water early in Mars’ history, increasing the potential for past habitable environments. However, it has becoming progressively clear that there are several more requirements, in addition to liquid water, that make an environment habitable including a source of energy for biochemical processes, major and trace elements to form macromolecules (e.g., CHNOPS), as well as clement physicochemical conditions (e.g., pH, salinity, temperature). The search for habitable environments on Mars has now become more

refined, searching for locales that show evidence for not only liquid water, but these other important constraints.

This dissertation first focuses on the Nili Fossae region of Mars, an area that shows extensive evidence for aqueous alteration with a diverse range of hydrated minerals. This work views the region through the lens of both bulk surface composition and secondary alteration minerals, in particular with respect to minerals that would indicate not only liquid water but an energy source and a means for creating organic materials, such as with serpentinization. The study ultimately uses what is learned in Nili Fossae to better understand the global distribution of mineralogical evidence for serpentinizing systems detectable from available orbital data. The studies presented here rely on near-infrared (~1.0-3.0 µm) reflectance and thermal-infrared (~5-50 µm) emissivity measurements of both the martian surface and terrestrial analog materials to best describe the composition of surfaces exposed in Nili Fossae.

Chapter Two uses a complementary approach for looking at near- and thermal-infrared measurements of the surfaces in Nili Fossae to identify elevated bulk-silica exposures that imply increased aqueous alteration of a capping unit that was previously considered unaltered. This extends aqueous alteration to all three major stratigraphic units in the area. *Chapter Three* uses near- and thermal-infrared laboratory measurements of rocks from the Lost City Hydrothermal Field on Earth to better constrain the geochemical and astrobiological environment that formed similar minerals in Nili Fossae, Mars. This work identified a suite of spectral types and minerals (serpentine, Mg-carbonate, and talc/saponite) associated with low-temperature serpentinizing systems on Earth and compared them to what was observed in Nili Fossae. This resulted in an additional identification of serpentine within the region, and additional evidence for a sustained habitable serpentinizing system in Nili Fossae. This framework was used to search for similar sites across Mars in *Chapter Four*. This produced a global map of the distribution of spectral types associated with low-temperature serpentinizing systems. This study resulted in new identifications of serpentine across the southern highlands, predominately in isolated exposures in crater and valley walls, crater ejecta and ancient knobby terrains. Additionally, it found that serpentine was much more pervasive in the Nili Fossae region than previously thought, making it an increasingly compelling site for future detailed surface investigations with respect to habitability.

TABLE OF CONTENTS

LIST OF FIGURES

LIST OF TABLES

ACKNOWLEDGEMENTS

It really does take a village to make a planetary scientist so I will do my best to thank all those who have helped me along this journey.

First, I want to express my deepest gratitude to Josh Bandfield for taking me on as a graduate student, and teaching me how to think critically about spacecraft data and planetary science in general. I would not have been able to finish my dissertation without your *patient* guidance and support.

Thank you to my committee, Victoria Meadows, David Catling, and Darlene Zabowski. Thank you for always having your doors open, especially as the planetary remote sensing group was shrinking at UW. Additionally, there were several others who aided in the scientific content of this dissertation: Billy Brazelton and Deborah Kelley for providing Lost City Hydrothermal Field samples and teaching me about terrestrial serpentinization, and of course Bernard Evans for explaining all the mineralogical details involved in serpentinization.

I also must thank those who encouraged me to pursue planetary science when I was an undergraduate student. Dr. Janice Bishop at the SETI Institute introduced me to CRISM data and near-infrared spectroscopy. Thank you to Dr. Carl Allen and Dr. Dorothy Oeheler at NASA Johnson Space Center for an incredible undergraduate research experience and project. Thank you to the UC Santa Cruz Earth and Planetary Science faculty who first introduced me to planetary geology, in particular professors Francis Nimmo and Erik Asphaug. There were several others who encouraged me at a young age to pursue planetary exploration: Jim Erickson, Bonnie Buratti, and Eleanor Basilio at the Jet Propulsion Laboratory.

Thank you to the Department of Earth and Space Sciences for providing funding for my graduate studies and an inclusive atmosphere over the years. I'd like to especially thank those who worked "behind the scenes" to keep this department running so smoothly: Eunice Yang, Kathy Gabriel, Lauren McOwen Wood, Noéll Bernard-Kingsley, Nathan Briley, Ed Mulligan, Dave McDougall, Sue Bernhardt, and I've probably missed others but you've made this process as painless as possible.

Thank you to the UW Astrobiology Program. This program has kept me sane during my graduate career. The opportunities given to me because of UW Astrobiology are unmatched at any other university. I’ve been from Iceland to Hawaii to the Rio Tinto in Spain, thanks to the AB program. Woody Sullivan told us that when we left this program we would be able to a) sit through and comprehend any seminar related to astrobiology from microbiology all the way to astrophysics and b) that we would have a unique perspective and look at planetary problems in a whole new way. Well, he was right, and only a program like this could have accomplished that. Additionally, I have to specifically call out Victoria Meadows for being our fearless director. Thank you Vikki, for guiding this program and creating an environment that we the graduate students could really take ownership of. You’ve treated us as colleagues rather than students and we will remember that when we are mentors to future students.

Special shout out to my FELDSPAR Iceland colleagues. We were a rag-tag group of early-career scientists who just wouldn’t quit. Thank you for the wonderful science and most importantly all the laughs.

Thank you to all my friends I’ve made over the years at UW and in Seattle. We have had a lot of fun and I will miss the community that we have built. I’d especially like to thank Topher French and Marty McFly for the nonstop adventures, love, and kindness. I cannot wait to see what California has in store for us – in particular, sunshine and burritos.

Last but certainly not least, thank you to my incredible family. Thank you to my beautiful sister Sarah, for “jaws” being incredibly patient with me, always letting me talk first (and last), and always being there for me when I need you. Thank you to my intelligent mother Begoña, for teaching me to be tough and stand my ground, how to manage a budget, and always being available to talk on the phone when I’m waiting at a bus-stop. Thank you to my inspiring father Arthur, for teaching me about the Universe. The three of you have encouraged and supported me my entire life, and we’ve been *mostly* laughing the whole way.

DEDICATION

To my sister, Sarah,

and my parents, Begoña and Arthur

Chapter 1. **INTRODUCTION**

1.1 ORGANIZATION OF DISSERTATION

This introductory chapter contains a brief overview of the motivation for my dissertation work. Chapters 2 through 4 of the dissertation have been written as stand-alone papers; as such each chapter contains a detailed introduction with a thorough literature review. The second chapter "**Elevated bulk-silica exposures and evidence for multiple aqueous alteration episodes in Nili Fossae, Mars**" was published in the journal *Icarus* in the spring of 2016. The third chapter "**The Lost City Hydrothermal Field: A spectroscopic and astrobiological analog for Nili Fossae, Mars**" was submitted to the journal *Astrobiology* in October 2016, and was returned with "minor revisions" in December 2016 and a revised manuscript will be submitted to the editor in February 2017. The fourth chapter "**A search for minerals associated with serpentinization across Mars using CRISM spectral data**" will be submitted to the journal *Icarus* during Winter Quarter 2017. A bibliography of all references within all chapters can be found at the end of the dissertation**.**

1.2 MOTIVATION

One of the main motivations driving planetary exploration today is to understand the range of geologic and geochemical environments found across our Solar System, throughout its history. The underlying questions behind this motivation are: Under which geologic conditions did life evolve on Earth? Did other planetary bodies experience similar geologic constraints? And ultimately, could (or did) life ever arise outside of the Earth? Scientific attention has been particularly placed on constraining the evolution of Mars for several reasons, including its similarity in geologic features to Earth, its strong evidence for past surface liquid water (e.g., Poulet et al., 2005; Hynek et al., 2010), and its proximity to the Earth aiding in the timely exploration and turn-around time between exploration missions.

Geomorphic and mineralogical observations of the martian surface over the last several decades have taught scientists that Mars has undergone a series of transient, or potentially sustained, periods of surface and near-surface liquid water (e.g., Ehlmann and Edwards, 2014). And though as a whole the martian surface is primarily composed of unaltered basalt, it is becoming clear from the increasing return of data from planetary exploration missions, that at the regional and local scale, the martian surface can have a wide range of primary and secondary alteration minerals (Ehlmann and Edwards, 2014), implying more sustained and localized aqueous environments. These sites that show evidence for sustained aqueous alteration are compelling for the study of astrobiology, as they may preserve evidence for putative martian life, or conversely they may provide important clues for why life may not have formed on Mars.

The study of martian surface mineralogy and rock composition can be extremely powerful tools for understanding the environmental, geochemical, and global conditions on Mars, as many minerals are diagnostic of specific conditions. Even more illuminating is the variation of mineralogical alteration suites across the planet and their association to the surrounding, unaltered source rock. The ability to place the alteration products in the context of bulk surface composition is a powerful means of constraining the duration, intensity, and type of aqueous alteration of the surface and subsurface while revealing specific chemical pathways available as an energy source for potential microbial life in Mars' past.

This dissertation work focused on studying Mars from the perspective of surface composition and mineralogy, specifically as it related to habitability. The work was predominantly concentrated in the Nili Fossae region of Mars, an area that has been studied extensively because of its unique and rich mineralogical diversity (detailed description of the geologic setting in Section 2.1.1). However, the work presented here used newly applied data analysis techniques and viewed the region through the lens of terrestrial sites of astrobiological importance. Additionally, this work sought to use what was learned about the past habitability and mineralogy in Nili Fossae to better understand the potential for similar sites across the planet. Finally, a major component of each chapter presented in this dissertation was using acquired spectroscopic measurements of either Mars or terrestrial field samples, in new and often more comprehensive ways. This allowed the problem, or question being asked, to be approached in a different way, often more completely.

In **Chapter 2**, we created “weighted absorption center” index maps from thermal-infrared THEMIS (Thermal Emission Imaging System) multispectral data to visually display the relative bulk-silica content across the Nili Fossae. By doing this, we could identify elevated bulk-silica units that would have otherwise gone undetected using traditional analysis techniques. In this chapter, we also systematically compared thermal- and near-infrared spectroscopic datasets that provide complementary but different information about the surface. Similarly, by using the two datasets collaboratively, we could make mineralogical interpretations that would have been missed by any one dataset use alone. In **Chapter 3**, we measured the thermal-infrared emissivity and near-infrared reflectance of terrestrial rock samples from a serpentinizing system. These specific measurement techniques were used to not only assess the mineralogical composition and variability found in these samples, but to do so with techniques comparable to those on past, current, and future spacecraft. Lastly, in **Chapter 4**, we applied factor analysis and target transformation techniques to CRISM (Compact Reconnaissance Imaging Spectrometer for Mars) near-infrared spectral data to search for spectral evidence for serpentinization across Mars. This approach allowed us to look through >10,000 CRISM images in a timely and quantitative manner, and search for the subtle and weak spectral absorptions associated with serpentine that can be missed with traditional analysis techniques.

Chapter 2. **ELEVATED BULK-SILICA EXPOSURES AND EVIDENCE FOR MULTIPLE AQUEOUS ALTERATION EPISODES IN NILI FOSSAE, MARS**

Originally published in the journal Icarus
Elena S. Amador and Joshua L. Bandfield, 2016. Elevated bulk-silica exposures and evidence for multiple episodes of aqueous alteration in Nili Fossae, Mars. *Icarus,* 276, 39-51, doi:10.1016/j.icarus.2016.04.015

2.1 INTRODUCTION

Spectrometers on orbital spacecraft around Mars inform our understanding of the mineral composition of the upper few microns to tens of microns of the martian surface. This mineralogy provides a record of the geochemical conditions present during the time of formation and allows past environmental conditions to be ascertained, especially when local mineralogies are investigated with respect to regional compositions and geologic context. Orbital spectroscopy has been used extensively to identify regional surface mineralogy on Mars and given that specific wavelength regions are sensitive to different phases; a combined analysis can lead to a more comprehensive view of the surface.

This study focuses predominately on spectral data acquired by the 2001 Mars Odyssey Thermal Emission Imaging System (THEMIS; Christensen et al., 2004) and the Compact Reconnaissance Imaging Spectrometer for Mars (CRISM; Murchie et al., 2007) on the Mars Reconnaissance Orbiter (MRO). The combined wavelength coverage from CRISM and THEMIS allows for the characterization of both bulk surface compositions and the identification of secondary alteration products.

This study has two goals:

1) To introduce a detailed and systematic approach to analyzing near-infrared CRISM and thermal-infrared THEMIS spectral datasets in a complementary fashion, including the applicability of using a new index map, the “weighted absorption center”, as a tool for the reconnaissance of THEMIS images with elevated bulk-silica compositions. We use Nili Fossae as the test locale for this approach given its high mineralogical diversity.

2) To document the presence of elevated bulk-silica exposures in the Nili Fossae region. These newly observed exposures are associated with local olivine-rich basalts and phyllosilicate-bearing basalts but are not spatially co-located with either unit. The units likely represent a period of aqueous activity in Nili Fossae, separate from that which formed the previously identified phyllosilicates.

2.1.1 Geologic Setting

The Nili Fossae are a set of concentric graben surrounding the north-west rim of the Isidis impact basin (Schultz and Frey, 1990) and likely formed due to mass unloading and flexure associated with the Isidis impact event that occurred approximately 4 Ga (Wichman and Schultz, 1989) (**Figure 2.1**). Apart from the early Hesperian-aged flood basalts from Syrtis Major that inundate the floor of the Nili Fossae trough (Hiesinger and Head, 2004) the fossae provide a rare glimpse into Mars' geologic and geochemical past with extensive exposures of Noachian crustal materials. The fractures themselves, local impact craters, as well as the relatively low dust cover (Ruff and Christensen, 2002), reveal compositionally heterogeneous exposures that can be spatially resolved from orbit. The diverse surface compositions and alteration products found in Nili Fossae imply unique igneous activity during the region's history in addition to multiple phases of aqueous alteration (e.g, Hoefen et al., 2003, Hamilton and Christensen, 2005; Poulet et al., 2005; Bibring et al., 2006; Mangold et al., 2007; Mustard et al., 2007, 2009; Ehlmann et al., 2008, 2009, 2010; Tornabene et al., 2008; Brown et al., 2010; Viviano et al., 2013; Edwards and Ehlmann, 2015).

The basement rock in the region is described as a massive to brecciated basalt with localized signatures of Fe/Mg-smectite, likely due to subsurface aqueous alteration prior to the Isidis impact event (e.g., Poulet et al., 2005; Bibring et al., 2006; Mangold et al., 2007; Mustard et al., 2007; Ehlmann et al., 2009). Alternatively, the Fe/Mg-smectites may have formed syn-/post-Isidis impact from ground water circulation (Viviano et al., 2013). An olivine-rich basalt unit is primarily exposed in the eastern portion of the Nili Fossae troughs, stratigraphically above the

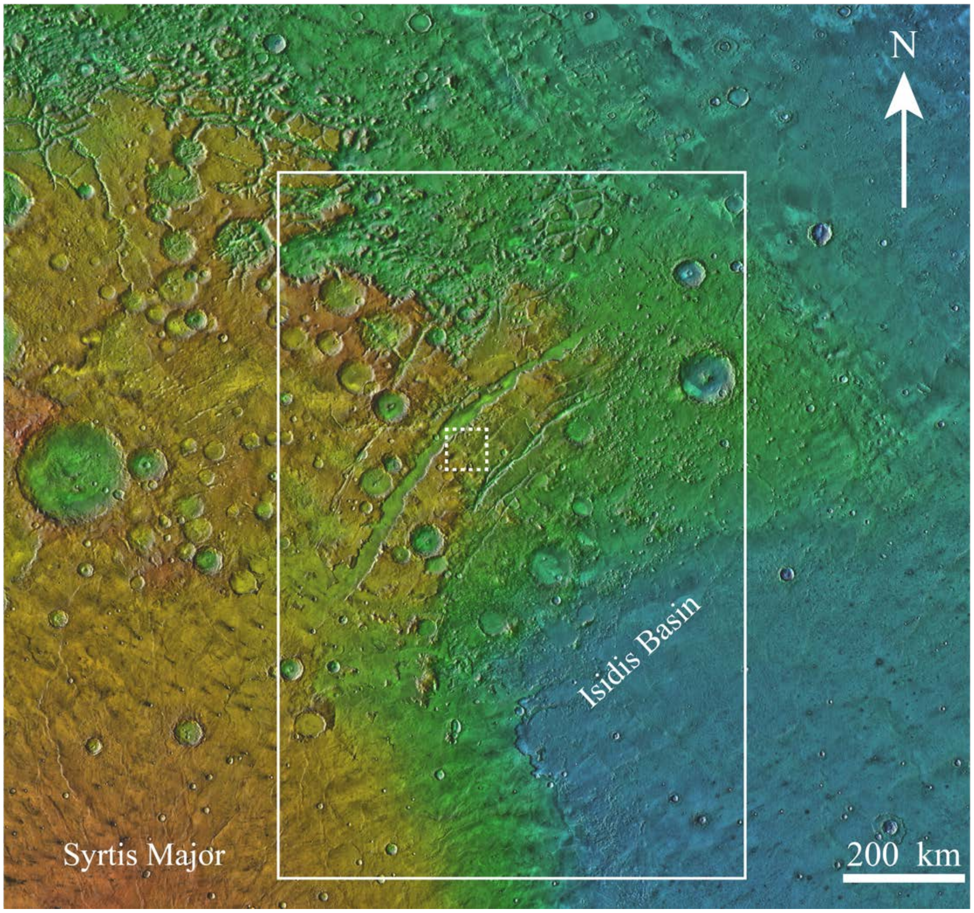

Figure 2.1. Nilo-Syrtis Major colorized elevation map with THEMIS Global Day IR mosaic used for shading. Solid white box indicates initial THEMIS image search area. Dashed white box indicates area covered by **Figure 2.10**. Image is centered around 77.02ºE and 21.86 ºN.

Noachian basement unit (Hoefen et al., 2003; Hamilton and Christensen, 2005; Mustard et al., 2007; Tornabene et al., 2008). Quantitative deconvolution analyses of emission spectra from the Mars Global Surveyor (MGS) Thermal Emission Spectrometer (TES) have shown that this basalt contains between 20 and 30 wt% olivine with olivine compositions ranging from Fo_{68-75} (Hamilton and Christensen, 2005; Koeppen and Hamilton, 2008; Edwards and Ehlmann, 2015). The olivine-rich unit appears to drape pre-existing topography and may have formed as a post-Isidis impact melt sheet (Mustard et al., 2009), or post-Isidis volcanic lava flows (Hamilton and Christensen, 2005; Tornabene et al., 2008). Isolated locations of the olivine-rich basalt have subsequently been variably altered to Fe/Mg-carbonates (Ehlmann et al., 2008, 2009; Edwards and Ehlmann, 2015), Mg-serpentine (Ehlmann et al., 2009, 2010), and talc and/or saponite (Brown et al., 2010; Viviano et al., 2013). The presence of these mineral phases has been attributed to localized hydrothermal alteration of both the underlying Fe/Mg-smectites and the olivine-bearing basalt during the emplacement of Hesperian aged lava flows (e.g., Viviano et al, 2013).

Both the northeastern and northwestern portions of Nili Fossae are capped by an olivine-poor basalt (e.g., Tornabene et al., 2008; Mustard et al., 2009). The source of this basalt is still debated, though Mustard et al. (2009) hypothesize that it may represent the upper (less dense) portion of the impact melt sheet that formed the olivine-rich basalt unit. More recently, Edwards and Ehlmann (2015) proposed that the capping unit may be an eroded volcanic ash based on Hapke modeling of single scattering albedo from CRISM data and low thermal-inertia values derived from THEMIS observations, in addition to observed composition and morphology. This is similar to work presented by Bandfield et al. (2013a) who argued that much of Mars' older surfaces are composed of relatively friable volcanic ash of a basaltic composition. The region also shows evidence for reworking by late Noachian/early Hesperian fluvial activity, based on the presence of channel networks (e.g., Ehlmann et al., 2009). The fluvial activity likely led to the transport and re-emplacement of Fe/Mg-smectites into fan deposits (e.g., Ehlmann et al., 2009).

2.2 DATA AND METHODS

To determine the surface composition of exposures of interest in Nili Fossae, we incorporated both near-infrared (NIR; defined here as ~ 1.0 – 3.0 µm) and thermal-infrared (TIR; ~ 5.0 – 50.0 µm) spectral datasets that provide highly complementary information based on their specific sensitivities. When present as coarse particulates, TIR spectral measurements are sensitive to the major phases present and the bulk-rock compositions (e.g., Thomson and Salisbury, 1993; Ramsey and Christensen, 1998; Smith et al., 2013). NIR spectral measurements are sensitive to hydrated and Fe-bearing phases (e.g., Hunt, 1977). This property allows for the detection of specific phases, even when present only as minor constituents, although it can be difficult to retrieve quantitative mineral abundance information from the NIR spectra (e.g., Hunt, 1977). In-depth examination of both NIR and TIR wavelength regions can reveal details that might be otherwise missed by the investigation of either dataset alone. Here, we present an updated TIR data analysis technique and a new approach to comparing the two wavelength regions in a complementary fashion.

2.2.1 Thermal Emission Imaging System (THEMIS)

THEMIS multispectral thermal-infrared data can be used to understand the bulk mineralogy of martian surfaces (e.g., Huang et al., 2013; Edwards and Ehlmann, 2015). We applied several analysis techniques to the THEMIS data. Decorrelation stretch image products were first used as a preliminary survey tool to obtain a broad understanding of the variability in rock composition within the region (e.g., Bandfield et al., 2004a). Similarly, colorized index images mapping the weighted absorption center (WAC), or “center of gravity” (e.g., Smith et al., 2013), of THEMIS emissivity spectra were produced and used to infer the variability in bulk-silica abundance (Smith et al., 2013). Based on the regions of interest identified from the broad survey products, a more detailed analysis of emissivity spectra from individual locations was conducted using the atmospherically corrected images.

2.2.1.1 Introduction to data and atmospheric corrections

THEMIS is a multi-spectral visible, near-infrared, and thermal-infrared imager on the 2001 Mars Odyssey spacecraft. The imager has 10 thermal-infrared spectral channels spaced between 6.5 and 15 μm (**Table 2.1**) with a spatial sampling of ~100 meters/pixel and a swath width of 32 km collected from the orbital height of ~420 km. The thermal-infrared component of THEMIS consists of an uncooled 320 by 240 element microbolometer array that produces calibrated radiance images using an internal calibration flag and instrument response functions determined from pre-launch data. Further description regarding calibration and data processing procedures and errors are detailed by Bandfield et al., (2004b), Christensen et al., (2004) and Edwards et al., (2011). For this study, only THEMIS day-time infrared images with average surface temperatures of greater than 250 K, and water-ice and dust opacities of less than 0.15 were examined.

THEMIS data were corrected for atmospheric effects using the techniques described by Bandfield et al., (2004b). Briefly, this correction is performed in two steps: First, a spectrally uniform region with a range of surface temperatures (e.g., shaded and sunlit slopes) is isolated in the THEMIS image. This set of spectra is then used to isolate and remove the additive contributions of atmospheric emission and scattering. Second, surface emissivity derived from Thermal Emission Spectrometer (TES) data, coincident with a portion of the THEMIS image, is isolated; the surface emissivity from this area is then used to provide the multiplicative contributions for atmospheric attenuation in each THEMIS spectral band. The multiplicative terms are then applied pixel by pixel at the full spatial resolution of THEMIS to retrieve atmospherically corrected emissivity spectra across the full THEMIS image (Bandfield et al., 2004b). This method assumes that the atmosphere is constant across the THEMIS scene, which is generally the case in images with small variations in elevation and low water-ice opacity. For this study, elevation varies by up to 1.8 km over the surfaces analyzed. Assuming an atmospheric scale height of 12 km and well-mixed atmospheric dust, this results in a maximum 9 µm opacity difference of <0.01.

Table 2.1. THEMIS Spectral Bands

Band	Center Wavelength (µm)
1	6.78
2	6.78
3	7.93
4	8.56
5	9.35
6	10.21
7	11.04
8	11.79
9	12.57
10	14.88
6	10.21

2.2.1.2 Decorrelation Stretch (DCS) Images

Spectrally distinct units within THEMIS images were initially identified by the examination of running decorrelation stretch (DCS) images (Gillespie et al., 1986; Edwards et al., 2011) derived as standard products from THEMIS infrared data (Bandfield et al., 2004a). THEMIS DCS images are typically displayed using bands 8-7-5, 9-6-4, or 6-4-2 projected as red, green, and blue, respectively (See **Table 2.1** for wavelengths). For example, regions with shorter wavelength absorptions, consistent with elevated bulk-silica, appear yellow in THEMIS DCS image stretches using bands 8-7-5 and 9-6-4, and magenta in band 6-4-2 stretches (**Figure 2.2**). Similarly, regions with elevated olivine abundance have long wavelength emissivity absorptions and will appear purple, purple, cyan in DCS 8-7-5, 9-6-4, and 6-4-2 stretches, respectively. Temperature variations can affect color in the DCS images, sometimes leading to ambiguous interpretations, however, the images provide a rapid means for the identification of spectrally unique surface units that can be confirmed through a more detailed examination of the spectral data.

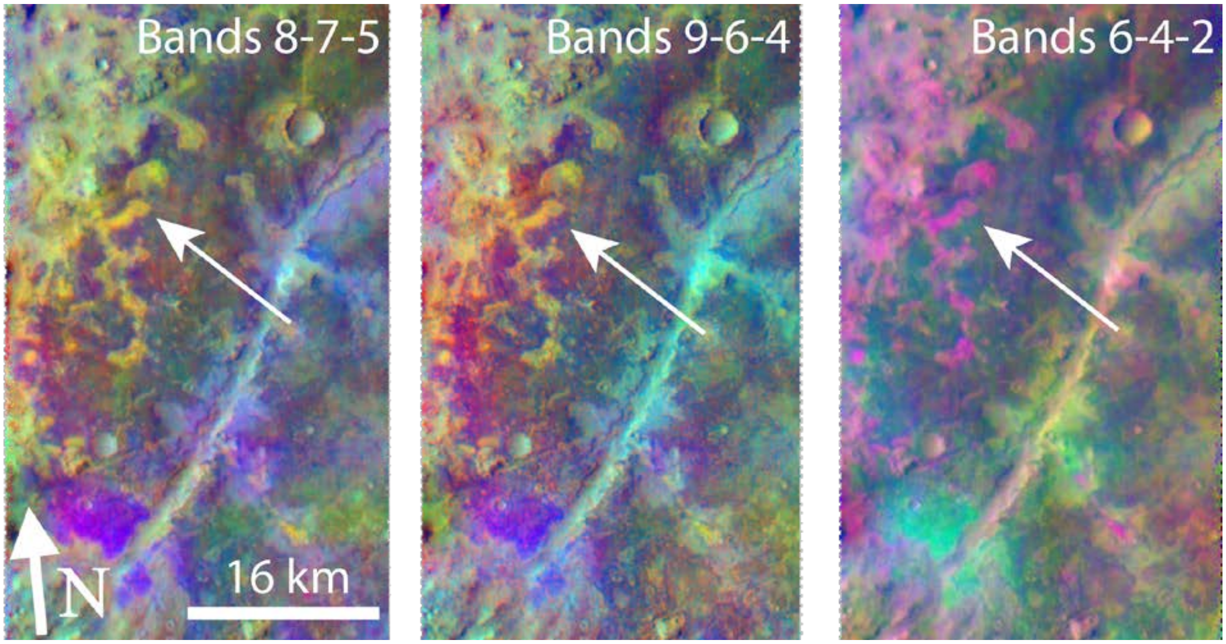

Figure 2.2. 3-panel decorrelation stretch (DCS) for THEMIS image I37499019. Arrow points to elevated bulk-silica surface, identifiable by its color combination across all three stretches.

2.2.1.3 "Weighted Absorption Center" (WAC) Index Maps

To produce a more directly interpretable image and to rapidly identify units with elevated bulk-silica compositions, we produced "weighted absorption center" (WAC) index maps (Vincent and Thomson, 1972; Smith et al., 2013). Given the limited number of spectral bands for THEMIS data, it is difficult to determine the specific mineralogical phases present. However, THEMIS is highly sensitive to the bulk-silica abundance of silicate surface materials as its wavelength range covers the diagnostic reststrahlen Si-O asymmetric stretch absorption band between 8 and 12 µm wavelengths. As bulk-silica abundance increases, the reststrahlen absorption band minimum shifts to shorter wavelengths (e.g., Vincent and Thomson, 1972; Walter and Salisbury, 1989). Determining the wavelength of the true band minimum for THEMIS data is difficult given the limited spectral resolution, but Smith et al., (2013) showed that the weighted center of the integrated reststrahlen band can be used instead of the true band minimum of the reststrahlen feature. Because this feature is well covered by the THEMIS wavelength range, this method can be used to determine relative silica abundance in surface spectra of regions of interest (Vincent and Thomson, 1972; Smith et al., 2013).

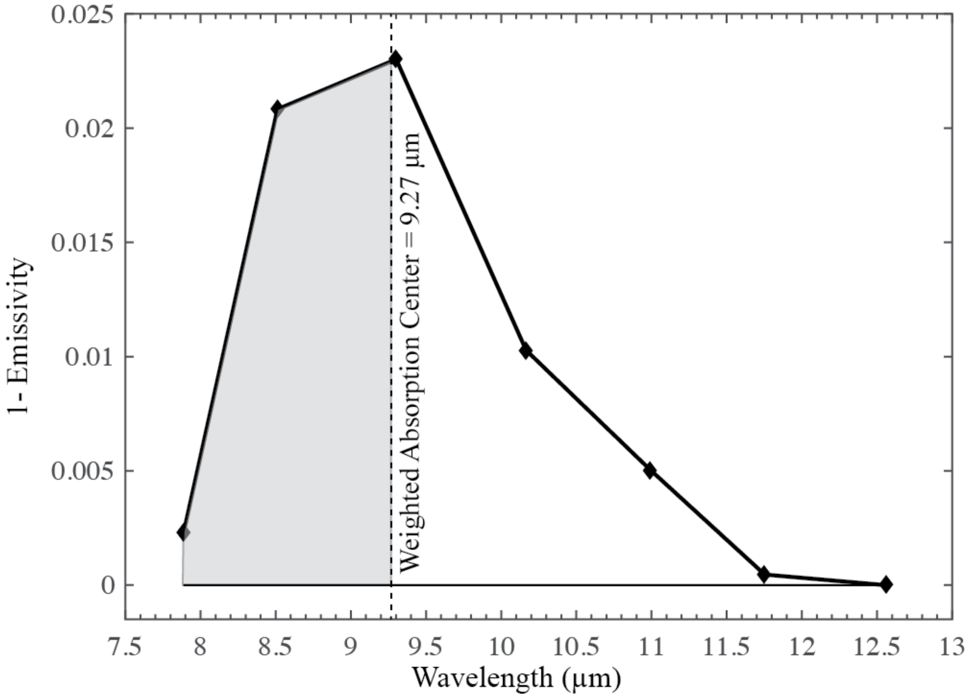

Figure 2.3. Depiction of the calculation for the “weighted absorption center” (WAC) value for a given THEMIS spectrum (bands 3-9).

We have created WAC index maps that provide a quantitative and visual representation of the varying bulk-silica across a single or multiple THEMIS images. The WAC index uses atmospherically corrected emissivity from THEMIS bands 3 through 9. To apply the index consistently between images, emissivity for each pixel is normalized to the maximum value of that spectrum. The new spectrum is then inverted to calculate the integrated area beneath the curve using linear interpolation between data points. The WAC wavelength value is determined by calculating the wavelength at which half of the integrated area is located on each side of the center wavelength (**Figure 2.3**). The presence of martian dust reduces spectral contrast and has scattering effects that interfere with this method. Thus, THEMIS pixels with a spectral contrast of less than 0.03 in emissivity (indicating the presence of significant dust) are masked to prevent misidentification.

The WAC index is also sensitive to the presence of other non-silicate phases, such as sulfates, as they also typically have band minima at shorter wavelengths within the THEMIS spectral range. To ensure that the WAC index in Nili Fossae was detecting variability in silica content only, CRISM NIR data were examined in regions of interest to ensure that sulfate-bearing compositions were not present.

THEMIS DCS images and WAC index maps were then used in coordination as each technique has its own uncertainties and limitations. For example, colors in DCS images can be influenced by temperature as well as composition. In contrast, the WAC values across a given THEMIS image can be affected by dust cover. Therefore, no single technique alone was used to confirm the presence of significant compositional variability. This combined approach adds confidence in our analysis and determination of surface unit properties.

2.2.2 Compact Reconnaissance Imaging Spectrometer for Mars (CRISM)

CRISM is a hyperspectral visible- and near-infrared imager onboard the Mars Reconnaissance Orbiter (MRO) with 544 spectral bands between ~ 0.4 and 4.0 µm (Murchie et al., 2007). CRISM has multiple observation modes with several spectral and spatial samplings. This study predominately used multi-spectral survey products (MSP) images with 70 spectral bands and a spatial sampling of 200 meters/pixel. MSP images were relied upon due to the limited higher resolution image coverage spatially coincident with areas of interest. However, despite the lower spatial and spectral sampling, CRISM MSP data have much more extensive coverage than the higher resolution data products, which enabled a more complete regional understanding of the observed mineral phases.

CRISM images are corrected for atmospheric gas absorptions using the scaled volcano-scan method described in McGuire et al., (2009). Absorptions due to atmospheric gasses are isolated by subtracting a spectrum from the summit of Olympus Mons from one at its base. The resulting gas bands are scaled and subtracted from each pixel in the CRISM image of interest.

CRISM spectral index maps were created in a manner like that described by Pelkey et al., (2007) and Viviano-Beck et al., (2014). These maps take advantage of specific spectral features indicative of particular phase groups across a CRISM image, which allows for the rapid analysis of the data. Areas of interest within an image can then be further investigated by evaluating I/F values (defined as the spectral radiance observed by CRISM divided by the solar spectral irradiance at the Mars distance divided by π) and spectral ratios to confirm the presence, or absence, of the spectral feature(s) of interest. Spectral ratios were created by taking a pixel average of I/F values for an area of interest and dividing it by the I/F pixel average for a region considered spectrally neutral (or spectrally known) within the same averaged image column. Band ratios allow for 1) the further reduction of systematic instrument errors and residual atmospheric gas absorptions, and 2) the isolation of relatively narrow absorptions such as the 2.3 µm smectite Fe/Mg-OH vibrational absorption (e.g., Clark et al., 1990).

2.2.3 Context Camera (CTX)

WAC and CRISM index maps were co-registered with high resolution imaging data to determine regional morphological context and stratigraphy. We used ~6 meter/pixel imaging data from the MRO Context Camera (CTX; Malin et al., 2007). CTX images have extensive spatial coverage in Nili Fossae and our regions of interest with 30 km swath width images. These images were used to determine relative albedo (tone) and textures of the units of interest.

2.3 RESULTS

2.3.1 TIR Spectral Results

2.3.1.1 THEMIS Data Selection

We completed a survey of 231 THEMIS daytime infrared images (**Supplementary Table 5.8**) that fell within a bounding box with an area of ~1.0 x 10^6 km^2 (**Figure 2.1**). Of these initial images, 55 were discarded based on visual inspection and identification of interfering factors such as high water-ice or dust opacities and excessive image striping or banding – the remaining 176 images provided complete (and often repeated) spatial coverage of the survey area with high quality data products (i.e., surface temperatures >250K, and dust and water-ice opacities <0.15). These data were then examined using the DCS bands 8-7-5 stretched images. With this stretch, surfaces with elevated olivine content appear purple and surfaces with elevated bulk-silica content appear yellow to amber. The 176 images were surveyed for discrete yellow/amber pixels in regional proximity to purple pixels (see Figure 2.4 for an example location). This regional proximity criterion was used to keep the spatial scope of the study within the Nili Fossae region where the known stratigraphy of basement rock, topped by olivine-rich basalt, topped by capping unit, exists. From these, 96 images were discarded due to low compositional variability with no evidence for yellow/amber surfaces in regional proximity to purple surfaces. This left 79 high-quality THEMIS images over our area of interest, given the wealth of data with repeat coverage, a set of 17 images were ultimately chosen to be atmospherically corrected for analysis of surface emissivity, WAC indices, and WAC values. These remaining images provided full spatial coverage of our region of interest. Units of interest were defined using the DCS imagery data and then described using other analysis techniques. See **Supplementary Table 5.9** for final image selections.

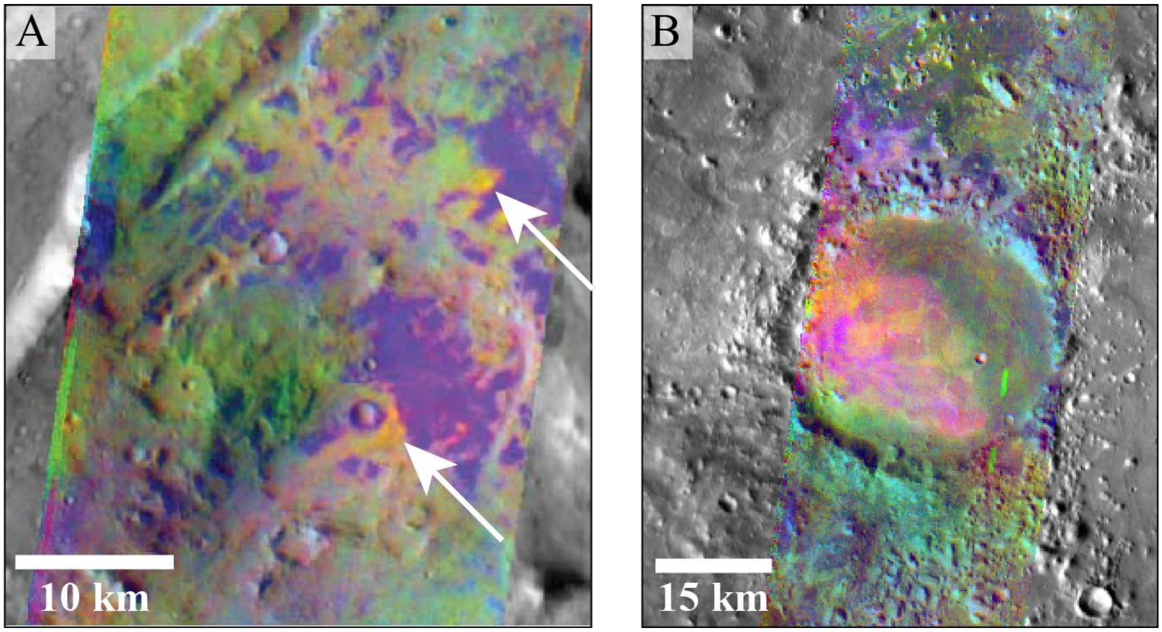

Figure 2.4. Panels A and B show the four TIR defined spectral units. Panel A (THEMIS image I18532009) shows the Purple Unit and the Yellow/Amber Unit (arrows). Panel B (THEMIS image I01570009 over THEMIS day IR) shows the Fuchsia/Orange Unit. Panel A is centered around 76.53ºE and 23.38ºN. Panel B is centered around 80.23ºE and 21.74ºN.

2.3.1.2 DCS Images

THEMIS DCS images show a wide-range of spectral variability across the Nili Fossae region. The region comprises distinct surface units that we have defined using their colors in DCS images using THEMIS bands 8-7-5. Typical, unremarkable terrain across the region ranges in color but is generally a washed-out or pale-brown or -green. This unit will be referred to as “typical terrain”. There are then three vibrantly colored surface units defined as the Purple Unit, the Yellow/Amber Unit, and the Fuchsia/Orange Unit (**Figure 2.4**ab).

The Purple Unit is extensive with exposures that span the area between ~76.0º and 80.5º E and 26.0º and 16.4º N. Exposures of the Purple Unit range in area and can be identified as discrete exposures <3.0 km^2 or as large, diffuse exposures up to 3,000 km^2. Found in regional association with the Purple Unit is the Yellow/Amber Unit with discrete exposures that typically cover an area <35.0 km^2. Finally, this region also contains wide-spread Fuchsia/Orange Unit surfaces (**Figure 2.4**b); we have defined this as a single unit despite there being two vibrant colors associated with it given that for this unit, a) the two colors are always found spatially intermixed and b) these surfaces are typically made up of dunes that are present across the area.

The TIR defined units are clearly identifiable in DCS images using other band combinations as well. For band combinations 9-6-4 and 6-4-2, the Purple Unit appears magenta and cyan, the Yellow/Amber Unit appears yellow and magenta, and the Fuchsia/Orange Unit appears purple/magenta and cyan/magenta, respectively (e.g., **Figure 2.2** and **Figure 2.4**a).

2.3.1.3 Weighted Absorption Center (WAC) Images

THEMIS images within the Nili Fossae region have WAC values that range from ~9.12 to 11.07 µm. Typical terrain has WAC values of ~10.07 to 10.14 µm (**Table 2.2**). Of the surface units defined here, the DCS Purple Unit has the highest WAC values. These values are typically between 10.40 and 10.60 µm (**Table 2.2**), but can be as high as 11.07 µm. The Yellow/Amber Unit shows a range of values, most commonly near 10.0 µm; however, there is a cluster of Yellow/Amber exposures in a 1,600 km^2 region centered around 23.51º N, 76.77º E with low WAC values that are ~9.6 µm (**Figure 2.1** inset and **Figure 2.5**). These exposures are commonly more amber than yellow in the DCS images, and are often spatially located adjacent to the Purple Unit (*e.g.,* **Figure 2.4**). Lastly, WAC values for the Fuchsia/Orange Unit ranged between 10.0 – 10.2 µm. Although image pixels with WAC values of <9.5 µm are present within all images, they are most often a single isolated pixel or a small cluster of pixels within the image scene and are not present as a coherent exposure.

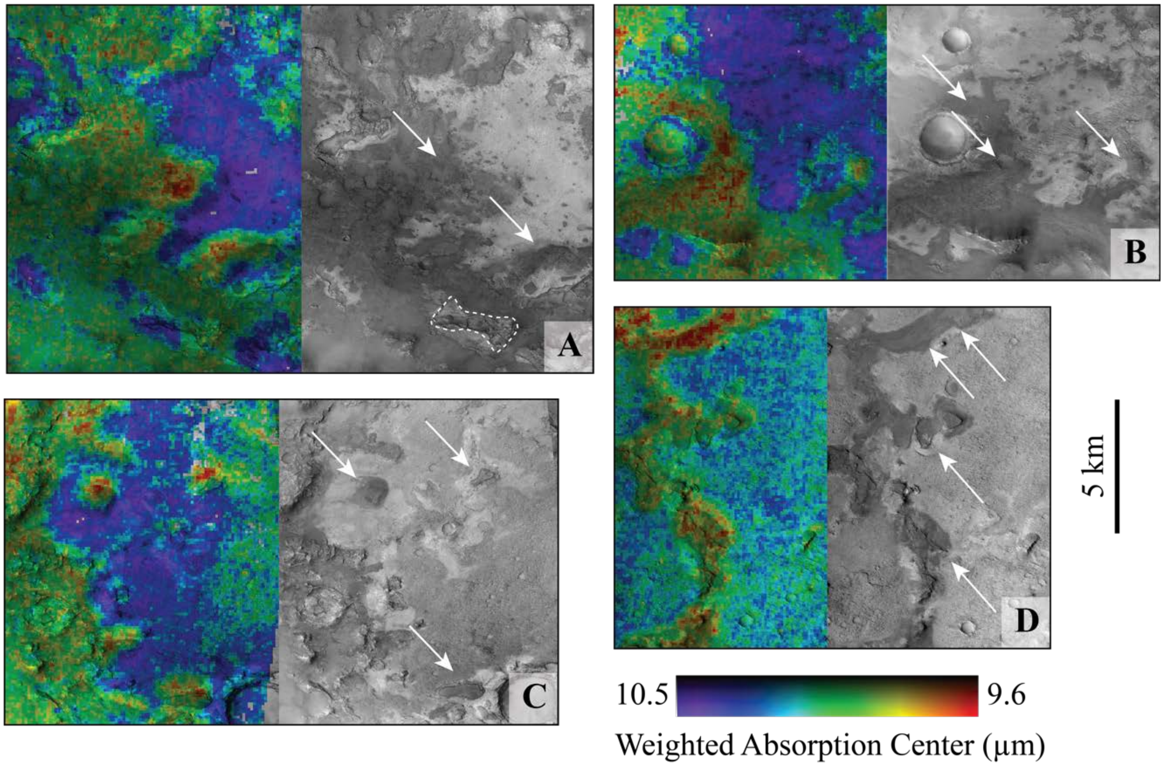

Figure 2.5. THEMIS WAC index maps and associated CTX images covering regions with exposures of the Purple and Yellow/Amber Units and phyllosilicate-bearing terrain. Low WAC values indicate surfaces with high bulk-silica compositions. White arrows point to Yellow/Amber Unit exposures, dashed white polygon indicate phyllosilicate-bearing surface. Purple Unit exposures are light-toned and have variable texture at the decameter-scale. Yellow/Amber Unit exposures are dark-toned and smooth and have a sharp contact with the bright Purple Unit. THEMIS and CTX images are (a-b) I18532009 and P13_006211_2038_XN_23N283W, (c) I36613020 and G18_025225_2058_XN_25N_283W, and (d) I02007009 and F06_037963_XI_23N_282W, respectively.

Table 2.2. TIR-defined Unit Descriptions

DCS Defined Spectral Unit	**WAC Values**	**CRISM observed phases and features**
Typical Terrain	~10.07-10.14 µm	Fe/Mg-smectites
Purple Unit	~10.40-10.6 µm (up to 11.07 µm)	Olivine
Yellow/Amber Unit	Commonly ~10.0 µm (clusters of ~9.6 µm)	1.9 µm (hydration) absorption
Fuchsia/Orange Unit	10.0-10.2 µm	-

2.3.1.4 Spectral Shapes

The THEMIS emissivity spectra in Nili Fossae show four distinct spectral shapes (**Figure 2.6**a) which correspond to the surface units defined by the DCS images and WAC index maps. The emissivity spectra for the typical terrain unit have a low spectral contrast with a slight, asymmetrical absorption weighted towards shorter wavelengths and emissivity minima occurring in band 5. Purple Unit emissivity spectra have a higher spectral contrast and a broad, asymmetrical absorption weighted towards longer wavelengths and emissivity minima occurring in band 7. This spectral shape is consistent with the high WAC value calculated for this unit.

Emissivity spectra for the Yellow/Amber Unit can be broken down into two subtly different, but distinct, spectral shapes. Emissivity spectra from surfaces that are yellow in DCS 8-7-5 images have a spectral shape like typical terrain, but with a higher spectral contrast (like the Purple Unit) consistent with its slightly lower than average WAC values around 10.0 µm (**Figure 2.6**a). In comparison, spectra from surfaces that appear amber in the DCS 8-7-5 stretch also have a higher spectral contrast but a narrow, asymmetric absorption weighted towards shorter wavelengths and a steep long-wavelength shoulder between bands 5 and 8 that shallows in slope between bands 8 and 9. Though the emissivity minimum is also in band 5 for the amber unit,

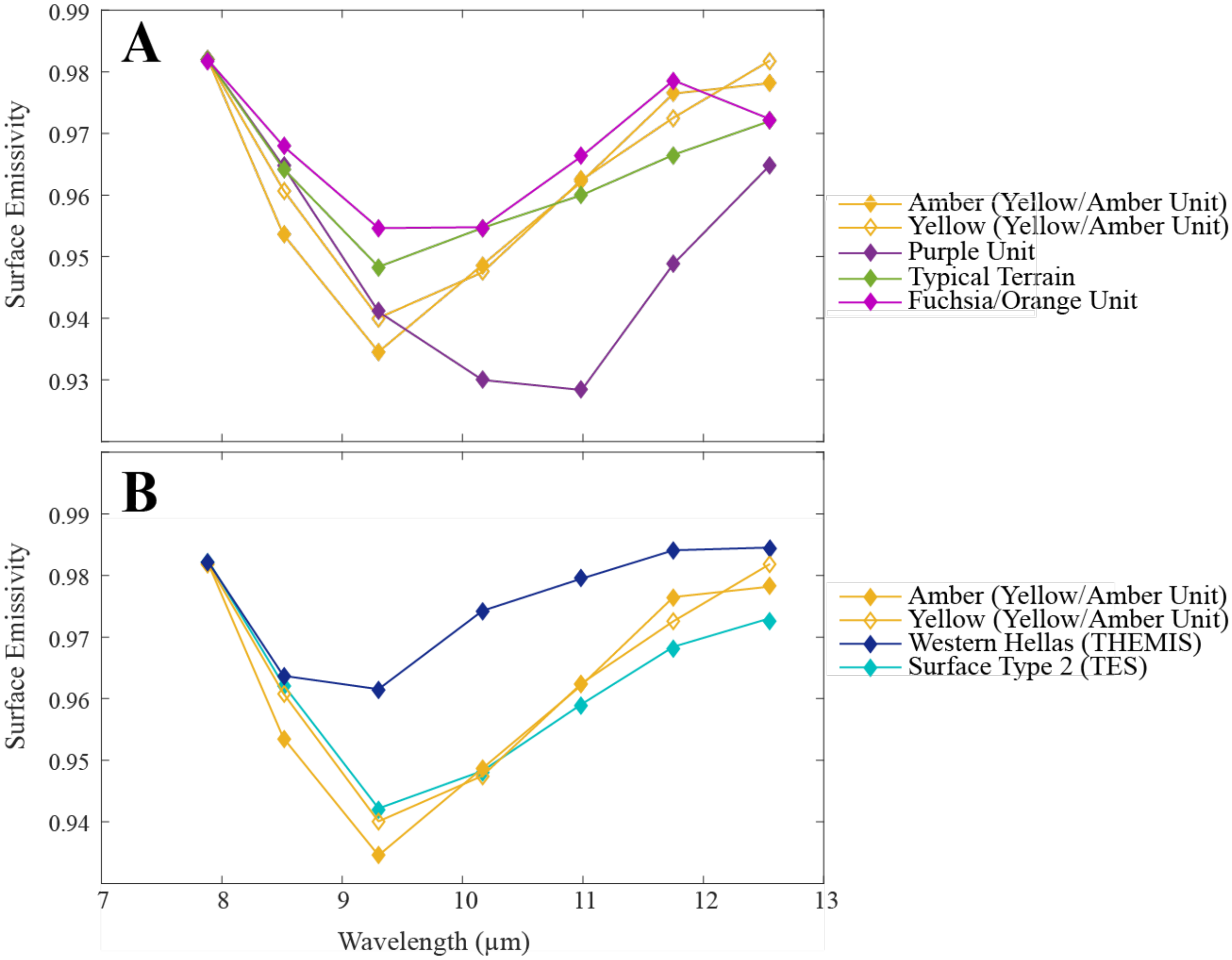

Figure 2.6. THEMIS emissivity data for bands 3 (7.93 μm) through 9 (12.57 μm). A) Spectral data for the four TIR defined spectral units found in the Nili Fossae region, including the subtly different Yellow and Amber spectra of the Yellow/Amber Unit. B) Comparison of the Yellow/Amber Unit spectra to other Mars spectral endmembers. Surface Type 2 spectrum acquired by TES and convolved to THEMIS spectral sampling. Line and sampling for THEMIS spectra can be found in **Supplementary Table 5.10**.

it has the lowest band 4 emissivity value of all the units described (**Figure 2.6**a). The spectral shape for this unit is consistent with its low WAC value around 9.6 μm. Emissivity spectra for the Fuchsia/Orange Unit have an overall lower spectral contrast than the Purple and Yellow/Amber Units, an emissivity minimum in band 5, and a kink between bands 8 and 9 (**Figure 2.6**a).

2.3.2 NIR Spectral Analysis

2.3.2.1 Index Maps

CRISM spectral index maps were surveyed in regions coincident with the analyzed TIR data. We searched for phases associated with aqueous weathering of basaltic rocks, including phyllosilicates, hydrated silica, sulfates, and carbonates and for evidence of bound and/or adsorbed H_2O molecules (see **Supplementary Table 5.11** for all indices surveyed). We also surveyed the OLINDEX (sensitive to the broad olivine absorption centered near 1.0 µm) in areas where olivine-rich basalts have been previously detected - this helped to ensure that the CRISM data were of sufficient quality. In other words, CRISM data with regions where no broad olivine absorption was observed yet was expected, given observations from other instruments, was thrown out as a poor-quality image.

Of the spectral indices surveyed, the OLINDEX, D2300 index (sensitive to a negative drop-off in slope at 2.3 µm, characteristic of hydroxylated Fe/Mg-silicates), and the BD1900 (sensitive to bound and/or adsorbed H_2O molecules) have positive detections in the region of interest.

Within the THEMIS typical terrain unit, are surfaces that are distinctly identified by their elevated D2300 index values. The D2300 phyllosilicate-index shows widespread, high values in MSP data as far east as 80.12 °E within the search area with the phyllosilicate-bearing exposures that are typically tens of square kilometers in area. Also, spatially associated with the high D2300 index values are elevated BD1900 hydration-index values, consistent with the presence of hydrated phyllosilicate phases. The TIR defined Purple Unit is spatially co-located with surfaces identified as olivine-bearing by the OLINDEX in CRISM data.

The Yellow/Amber Unit showed variable identifications from CRISM spectral index maps. Surfaces that were more amber than yellow, were weakly highlighted in the BD1900 index (**Figure 2.7**ab), interestingly, the same cluster of amber exposures that had the lowest WAC values (~9.6

µm), were the exposures that showed the weakly positive detection in the BD1900 index. This weakly positive BD1900 index value indicates a limited abundance of hydrated phases, however, no phyllosilicate phases were highlighted with high D2300 index values (**Figure 2.7**a and **Figure 2.8**), co-spatial with these exposures. Exposures that were more yellow than amber were not highlighted by any of the index maps surveyed. The Fuchsia/Orange Unit was highlighted by moderate OLINDEX values and weakly identified using the BD1900 index.

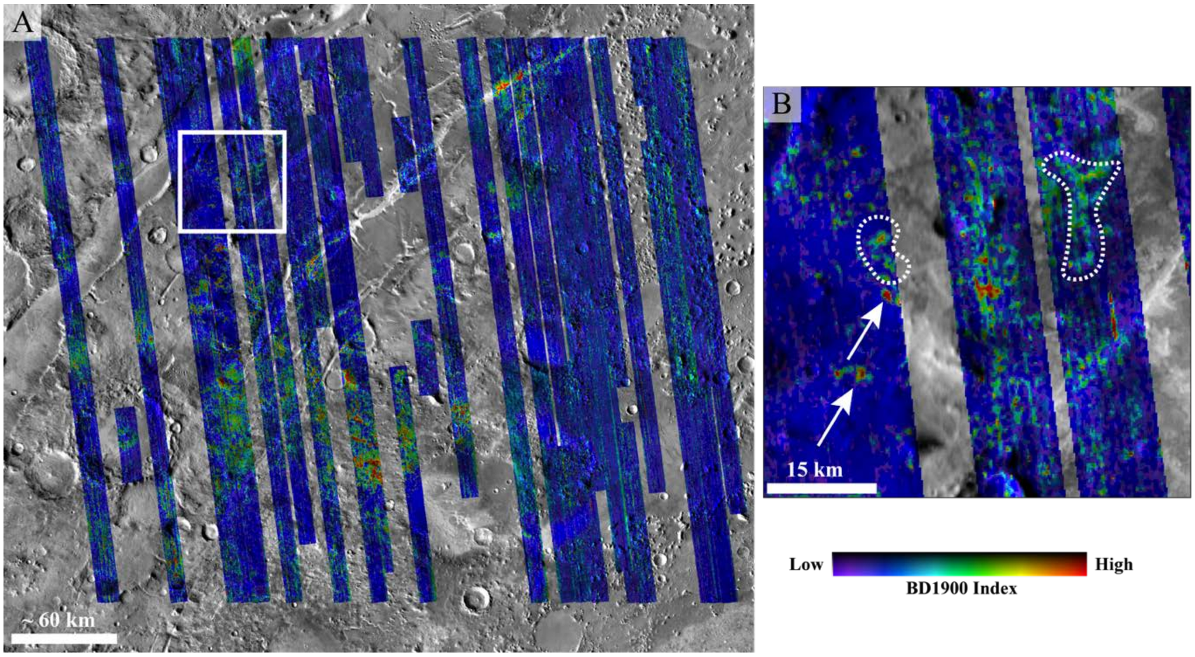

Figure 2.7. A) CRISM MSP BD1900 hydration index map using individually stretched images across Nili Fossae. White box indicates location of Panel B. Hydrated phases span across most of the region and predominately indicate the presence of phyllosilicate-phases. B) Dashed polygons indicate the location of Yellow/Amber Unit exposures identified by TIR data that show hydrated signatures in NIR MSP data. White arrows indicate exposures of phyllosilicate-bearing surfaces identified by D2300 index and inspection of spectral ratios. Panel A is centered near 78.54ºE and 21.76ºN. See **Supplementary Table 5.12** for MSP image IDs.

Other index maps surveyed showed no positive detections in the region (**Supplementary Table 5.11**). It should be noted however, that a non-detection in these MSP index maps, does not necessarily indicate the absence of the mineral phase. For example, Mg-carbonate bearing surfaces have been previously identified in areas co-spatial with MSP00013755_01 (e.g., Ehlmann et al., 2008) but the Mg-carbonate index (e.g., BD2500) showed no positive detection. As such, care has been taken to inspect individual I/F spectra and spectral ratios for surfaces co-located with the TIR surfaces units, in particular the Yellow/Amber Unit.

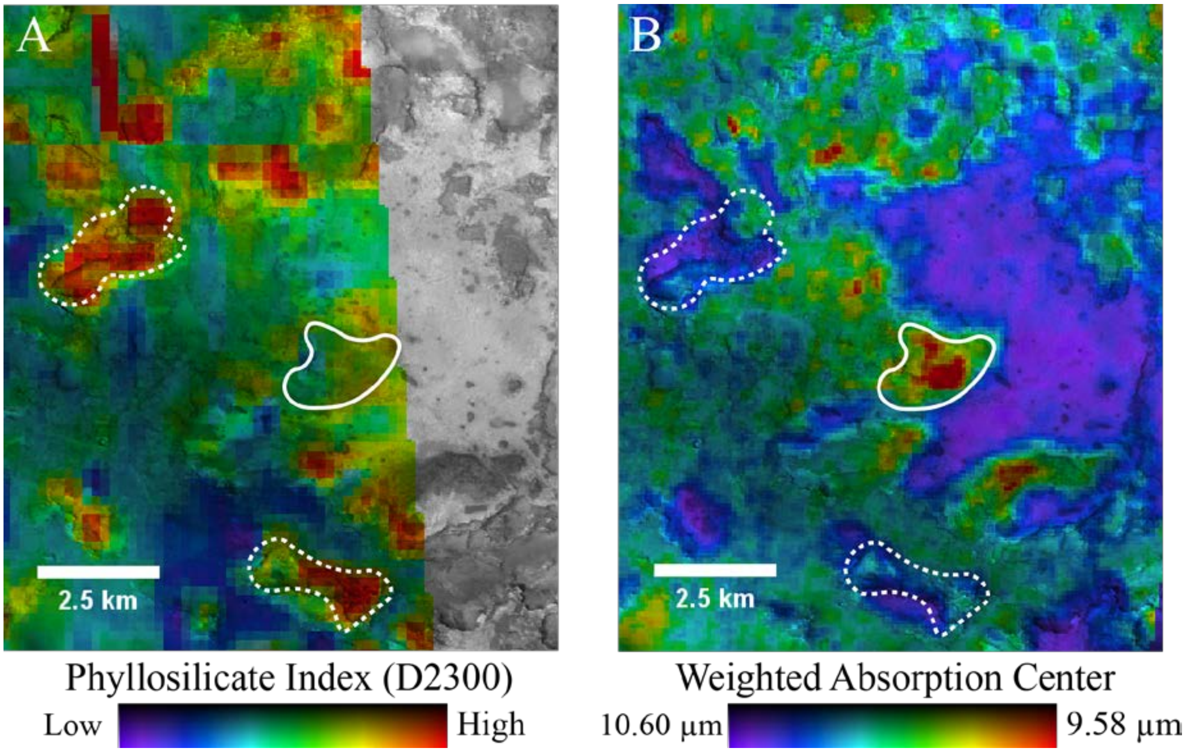

Figure 2.8. Comparison of phyllosilicate-bearing surfaces (high 2300 index values, MSP0000366C_01) and elevated bulk-silica surfaces (low WAC index values; THEMIS I18532009). Panels A and B cover the same spatial region. Solid white polygons indicate location of Yellow/Amber Unit exposure and dashed white polygons indicate phyllosilicate-bearing surfaces. index maps shaded by CTX image data. Image is centered near 77.83ºE and 23.37ºN.

2.3.2.2 Spectral Ratios

Four CRISM MSP images were selected for analysis of I/F ratioed spectra: MSP0000366C_01, MSP00007526_07, MSP00013755_01, MSP000037E8_03. These images spatially overlap all four TIR surface units observed. The NIR I/F data within these images clearly show the presence of spectral variability due to mineralogical phases.

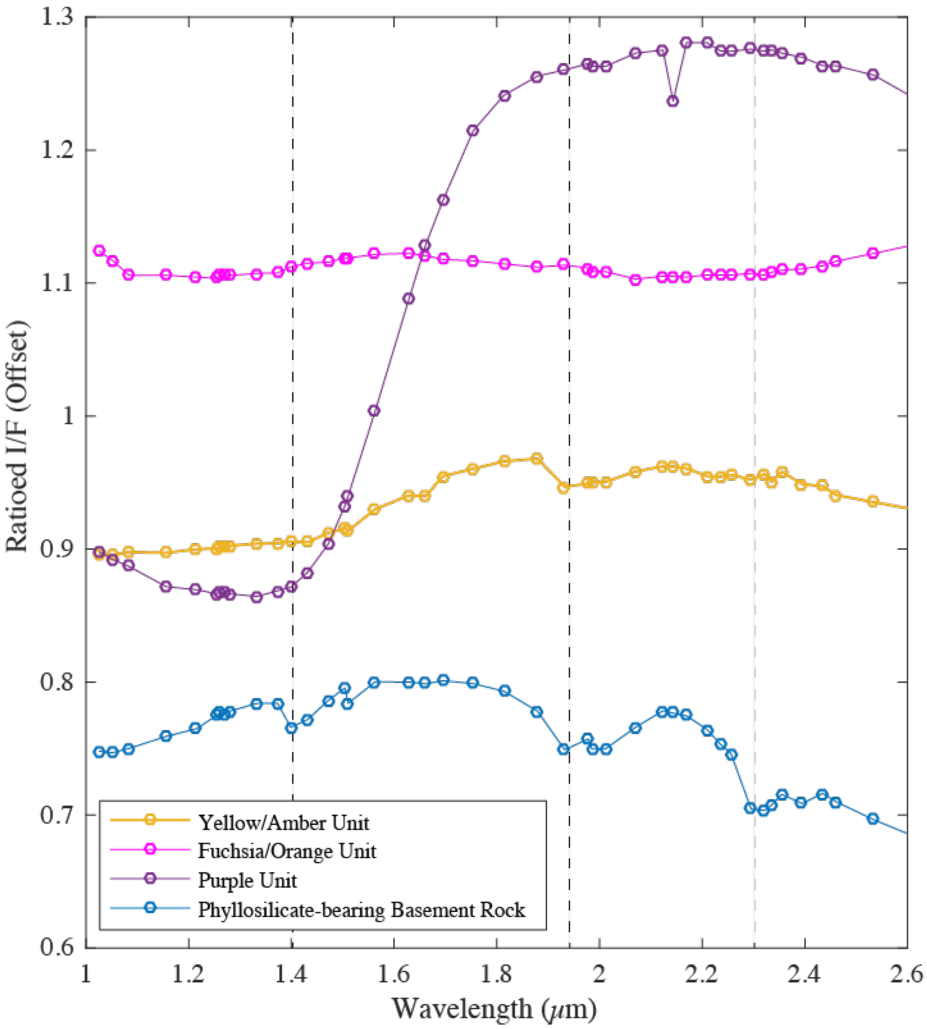

Figure 2.9. CRISM MSP spectra for the TIR defined spectral types (except typical terrain) and a phyllosilicate-bearing exposure ~5km from a Yellow/Amber Unit exposure. Yellow/Amber Unit spectrum is an average of 8 Yellow/Amber Unit spectra taken from MSP0000366C_01 (see **Supplementary Table 5.13** and **Supplementary Table 5.14** for all pixel locations for spectra presented here). Yellow/Amber Unit spectra show a weak broad short-wavelength absorption consistent with olivine, and a weak 1.9 μm absorption consistent with bound H_2O.

MSP images were spatially co-registered with both THEMIS DCS images and colorized WAC index maps in JMARS (Christensen et al., 2009). We used the co-registration to find the

MSP image pixels that best correspond to the surface exposures of the Yellow/Amber Unit in TIR data. I/F spectra for these surfaces were then ratioed against pixels within the same image column of typical terrain (as determined by the co-registered TIR data) that did not contain phyllosilicate phases (as determined by both the D2300 index and visual inspection of the I/F spectra). We collected NIR spectral ratios for surfaces co-registered with the TIR DCS Purple, Yellow/Amber, and Fuchsia/Orange units as well as those detected as phyllosilicate-bearing with the D2300 index.

I/F spectra for typical terrain are spectrally featureless except for a broad 2.0 µm absorption likely due to residual CO_2 from the atmosphere. Spectra from this terrain were used to ratio against I/F spectra from other surfaces of interest.

The TIR defined Purple Unit (co-located with surfaces having positive detections in the NIR OLINDEX index) has spectral ratios with a broad absorption centered at ~1.3 µm and a long-wavelength shoulder at ~1.8 µm. This absorption is due to the ferrous component of olivine and is typical of an olivine-bearing basalt (**Figure 2.9**).

Surfaces that show positive detections in the D2300 index have spectral ratios with distinct absorptions at 1.4, 1.9, and 2.3 µm (**Figure 2.9**), typical of a Fe/Mg-smectite (e.g., nontronite). These exposures are also located within the TIR defined typical terrain (**Figure 2.8**), however are not identifiable in the TIR data themselves.

The Yellow/Amber Unit shows spectral ratios that have a broad (albeit weak relative to the Purple Unit) short-wavelength absorption consistent with the presence of olivine given its spectral shape, this may be due to sub-pixel contributions from neighboring olivine-bearing surfaces. Two exposures in MSP0000366C_01 (of the ~10 exposures analyzed) show a weak, but clear, 1.9 µm H_2O hydration absorption. Three exposures in MSP000366C_01 present a weak 2.2 µm absorption in spectral ratios, however these are often on the same level as the spectral noise and are not enough to confidently attribute to an Al^{3+}-OH component. Otherwise, no long-wavelength absorptions consistent with a metal-OH phase were detected within the spectral ratios of the Yellow/Amber unit.

Spectral ratios of the Fuchsia/Orange Unit have low spectral contrast, like typical terrain, but show two broad and weak absorptions, one at ~1.0 µm and another at ~2.0 µm. These two broad absorptions are approximately consistent with an increase in pyroxene relative to typical terrain, however, given the weak spectral contrast it is difficult to assess the absorption shapes and centers for confident identification.

2.3.3 Unit Textures

2.3.3.1 CTX

The Yellow/Amber Unit appears dark-toned compared to the surrounding terrain; the unit is smooth at the meter scale and typically shows few to no pits or craters and relatively homogenous tone and texture. Where Yellow/Amber Unit exposures are adjacent to the Purple Unit, there is a clear contact between the two, however the transition between the Yellow/Amber Unit and typical terrain is normally more diffuse **Figure 2.5**, **Figure 2.10**, and **Figure 2.11**).

The Fuchsia/Orange Unit shows clear morphological evidence for dune structures. The dunes are dark toned and barchanoid in shape (**Figure 2.11**b). The dark-toned dunes are associated with the fuchsia pixels in the DCS bands 8-7-5 stretch. The pixels which are more orange are associated with lighter toned surfaces. The light-toned surfaces appear highly textured with small ridges and remnant craters. Dark-toned, dunes are likely enriched in olivine particulates and may presently, or in the past, have scoured the underlying light-toned surface.

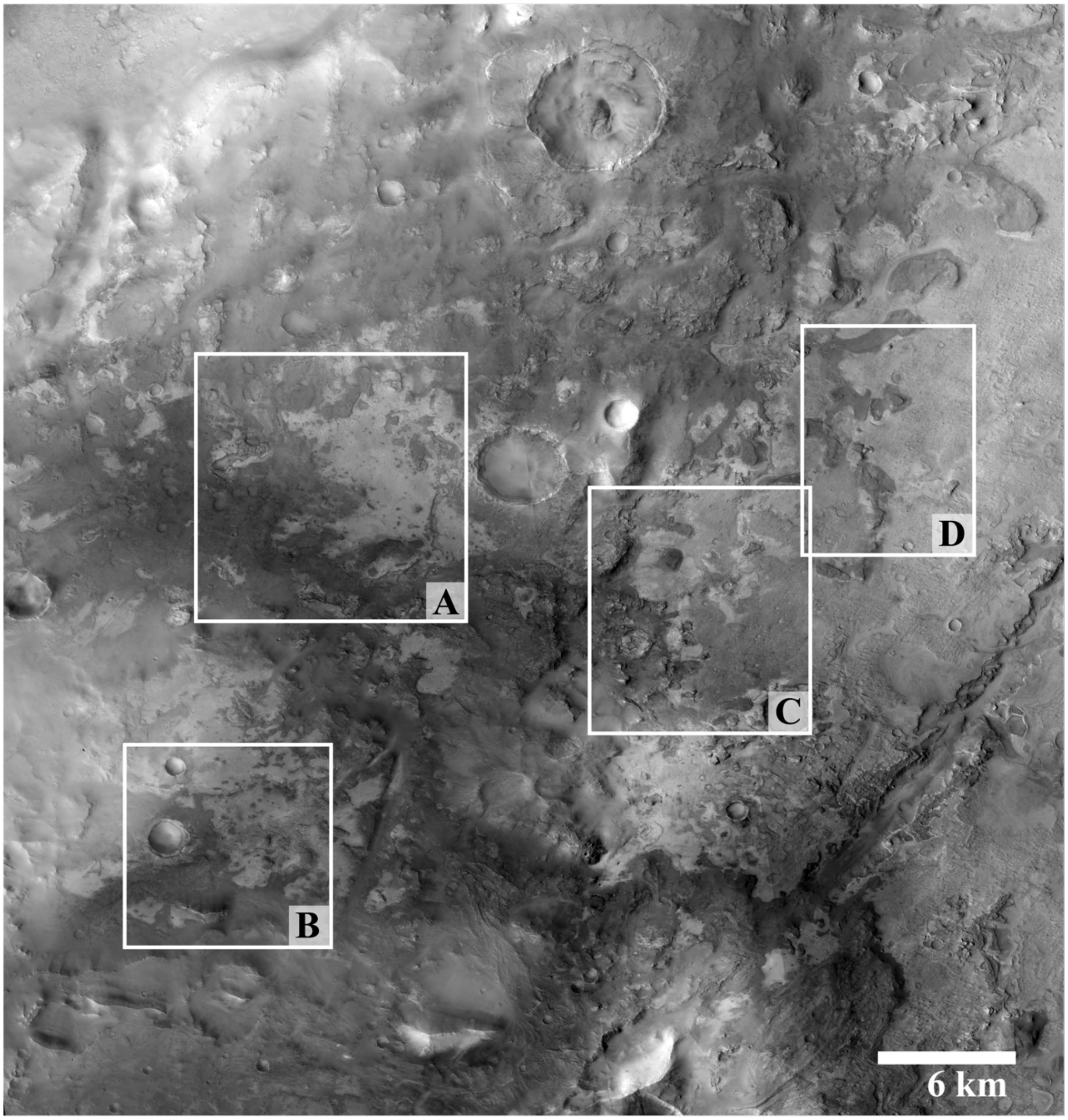

Figure 2.10. CTX mosaic centered around 76.93ºE and 23.45ºN. Inset solid boxes indicate locations for Panels A-D in **Figure 2.5**.

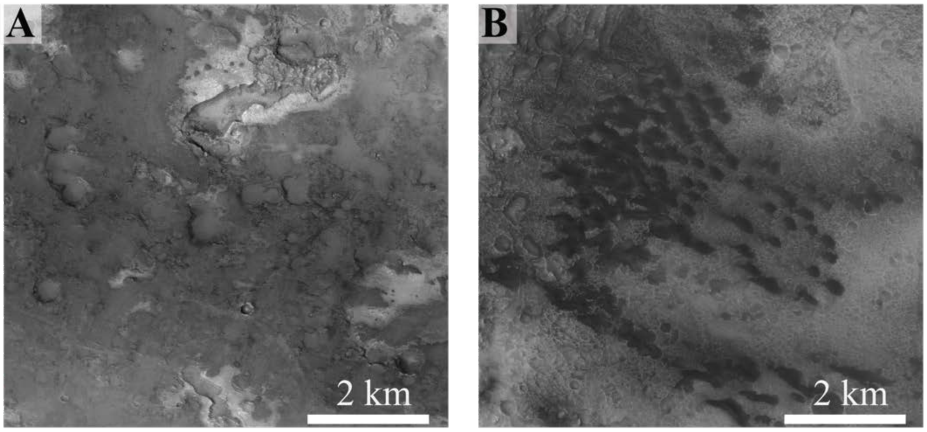

Figure 2.11. (A) Representative exposure of typical terrain, dark-toned, cratered, and rough in texture; CTX P13_006211_2038_XN_23N_283W. (B) Representative exposure of the Fuchsia/Orange Unit, dark barchanoid-shaped dunes with lighter-toned scalloped terrain underneath; CTX P17_007_648_2015_XN_21N_279W.

2.4 DISCUSSION

2.4.1 Compositions

The integration of TIR analysis techniques (DCS imagery, WAC index maps, and visual inspection of emissivity spectra) combined with the NIR analysis techniques (spectral absorption index maps and spectral ratios), allows for a robust determination of surface compositions in Nili Fossae. Here, we discuss the compositions of the TIR-defined units, based on both the THEMIS and CRISM data analyses.

2.4.1.1 Typical Terrain

The TIR-defined typical terrain illustrates the different sensitivities of the TIR and NIR spectral datasets. Thermal-infrared emissivity and weighted absorption center wavelength values indicate that the bulk-rock composition for this unit is an olivine-poor basalt, (i.e., a composition dominated by plagioclase feldspar and high-Ca pyroxene). We find that typical terrain in the Nili Fossae region has a WAC value of ~ 10.1 µm, similar to laboratory spectra of basalt samples and typical martian basaltic compositions found globally (10.2-10.3 µm; Smith et al., 2013). The slightly lower WAC value of typical terrain likely indicates that the region has a relatively higher bulk-silica component compared TES Surface Type 1 (ST1; Bandfield, 2000) or other basalt compositions. This is consistent with past studies using TES spectra and mineral phase maps (e.g., Bandfield, 2000; Bandfield, 2002; Edwards and Ehlmann, 2015) that show consistent high-Si phases (~20%) present in northeastern Nili Fossae, attributed to either a slightly higher silica content in the primary igneous composition or a small amount of aqueous alteration throughout region (e.g., Bandfield, 2002; Mangold et al., 2007; Rogers and Christensen, 2007).

However, where the THEMIS data show a relatively uniform surface, consistent with basaltic compositions, the CRISM data show spectral variability, including exposures of Fe/Mg-smectite bearing material (e.g., nontronite-bearing). The phyllosilicate-bearing surfaces are not identifiable in the THEMIS TIR spectral data products and would otherwise be missed without the inspection of CRISM NIR data. The phyllosilicate abundance must be relatively low given that the THEMIS data do not show a significant change in the spectral response over those surfaces, despite their sensitivity to changes in bulk composition.

2.4.1.2 Purple Unit

Purple Unit is the most compositionally unambiguous unit and has been studied extensively (e.g., Hoefen et al., 2003; Hamilton and Christensen, 2005; Mustard et al., 2007; Tornabene et al., 2008). Spectral signatures, WAC values, and NIR I/F spectral ratios are all consistent with the presence of an olivine-enriched basalt. Our data agree with past interpretations, and have relatively high WAC values ranging between 10.40 and 11.07 µm, consistent with a lower bulk-silica content. This unit has been described as a basalt with ~20 to 30 vol% olivine with a Fo_{68-75} composition (Hoefen et al., 2003; Hamilton and Christensen, 2005; Koeppen and Hamilton, 2008; Edwards and Ehlmann, 2015).

2.4.1.3 Yellow/Amber Unit

The shape of the Yellow/Amber Unit TIR emissivity spectra, coupled with its low WAC value, is consistent with a composition having an elevated bulk-silica component relative to the surrounding terrain. In NIR data, some exposures of the Yellow/Amber Unit show a weak 1.9 µm H_2O absorption feature; where this hydration feature is present, TIR spectral data indicate the lowest WAC values – indicating the highest relative concentration of bulk-silica. Given that the NIR spectra lack the clear presence of other diagnostic absorption features (e.g., a 1.4 µm H_2O/OH and 2.21-2.26 µm (Si-OH) absorptions consistent with hydrated silica or 1.4 µm and 2.2/2.3 µm metal-OH absorptions consistent with phyllosilicate phases), we are unable to use CRISM data to determine the hydrated mineral phase(s) present. Though it should be noted that the lack of these absorptions does not preclude their physical presence: a) the absorptions could be present but too weak to detect with the instrument, and/or b) an increase in sediment grain size could lower the overall reflectance and thereby decrease the depth of diagnostic absorptions (e.g., Rice et al., 2013). It should also be noted that we cannot rule out the presence of diagenetic quartz in these surfaces, which is not expected to have a 1.9 µm hydration absorption feature. As such, it is possible that we are detecting two different high silica units.

Given the limited spatial extent of the Yellow/Amber exposures, we are unable to resolve the high silica and hydrated surfaces using the high spectral resolution TES data. However, the THEMIS emissivity spectra and the WAC values can be compared to other elevated bulk-silica regions on Mars determined from previous studies. Smith et al., (2013) examined the range of *hydrated* silica exposures identified across Mars to date. Their work compared WAC values for the exposures, or what they call “center-of-gravity” measurements, to NIR CRISM spectral data and allowed for a quantitative means of linking bulk-silica composition and degree of alteration. The exposures of the Yellow/Amber Unit with the lowest WAC values indicate the highest bulk-silica content in the region. These exposures have WAC values of ~9.6 µm, similar to the values calculated by Smith et al., (2013) for exposures in Northern Syrtis Major (~ 9.56 µm). Those exposures are located to the southeast of Antoniadi Crater, the only known region with quartz exposures on Mars (Bandfield et al., 2004a). Work by Ehlmann et al., (2009 and Smith and Bandfield, (2002) showed that the quartz outcrops detected with TIR spectral data (TES and THEMIS) are co-located with hydrated silica identified using CRISM NIR data.

We can also compare the low WAC values for Yellow/Amber Unit exposures to other martian spectral endmembers, including the TES derived Surface Type 2, (ST2; spectrally consistent with a basaltic andesite (Bandfield, 2000) or basalt with silica coatings (Kraft et al., 2003) (**Figure 2.6**b). TES ST2 has a WAC value of ~ 9.96 µm, when convolved with the THEMIS spectral bandpasses, and a bulk-silica abundance of ~ 58 wt% (Hamilton et al., 2003), most of the Yellow/Amber Unit has WAC values of ~10 µm, similar to ST2. The lowest WAC values for the Yellow/Amber Unit (~ 9.6 µm) were in a more amber than yellow cluster of exposures (**Figure 2.5**). These values are less than TES ST2, implying that those exposures have a higher bulk-silica abundance than TES ST2. Similarly, the lowest WAC value documented by Smith et al., (2013) was 9.27 µm from hydrated silica exposures in Western Hellas Basin that are composed of ~ 78 wt% poorly crystalline hydrated silica phases (Bandfield, 2008; Bandfield et al., 2013b). Given that the more amber exposures of the Yellow/Amber Unit have WAC values that lie between those for ST2 and the Western Hellas exposures, it can be inferred that the bulk-silica abundances for the low WAC value Yellow/Amber Unit exposures are likely between these two units.

2.4.1.4 Fuchsia/Orange Unit

The barchanoid shaped dunes spatially associated with the Fuchsia/Orange Unit are consistent with a basaltic composition with some enrichment of olivine as indicated by elevated OLINDEX values in CRISM data. Given the dunes regional proximity to the olivine-rich basalts, some component of eroded olivine-rich sediment may have been incorporated into the active dunes and is consistent with past studies (e.g., Edwards and Ehlmann, 2015).

2.4.2 Stratigraphic Relationships

To this point, all surfaces units described have been segregated using the TIR DCS 8-7-5 stretch, and have been compositionally defined using the TIR and NIR spectral datasets. We have also described surface textures and morphology using CTX images. However, these descriptions do not place the defined units in a spatial or stratigraphic context. As discussed in Section 2.1.1., previous studies in Nili Fossae have described three main stratigraphic units in the region: a phyllosilicate-bearing basement rock, an olivine-enriched basalt unit, and a capping rock unit (Ehlmann et al., 2009; Mustard et al., 2009). Our work presented here allows for a more complete compositional perspective of the main rock units in the area. The classic stratigraphic units in Nili Fossae can now be viewed from a new stratigraphic perspective; one which breaks them down into their bulk rock composition and their associated secondary alteration composition (**Figure 2.12**).

Based on our analysis presented here, the lowest stratigraphic unit in the section referred to in past studies as the phyllosilicate-bearing basement-rock unit (e.g., Mustard et al., 2009), has a bulk-rock composition of an olivine-poor basalt and is part of the TIR-defined typical terrain. This stratigraphic unit has limited exposures of hydrated, Fe/Mg-smectite phases like those found elsewhere in the region and across Mars (e.g., Poulet et al., 2005; Mustard et al., 2009).

The next stratigraphic unit up-section has a bulk-rock composition of an olivine-rich basalt. Isolated exposures of this unit in the region are variably altered to Mg-carbonate, talc/saponite, and serpentine phases (Ehlmann et al., 2008, 2009, 2010; Brown et al., 2010; Viviano et al., 2013; Edwards and Ehlmann, 2015) based on analysis of NIR and TIR spectral datasets. This stratigraphic unit is strictly co-located with the TIR defined Purple Unit.

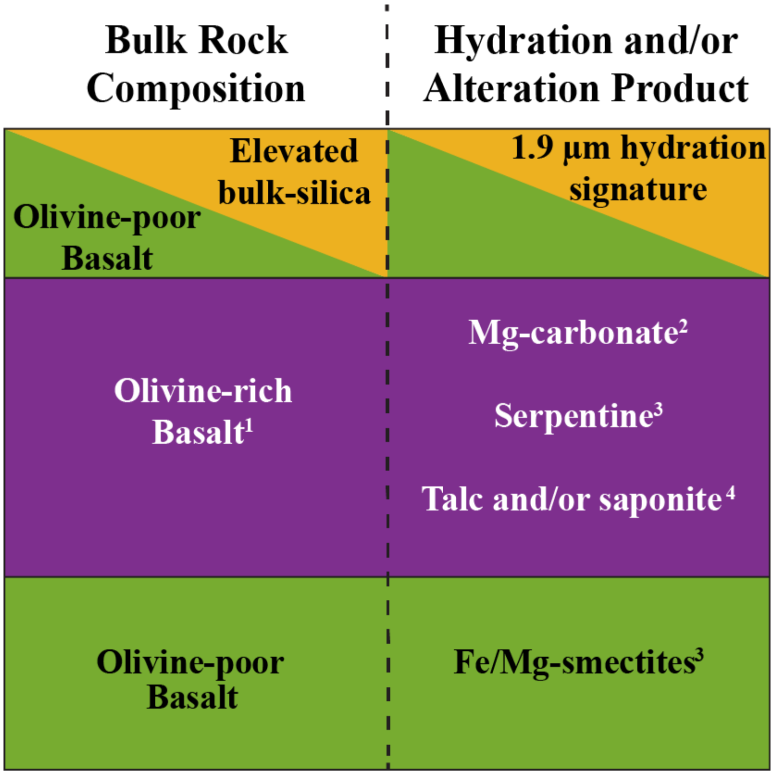

[1]Hamilton and Christensen, 2005; [2]Ehlmann et al., 2008; [3]Ehlmann et al., 2009; [4]Brown et al., 2010

Figure 2.12. Eastern Nili Fossae stratigraphy in terms of bulk-rock composition and alteration products. Spatial scaling is not represented in this visualization. The top capping unit can be broken down into an unaltered, olivine-poor basalt, and separately, an altered capping unit with an elevated bulk-silica composition that is sometimes hydrated.

The uppermost unit has been referred to as the Nili Fossae capping unit (e.g., Mustard et al., 2009). However, from our analyses here, this stratigraphic formation is the most complicated with large variations in bulk composition. The formation can be broken down into two different compositions; (1) an olivine-poor basalt with no apparent alteration phases – this is spatially co-located with the TIR defined typical terrain and makes up much of the capping unit; (2) isolated surfaces with an elevated bulk-silica composition and a sporadic 1.9 µm hydration feature – this is spatially co-located with the TIR defined Yellow/Amber Unit. In this way, the uppermost unit in Nili Fossae, the capping unit, comprises both TIR defined typical terrain and the Yellow/Amber Unit (**Figure 2.12**). From here on, the capping unit will be referred to as either the "unaltered capping unit" or the "altered capping unit" in reference to these two compositions.

Lastly, the Fuchsia/Orange Unit corresponds to dunes that are typically located in constrained topography such as crater floors, valley bottoms, or behind raised topography (**Figure 2.11**b). These are presumably mobile sediments that can cover any of the three stratigraphic units.

2.4.3 Localized Alteration of the Capping Unit

The capping unit has previously been interpreted as unaltered. However, this work has shown regions within this unit with increased bulk-silica content relative to the surrounding terrain. On Earth, bulk-silica abundance can be elevated in a rock composition in many ways, including via both igneous and aqueous processes. For example, the primary igneous composition of the rock may have an elevated silica abundance through partial melting or other igneous processes (e.g., obsidian or granite). Conversely, aqueous alteration and siliceous deposition (in the form of silica coatings, silica residues, or precipitates from solution) can also increase the bulk-silica composition of the surface (Tosca and Knoll, 2009). Given the paucity of high-Si primary igneous compositions on Mars, in addition to the morphological characteristics of the altered capping unit (e.g., the diffuse transition from altered to unaltered capping unit), it is unlikely that the first scenario applies to these elevated bulk silica exposures (e.g., Carter and Poulet, 2013; Wray et al., 2013; Rogers and Nekvasil, 2015). Consequently, bulk-silica content may be used as a proxy for aqueous alteration, with the underlying assumption that much of Mars primary igneous compositions are mafic (e.g., McSween et al., 2009; Smith et al., 2013). This indicates that the altered capping unit represents some form of localized aqueous alteration of the uppermost unit in

Nili Fossae. The timing of the alteration relative to the formation of the rest of the capping unit is difficult to determine, however, it is clear that it relates to the stratigraphically youngest unit.

Ehlmann et al., (2009) broke down the aqueous history of the Nili Fossae region into three distinct episodes that may have overlapped temporally in some cases. (1) The aqueous alteration that formed the basement Fe/Mg-smectites, which was likely a widespread process given the extent of the pedogenic phyllosilicate phases. (2) The aqueous alteration episode that altered the basement unit Fe/Mg-smectites to overlaying kaolinite phases through leaching processes and variably altered the olivine-rich basalts to Fe/Mg-carbonates and serpentine/talc/saponite phases. (3) The fluvial activity that transported and deposited these altered minerals to channel bottoms (Ehlmann et al., 2009). Our work adds a fourth episode of aqueous activity that occurred after Episode 1 but otherwise is not constrained temporally and may have occurred contemporaneously with Episodes 2 and 3.

There are several potential sources (or combinations of sources) for the elevated bulk-silica content of the altered capping unit. One possibility is that silica-saturated water may have been transported and subsequently precipitated in the fine-grained cap rock (Edwards and Ehlmann, 2015). For example, dissolved silica from the exothermic carbonation (e.g., Keleman and Matter, 2008) of the underlying olivine-rich basalt may have been transported upwards and deposited in cap rock. Carbonation of the olivine-rich basalt in Nili Fossae has been suggested by several studies as the source of the Mg-carbonate observed in the region (e.g., Viviano et al., 2013; Edwards and Ehlmann, 2015), and would produce SiO_2 (e.g., Keleman and Matter, 2008). This type of alteration and deposition would imply moderate to high water to rock ratios in moderate to low temperature conditions (e.g., Keleman and Matter, 2008). If this process is the source for the alteration of the cap rock, it constrains the timing of the formation of the silica to during or after the formation of the olivine-rich basalt and prior to, or contemporaneously with, the formation of channel networks, which cut through both the cap rock and Mg-carbonate-bearing rock (Edwards and Ehlmann, 2015). It should be noted that the Mg-carbonate-bearing surfaces appear ~45 km away from the altered capping unit, though the capping unit was likely significantly more extensive in the past than observed today. Additionally, high silica deposits have been identified elsewhere without associated carbonates and it is likely that silica-rich materials can form via a variety of processes on Mars.

An alternate possibility is that the increased silica signature of the altered cap rock is due to silica-coatings and/or cementation. Silica-coatings typically form under relatively slow and generally local weathering processes involving limited surficial water activity and are most likely to be present on sand or rock surfaces (e.g., Kraft et al., 2003) but do not make up a large proportion of the bulk volumetric composition. Given that the thermophysical properties of the cap rock are consistent with an eroded volcanic ash (Edwards and Ehlmann, 2015) and this study's evidence for increased bulk-silica content, silica-coatings are not the favored source for the increased silica signature. Rather, the fine-grained nature of the cap rock makes it particularly receptive to in-situ alteration, even under limited aqueous activity, leading to deposition and cementation from mobilized SiO_2. As such, a silica-cement that is pervasive throughout the rock, rather than a surface coating of silica, would be a more likely source for the increased silica signature of the altered cap rock.

Each of the three stratigraphic units show evidence for aqueous alteration of primary mafic materials. Although the primary unaltered material in the units is similar (with variations in olivine content), the alteration products show considerable variety. This implies that different aqueous conditions were likely responsible for the formation of the alteration phases present in each stratigraphic unit. This is especially the case with the basement and capping units, which have nearly identical unaltered bulk compositions, but different alteration products. A variety of alteration scenarios are possible that would elevate the bulk-silica composition of the cap rock to such an extent, ranging from the carbonation of underlying olivine-rich basalt, to surficial slow-weathering of the cap rock to produce silica-cements.

2.5 SUMMARY AND CONCLUSIONS

By combining both near-infrared and thermal-infrared spectral datasets, we have presented a new perspective in the understanding of known geologic units in Nili Fossae. We have shown the applicability of the "weighted absorption center" index maps as a reconnaissance tool and an aid by producing a broadly useful parameter: bulk-silica content. This has allowed us to identify a new compositional unit in Nili Fossae that likely represents the localized aqueous alteration of the Nili Fossae capping unit.

This work adds to the diversity of the recognized compositions in the Nili Fossae region. We have shown evidence for aqueous activity and alteration throughout the entire stratigraphic package in Nili Fossae. The compositions present within these units indicate a wide range of aqueous episodes, with some suggesting substantial amounts of water. We present evidence for aqueous activity that likely occurred after the formation of the basement phyllosilicates but otherwise is not constrained temporally. It may have occurred contemporaneously with the formation, and alteration, of the olivine-rich basalts and the formation of the capping rock. Furthermore, one potential source of the elevated bulk-silica surfaces in the cap rock may be linked to the hypothesized carbonation of underlying olivine-rich basalt, a process that produces SiO_2.

Lastly, we present a new example of multiple alteration products that are produced by different aqueous conditions, rather than differences in the primary composition. In this case, the basement-rock unit and the capping rock unit have nearly identical starting bulk compositions yet contain different alteration products. The alteration products indicate differences in conditions, such as water to rock ratios, the duration of alteration, as well as the thermal conditions present during formation. The Nili Fossae region presents a rare combination of multiple primary and variably altered compositions preserved within a clear stratigraphic sequence.

Chapter 3. **THE LOST CITY HYDROTHERMAL FIELD: A SPECTRCOPIC AND ASTROBIOLOGIAL ANALOG FOR NILI FOSSAE, MARS**

This manuscript has been accepted with minor revisions to the journal Astrobiology as of Dec. 12, 2016, revisions are due on March 12, 2017

Co-authored by: Elena S. Amador, Joshua L. Bandfield, William J. Brazelton, Deborah S. Kelley

3.1 INTRODUCTION

The search for habitable environments in our solar system is commonly driven by evidence for environments with liquid water. However, water alone is not sufficient to sustain life. Temperature and pH gradients, nutrients, and a source of biologically-accessible energy are also critical. Environments with active serpentinization, which involves the interaction of water with ultramafic rock, can host ecosystems driven predominantly by chemical energy harnessed from these alteration processes (e.g., Kelley et al., 2001, 2005; Früh-Green et al., 2004; Russell et al., 2010). Serpentinization has been documented in several terrestrial settings (used in this paper to describe a setting on the Earth as opposed to another planetary body), including the deep-sea hydrothermal vent system of the Lost City Hydrothermal Field (Kelley et al., 2001, 2005; Früh-Green et al., 2004), and the high-temperature Rainbow and Logatchev hydrothermal fields (Holm and Charlou, 2001; Petersen et al., 2009) on the Mid-Atlantic Ridge, as well as at numerous ophiolite complexes (e.g., Barnes et al., 1978; O'Hanly, 1996; Früh-Green et al., 2004). Spectroscopic studies of Mars have also shown evidence for serpentine-bearing surfaces, implying that serpentinization was an active process at some point in the planet's history (e.g., Ehlmann et al., 2009; 2010).

This study characterizes the spectral and mineralogical variability in mafic bedrock samples and their alteration products from beneath the Lost City Hydrothermal Field on the Mid-

Atlantic Ridge and compares these results with mineralogically similar exposures at Nili Fossae, Mars. Results are placed into a geochemical and astrobiological context for processes that operated on Mars with implications for existing and future measurements acquired by orbital and landed spacecraft on Mars. Results from this study may also inform future science and instrumentation for astrobiologically-relevant missions to Mars.

3.1.1 Serpentinization

Serpentinization is an exothermic, volume-increasing reaction caused by the hydration of olivine in ultramafic rocks (Reactions 1-3) (O'Hanley, 1996; Evans, 2010). The reaction enriches altered fluids in H_2 and CH_4 and other low molecular weight hydrocarbons that can be metabolically exploited by microorganisms (Abrajano et al., 1988; Kelley et al., 2001, 2005; Proskurowski et al., 2006, 2008; Brazelton et al., 2010; Lang et al., 2010). The reactions occur over a wide range of conditions that include penetration by meteoric and marine fluids, and at 200°C to >500°C temperatures.

The serpentinization process is ideally composed of three reactions:

Reaction 1:

$$Fayalite + water \rightarrow magnetite + aqueous\ silica + hydrogen \qquad (3.1)$$

$$3Fe_2SiO_4 + 2H_2O \rightarrow 2Fe_3O_4 + 3SiO_2 + 2H_2$$

Reaction 2:

$$Forsterite + silica + water \rightarrow serpentine \qquad (3.2)$$

$$3Mg_2SiO_4 + SiO_2 + 4H_2O \rightarrow 2Mg_3Si_2O_5(OH)_4$$

Reaction 3:

$$Forsterite + water \rightarrow serpentine + brucite \qquad (3.3)$$

$$2Mg_2SiO_4 + 3H_2O \rightarrow Mg_3Si_2O_5(OH)_4 + Mg(OH)_2$$

Subsequent production of methane is also common in serpentinizing systems, but requires introduction of a carbon source, for example:

Reaction 4:

$$4H_2 + CO_2 \rightarrow CH_4 + 2H_2O \quad (3.4)$$

Ultramafic rocks are dominated by olivine with lesser orthopyroxene minerals; these phases are thermodynamically stable at high temperatures and pressures, as in the mantle. However, they are unstable at lower temperatures in the near-surface and as a consequence readily react with aqueous fluids (e.g., Früh-Green et al., 2004; Schulte et al., 2006). Because the reactions are exothermic and result in an increase in the rock volume by up to 55% (O'Hanley, 1996), serpentinization may result in enhanced fracturing that promotes fluid flow and alteration (e.g., Kelley et al., 2001, 2005; Lowell and Rona, 2002; Vance et al., 2007; Denny et al., 2016).

Serpentinization produces hydrous Fe/Mg-serpentine phases that may be represented by the general formula (Mg, $Fe^{2+})_3(Si_2O_5)(OH)_4$. The three most common polymorphs are the Mg-rich phases antigorite, chrysotile, and lizardite. Other mineralogical products include magnetite and brucite. The reactions produce highly alkaline fluids that commonly lead to the precipitation of carbonate from both meteoric and marine solutions (O'Hanley, 1996; Früh-Green et al., 2003; Palandri and Reed, 2004; Ludwig et al., 2006).

Most relevant to astrobiology, the oxidation of Fe^{2+} in fayalite (Fe-olivine) produces highly reducing molecular hydrogen (H_2), which is then biologically accessible for microbial metabolic pathways, such as methanogenesis. Zones of active serpentinization, therefore, create habitable environments where other energy sources may not be available (e.g., solar or volcanic) and promote ecosystems driven by the direct products of these geochemical reactions. Serpentinization is likely to have occurred throughout much of Earth's history and may have potentially created environments suitable for the origin of life on early Earth (Russell et al., 2010, 2014; Stüeken et al., 2013; Sojo et al., 2016). Given the common association of liquid water in direct contact with olivine-rich bedrock on Earth, similar geochemical environments are likely present across the Solar System, including the icy satellites of Jupiter and Saturn. These moons likely have olivine-rich mantles in contact with liquid-water oceans and are compelling sites to visit for potential extant life in our Solar System (e.g., Malamud and Prialnik, 2013; Russell et al., 2014).

Products of serpentinization can be detected using orbital spacecraft with infrared spectrometers (e.g., Ehlmann et al., 2010). For example, planetary surfaces with serpentine-bearing phases have unique spectral absorptions in near-infrared (defined here as ~1.0–3.0 µm) reflectance spectra, allowing for the confident identification of serpentine (e.g., Ehlmann et al. 2010). Furthermore, given that serpentine is created via reactions that typically produce H_2 in the presence of liquid water, the identification of serpentine phases is a unique indicator for two of the three components commonly assumed necessary for a habitable environment: an energy source (H_2), a solvent (liquid water), and nutrients (e.g., Domagal-Goldman and Wright et al., 2016). Other phases associated with serpentinization, such as talc, also have spectral characteristics in the near-infrared and thermal-infrared (defined here as ~5.0–50.0 µm) portions of the spectrum. In concert, analyses that span the near- and thermal-infrared provide a more complete understanding of the full range of compositions present in a rock or planetary surface and clues about the paleoenvironment present during their formation and alteration history.

3.1.2 The Lost City Hydrothermal Field

3.1.2.1 Geology

The Lost City Hydrothermal Field is a submarine hydrothermal venting system located near the summit of the Atlantis Massif, ~15 km west of the slow-spreading Mid-Atlantic Ridge near 30° N (Kelley et al., 2001; 2005). The Atlantis Massif is part of a larger ultramafic oceanic core complex composed of uplifted, serpentinized mantle peridotites (e.g., Denny et al., 2016). The terrain is highly fractured with a complex tectonic history not uncommon for sites located near slow- and ultra-slow-spreading centers (Kelley et al., 2005; Karson et al., 2006; Denny et al., 2016). The Lost City was serendipitously discovered in 2000 (Kelley et al, 2001), and possesses actively venting limestone monoliths that rise 30-60 m above the surrounding seafloor. It has been active for at least 150,000 years (Ludwig et al., 2011) and hosts a robust microbial community driven by serpentine-dervived hydrothermal fluids (Schrenk et al., 2003; Brazelton et al, 2006; 2010) To date, it is a rare example of an oceanic environment where the alteration of the olivine-rich protolith provides biologically viable energy for microbial life (e.g., Schrenk et al., 2004; Brazelton et al., 2006; 2010).

Faulting of the Atlantis Massif exposes massive serpentinite with lesser gabbro in the bedrock that underlies the Lost City Hydrothermal Field and in adjacent cliffs. In this area, >70% of the exposed rocks are variably altered and deformed serpentinized harzburgites, an ultramafic igneous rock composed primarily of olivine and low-Ca pyroxene (Karson et al., 2006; Boschi et al., 2006; Denny et al., 2016). Serpentine mineral assemblages are predominantly lizardite, with or without chrysotile and trace amounts of antigorite (Boschi et al., 2006). Talc, chlorite, and tremolite are also found in association with the serpentine phase (Boschi et al., 2006). The summit of the massif is capped by pelagic carbonate (Kelley et al., 2001; Früh-Green et al., 2003; Denny et al., 2016). The field is enclosed by a halo of carbonate rubble from chimneys associated with the active and extinct vents (Kelley et al., 2005; Ludwig et al., 2006; Denny et al., 2016).

The Lost City Hydrothermal Field serpentinites, and associated alteration products, are produced by the hydration and oxidation of the underlying ultramafic rocks (predominantly harzburgites) (Kelley et al., 2001; 2005; Boschi et al., 2006; Delacour et al., 2008). Isotopic analyses indicate that the fluid/rock interactions typically occur at temperatures <150°C (Früh-Green et al., 2003; Proskurowski et al., 2006) and produce pH 9–11 vent fluids enriched in H_2, CH_4, and other low molecular weight hydrocarbons (e.g., ethane (C_2H_6), ethylene (C_2H_4), and propane (C_3H_8) (Kelley et al., 2001; 2005; Proskurowski et al., 2006, 2008; Lang et al., 2010). When the alkaline fluids mix with seawater, carbonate ions combine with Ca^{2+} ions, resulting in the precipitation of aragonite (Früh-Green et al., 2003; Ludwig et al., 2006). The Mg-rich mineral brucite also precipitates. During aging of the structures, brucite is lost and the metastable aragonite converts to calcite (Ludwig et al., 2006; 2011). Dating of the limestone deposits indicate that the field has been active for >120,000 years (Ludwig et al., 2011).

3.1.2.2 Biodiversity

A thriving microbial ecosystem was discovered at the Lost City Hydrothermal Field, presumably sustained by the geochemical products of serpentinization, hydrothermal flow, and mixing with seawater (Kelley et al., 2001, 2005; Schrenk et al., 2004; Brazelton et al., 2006, 2010). Extensive biofilms are developed on mineral surfaces within the carbonate structures (e.g., Kelley et al, 2001; Schrenk et al., 2004; Brazelton et al., 2011). Microbial communities representing all three domains of life (Brazelton et al., 2006; 2010; Lopez-Garcia et al., 2007) are found throughout the chimneys, from the mesophilic (~25° C), aerobic surfaces to the (hyper)thermophilic (50-90° C), anaerobic zones of the chimney interiors (Kelley et al., 2001; Schrenk et al., 2004). The resident microbial communities are stimulated by the abundant chemical energy available from serpentinization (Brazelton et al., 2011). This energy is approximately twice that available at basalt-hosted black smokers due to the higher concentration of H_2 (McCollom and Seewald, 2007) in serpentinization-driven systems.

3.1.3 Nili Fossae, Mars

The Nili Fossae are a set of concentric graben-forming fractures to the west of the Isidis Basin and to the north of the Syrtis Major volcanic complex (**Figure 3.1**). The fractures and faulting likely formed due to flexure and unloading associated with the Isidis basin-forming impact (Wichman and Schultz, 1989; Schultz and Frey, 1990). Extensive exposures of olivine-rich bedrock occur within and in proximity to Nili Fossae (e.g., Hoefen et al., 2003), which is observable from orbit (Ruff and Christensen, 2002).

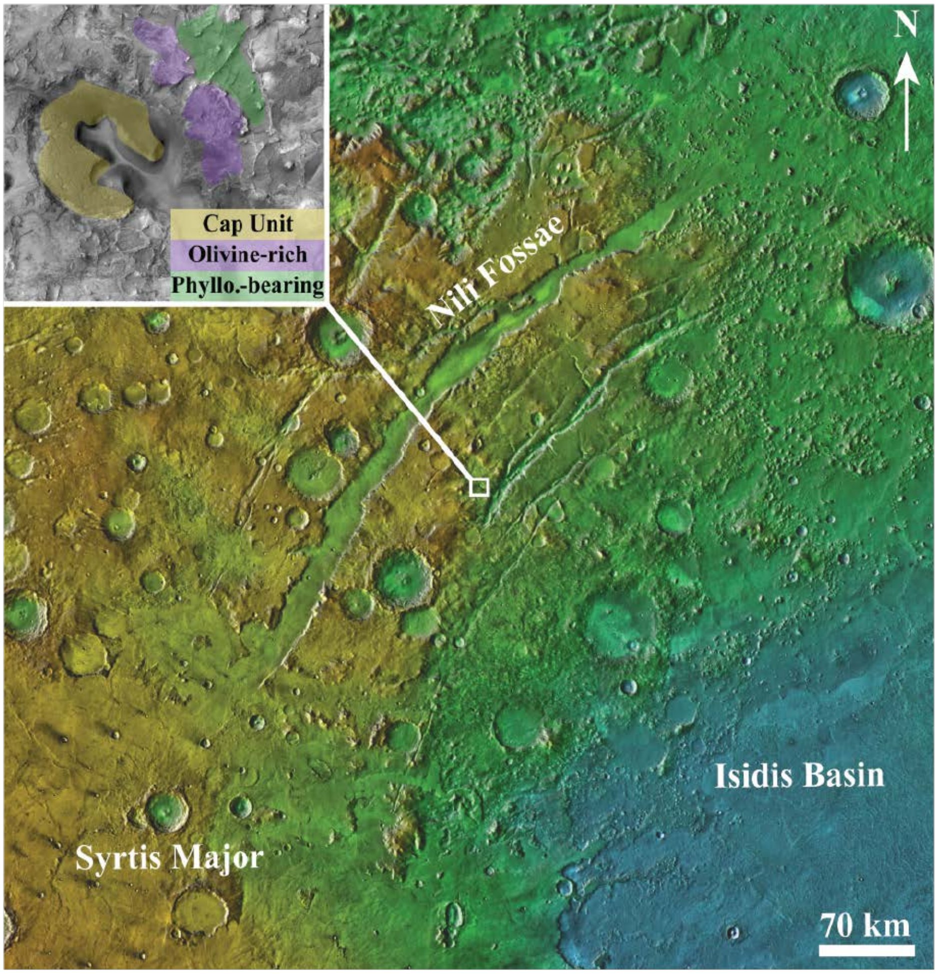

Figure 3.1. Nilo-Syrtis Major colorized elevation map with THEMIS Global Day IR mosaic used for shading centered around 76.6°E, 22.4°N. Inset image shows typical Nili Fossae stratigraphy in CTX image DO1_027691_2025_XN_22N_282W.

A diverse range of both primary and alteration minerals have been observed in the region (e.g., Poulet et al., 2005; Bibring et al., 2006; Mangold et al., 2007; Mustard et al., 2007, 2009; Ehlmann et al., 2008, 2009, 2010; Tornabene et al., 2008), including an assemblage of phases associated with low-grade metamorphism (e.g., Ehlmann et al., 2009, 2010; Brown et al., 2010; Viviano et al, 2013). These include serpentine, which has been identified by spectroscopic measurements in several locations across Mars (Ehlmann et al., 2010; Viviano-Beck and Murchie, 2014). However, the presence of serpentine phases in Nili Fossae are unique because they are found within a well-defined stratigraphic context. The eastern Nili Fossae bedrock is composed of three major bulk compositions. Moving from bottom to top of the section, the lowermost unit is composed of an olivine-poor basalt with an Fe/Mg-phyllosilicate component consistent with nontronite, followed by an olivine-rich basalt that has been variably altered to Mg-carbonate, serpentine, and talc and/or saponite, and topped by an olivine-poor basaltic capping unit with localized hydration and alteration to an elevated bulk-silica composition (Amador and Bandfield, 2016) (*Figure 1*).

3.2 APPROACH

Fifteen variably-altered and –deformed serpentinites, gabbros, fault-rocks, and carbonate samples from the Lost City Hydrothermal Field were selected for spectral analysis from a set collected by the human occupied vehicle Alvin during an oceanographic cruise in 2003 funded by the National Science Foundation (**Table 3.3** and **Figure 3.2**). We have separated the 15 samples into six rock-type groups: “Serpentinite”, “Carbonate”, “Gabbro”, “Talc-rich Fault Rock”, “Amphibole-rich Fault Rock” and “Pelagic Top-Layer”. Mineralogical and compositional analyses for the non-carbonate samples are described by Boschi et al. (2007), Delacour et al. (2008), and Karson et al. (2006) and for carbonate deposit samples by Ludwig et al., (2006, 2011)

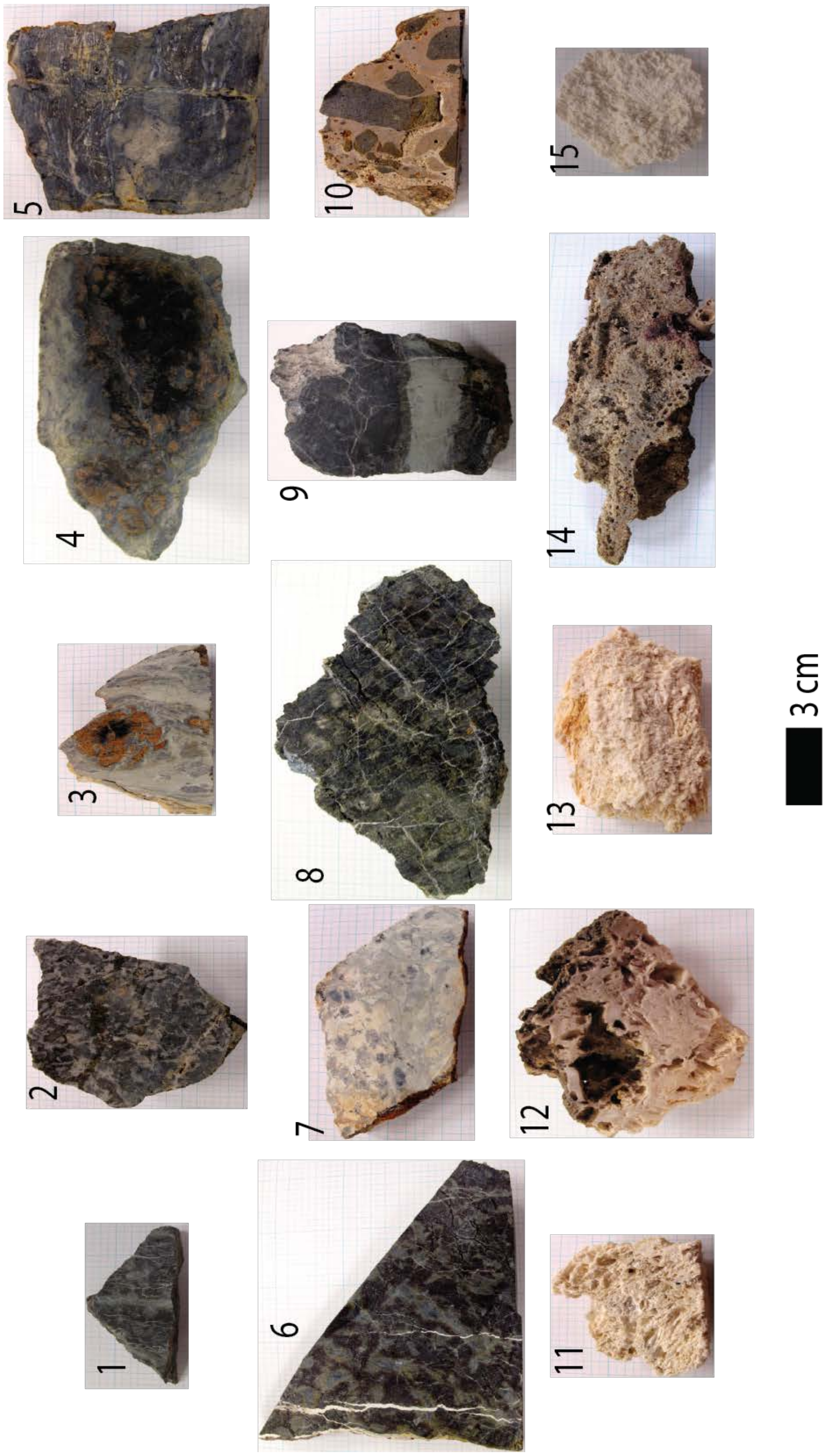

Figure 3.2. Photographs of the Lost City Hydrothermal Field samples used for this study.

(**Table 3.3**) using petrographic and bulk rock geochemical methods: no near-infrared or thermal-infrared spectral characterizations of these rocks had been performed previously. We have included a hand-held rock description for the 15 samples used for this study in **Table 3.3**.

Table 3.3. Lost City Hydrothermal Field Samples with descriptions. **Reference ID* is used across studies by others working with these samples. *Sample Number* is used for **this study only**.

Sample Number	Rock Type	Boschi et al., 2007 Table 1. Description	Delacour et al., 2008 Table 2. Description	Karson et al., 2005 Table 1. Description	Reference ID*	Rock Description (this Study)
1	Serpentinite	Serpentinite	None.	Serp+amph+chl. Veins of late calcium carbonate	3872-1136	Dark-toned, heterogeneous coloring, mesh-textured, small fractures
2	Gabbro	Gabbro	None.	Medium-grained gabbro	3876-1117	Dark-toned, heterogeneous, large fractures
3	Talc-rich fault rock	Talc-rich fault rock	None.	Serpentinite/talc-amph schist	3873-1124	Light-toned, heterogeneous coloring, marbled-texture, soapy feeling to touch
4	Serpentinite	None.	None.	Serpentinite	3873-1245	Massive, dark-toned, heterogeneous coloring, microfractures, mesh-textured
5	Gabbro	Mylonitic gabbro	None.	None.	3867-1254	Dark-toned, large fractures filled with light-toned material, marbled-texture
6	Serpentinite	Serpentinite	None.	None.	3877-1344	Heterogeneous, highly fractured with light toned material, mesh-textured, soapy feeling to touch
7	Amphibole-rich fault rock	Amphibole-rich fault rock	None.	None.	3877-1313	Light-toned, heterogeneous, marbled-texture
8	Serpentinite	None.	Serpentinite	None.	3877-1307	Heterogeneous, highly fractured with light-toned filling, mesh-textured
9	Serpentinite	Serpentinite (local metasomatism)	None.	None.	3877-1158	Heterogeneous, highly fractured, fractures, large alteration veins, soap feeling to touch
10	Pelagic top-layer	None.	None.	None.	3867-1116	Brecciated fragments in a fine-grained carbonate matrix
11	Carbonate	None.	None.	None.	3881-1132B	Porous, fine-grained, bright white, friable
12	Carbonate	None.	None.	None.	3867-1308	Brown colored, Porous, fine-grained, fossils, friable
13	Carbonate	None.	None.	None.	3869-1446	Porous, fine-grained, bright white, friable, some reddish-discoloration
14	Pelagic top-layer	None.	None.	None.	3862-1549 #6	Brown-colored, porous, fine-grained, friable, fossils
15	Carbonate	None.	None.	None.	3864-1537	Bright white, friable porous, fine-grained

Spectral characterization of rock samples has several benefits; first, it allows for a non-destructive method of determining the mineral constituents of the rocks, unlike (for example) preparing thin sections for electron microprobe analysis, which only provides elemental abundances. Second, little sample preparation is needed, saving time and resources. Third, spectral characterization provides a library from this specific hydrothermal environment using measurements directly comparable to those acquired of other planetary surfaces. Near- and thermal-infrared spectral measurements have been collected by numerous spacecraft throughout the Solar System, including Mars (e.g., CRISM/TES/THEMIS), Ceres/Vesta (Dawn VIR), and Pluto (New Horizons RALPH), Jupiter (Galileo NIMS), and they are planned for future robotic missions. These measurements are particularly useful because they can be made remotely from orbit and because they can provide a wealth of information at global, regional, and local scales. With these benefits in mind, we have measured the thermal-infrared emissivity and near-infrared reflectance properties for Lost City samples and compared them to measurements of low-grade alteration minerals on the surface of Mars in Nili Fossae (e.g., Ehlmann et al., 2009; Brown et al., 2010; Viviano et al., 2013). These measurements also serve as a spectral library for future orbital and landed spacecraft with these measurement capabilities.

3.2.1 Laboratory Spectral Measurements

3.2.1.1 Thermal Infrared

Thermal-infrared (TIR) emissivity measurements can provide an understanding of the bulk mineralogical composition for a given rock sample. This is possible because most rock-forming minerals have major absorptions in the 200–2000 cm^{-1} (5.0–50.0 µm) range (e.g., Thomson and Salisbury, 1993). Because of the implications for serpentinization and hydrothermal mineral identification, the spectral characteristics for silicate hydroxides and carbonates are of particular relevance to this work. Reststrahlen band absorptions occur between 833–1250 cm^{-1} (8.0–12.0 µm) due to vibrational motions associated with Si-O stretching modes – the exact minima for this feature depends on the mineral structure and composition (e.g., Hunt and Salisbury, 1971). Additional absorptions due to Si, O, and Al stretching and bending motions occur at longer wavelengths between 250 and 833 cm^{-1} (40.0 and 12.0 µm) (Hunt, 1980). Hydroxide-bearing minerals have characteristic spectral features due to fundamental bending modes of OH-metal ions (Hunt, 1980). Carbonate minerals have strong absorption features due to CO_3 vibrational modes in the 1250–1666 cm^{-1} (6.0–8.0 µm) range (Hunt and Salisbury, 1971).

TIR emissivity measurements allow for quantitative mineral abundances to be calculated from the whole rock spectrum. The high absorption coefficient of typical rock-forming minerals in the TIR spectral range results in a spectrum that can be approximated by a linear combination of each individual mineral spectrum of the measured surface, weighted by the areal abundance of the mineral (e.g., Thomson and Salisbury, 1993; Ramsey and Christensen, 1998). The TIR spectral measurements therefore serve to a) determine the bulk mineralogy of the Lost City samples, and b) provide an understanding of the variety of TIR spectral characteristics specific to this type of hydrothermal system. The latter can be used for future data analysis and instrumentation selection on orbital and landed missions to Mars and other terrestrial bodies.

Thermal-infrared emissivity spectra were collected at the Thermal Emission Spectroscopy Laboratory at Arizona State University. A modified Nicolet Nexus 670 FTIR interferometric spectrometer was used to collect emission measurements between 200–2500 cm^{-1} (4.0–50.0 µm). For details regarding the instrument set-up, measurement, and calibration procedures, see Ruff et al. (1997). Rock samples were heated to ~80°C for several hours in an oven and then transferred to an N_2-purged environmental chamber where the radiance was measured via the emission port of the spectrometer. Several measurements, each with a spot size of ~1 cm^2, were made for all 15 rock samples – exposing different rock faces to the detector to capture any heterogeneity in mineralogy.

Mineral abundances were then determined using a linear deconvolution method applied to the measured thermal-infrared emissivity. This method has been shown to successfully model the mineralogy for coarse particulate mixtures and rocks (Ramsey and Christensen, 1998; Feely and Christensen, 1999; Hamilton and Christensen, 2000; Rogers and Aharonson, 2008). As stated previously, this method allows for a non-destructive analysis of mineralogy with a ~5–7 vol% detection limit under optimal conditions (e.g., no interfering factors due to small particle sizes and the end-member spectral library has all the correct phases present) (Ramsey and Christensen, 1998; Feely and Christensen, 1999; Hamilton and Christensen, 2000) and a rapid sample-preparation, measurement, and modeled mineralogy turnaround time. This method separates the input emissivity spectrum into its constituent mineral components using a nonnegative linear least squares fitting routine and a library of known laboratory spectral end-members (e.g., Rogers and Aharonson, 2008). Given that the modeled spectrum is dependent on the spectral library used, if a mineral present in the experimental sample is not included in the spectral library, then the modeled mineralogy will not be consistent with the sample's actual mineralogy. Because of this, a large spectral library was used, with care to use multiple polymorphs for expected end-members. A total of 73 library spectral end-members, including six separate serpentine spectra were used for this study (**Supplementary Table 5.15**). It should be noted that the spectral library will likely never contain the full range of spectral end-members within the measured sample, given the potential diversity of compositions.

3.2.1.2 Near-Infrared

Near-infrared reflectance measurements are sensitive to a broad range of hydroxylated and hydrated mineral phases, carbonates, and Fe-bearing phases. Absorptions due to OH^- and H_2O generally occur near ~1.40 and 1.90 µm for most hydrated phases and are therefore not diagnostic of a specific phase. However, metal cation-OH absorptions are present at slightly longer wavelengths (~2.10–2.40 µm), and their shape and wavelength absorption center can often be used to uniquely identify specific phases. For example, the reflectance spectra for the Mg-rich polymorphs of serpentine have a unique shallow 2.10–2.12 µm absorption with an asymmetric absorption centered at 2.35 µm. The identification of these absorption features in NIR reflectance spectra, in combination with the 1.40/1.90 µm OH^-/H_2O hydration absorptions, can be used to uniquely identify and distinguish the presence of serpentine from other hydrated phases (e.g., Ehlmann et al., 2010).

Visible and near-infrared (VNIR) reflectance spectra were collected at the Department of Earth and Space Sciences at the University of Washington using a portable FieldSpec4 HiRes spectroradiometer with a spectral range of 0.35 to 2.50 µm. Radiance was collected with a 25° full conical angle fiber-optic cable mounted to a pistol grip aimed ~2 cm from the sample. Samples were illuminated using a standard heat lamp to increase the measured signal and stray light was limited by covering laboratory windows and acquiring measurements after sunset. Like the acquisition of the TIR emitted radiance, measurements were taken from multiple spots of ~2 mm^2 due to the heterogeneity of most samples. Data were calibrated using a spectralon calibration target and reflectance was calculated using RS^3 Spectral Acquisition and ViewSpec Pro software.

3.2.2 Mars Dataset from the Compact Reconnaissance Imaging Spectrometer for Mars (CRISM)

CRISM is a hyperspectral visible- and near-infrared imager onboard the Mars Reconnaissance Orbiter (MRO) with 544 spectral bands between ~0.4 and 4.0 µm (Murchie et al., 2007). CRISM has multiple observation modes with several spectral and spatial samplings. The alteration phases we are interested in for this study have been identified using full-resolution short and targeted (FRS and FRT) images with a spatial sampling of ~20 m/pixel and half-resolution short and long (HRS and HRL) images with a spatial sampling of ~40 m/pixel. For this study, we focused on examining CRISM images in locations where previous studies have identified serpentine-bearing phases, as well as other low-grade alteration phases. Furthermore, we performed automated factor analysis and target transformation analyses (Malinowski, 1991; Bandfield et al., 2000; Thomas and Bandfield, 2016) on all CRISM FRT, FRS, HRL, and HRS images acquired after 2011 (80 in total; see **Supplementary Table 5.16**), as these images have not yet been described by previous studies with respect to phases associated with serpentinization. The use of factor analysis and target transformation allows for the rapid identification of the dominant spectral end-members within an image and reduces random noise. These techniques have been shown to be useful for these types of studies with CRISM data (e.g., Thomas and Bandfield, 2013, 2016; Thomas et al., 2014).

CRISM images were corrected for atmospheric gas absorptions using the scaled volcano-scan method described by McGuire et al., (2009) with additional atmospheric correction techniques adapted from the current CRISM Analysis Tool (CAT) v.7.2.1. Spectral index maps were created in a manner like that described by Pelkey et al. (2007) and Viviano-Beck et al. (2014). Spectral indices map the strength of specific spectral features that are indicative of particular phases across a CRISM image, allowing for the rapid analysis of the data. Areas of interest within a given image were then further investigated by evaluating I/F (the radiance observed by the CRISM detector divided by the solar irradiance at the top of the martian atmosphere and is equivalent to reflectance) spectra and spectral ratios to confirm the presence or absence of the spectral feature(s) of interest. Spectral ratios were created by taking a pixel average of I/F values for an area of interest and dividing it by the I/F average for a region considered spectrally neutral (or spectrally known) within the same image columns, to reduce the effects of image striping on the spectral ratios.

3.3 MEASUREMENTS AND OBSERVATIONS

3.3.1 Lost City Hydrothermal Field Measurements

3.3.1.1 Thermal-infrared Measured Emissivity

Measured TIR emissivity spectra for the Lost City samples show well-defined absorption features that confirm the basic bulk mineralogy for most of the samples and clearly separate the previously defined rock types from one another (**Figure 3.3**, **Figure 3.4**, and **Figure 3.5**). Most spectra indicate a mixed composition, with multiple phases present.

“Carbonate” rock type spectra show a broad absorption with an emissivity minimum near 262 cm^{-1} (~38.2 µm), a distinct narrow absorption at 864 cm^{-1} (~11.6 µm), and a broad and flat bottomed absorption near 1512 cm^{-1} (~8.7 µm). This spectral shape is most consistent with a rock dominated by aragonite based on the shapes of the measured 1512 and 262 cm^{-1} absorptions (**Figure 3.3**). The “pelagic top-layer” rock type, has low signal-to-noise emissivity spectra due to low temperatures related to the low thermal conductivity of the fine-grained porous samples. Samples show likely absorptions near 320 cm^{-1} (~31.3 µm), and a weak, narrow absorption near 886 cm^{-1} (~11.2 µm). These absorptions are more consistent with calcite compared to the other carbonate phases within our spectral library (e.g., magnesite, dolomite) (**Figure 3.3**).

Emissivity spectra for the “talc-rich fault rock” have three apparent absorptions with minima at 1035, 673, and 467 cm^{-1} (~9.6, 14.8, 21.4 µm). This spectrum is similar to laboratory spectra of talc, with the exception of the 1035 cm^{-1} absorption. Talc has an emissivity minimum shifted to longer wavenumbers, 1062 cm^{-1}, consistent with a mixed end-member spectrum (**Figure 3.4**a). “Gabbro” rock type spectra (e.g., Sample #2) show two broad absorptions, one centered near 1071 cm^{-1} (~9.3 µm) and the other centered near 492 cm^{-1} (~20.3 µm), broadly consistent with amphibole and feldspar phases (**Figure 3.4**b).

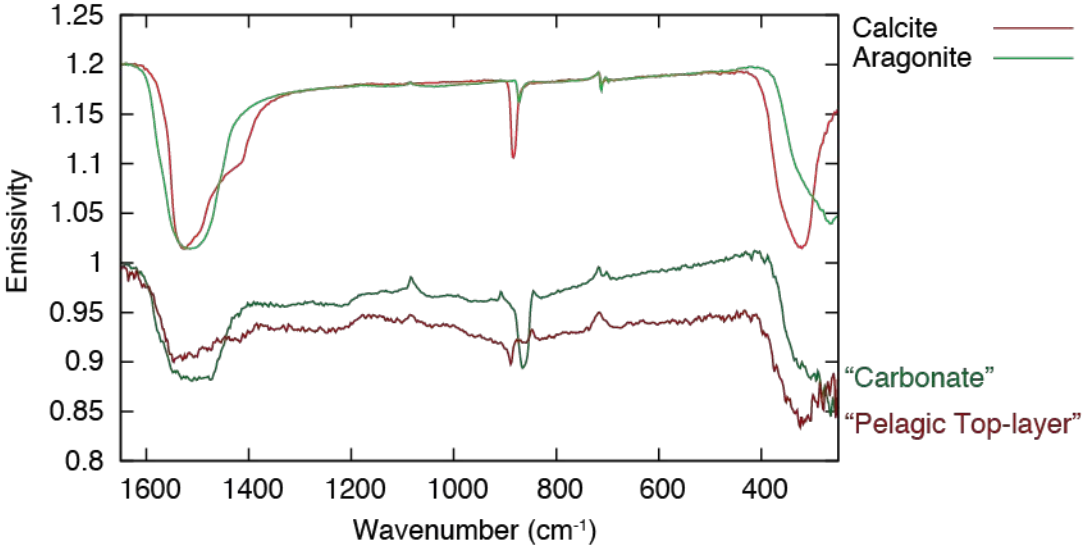

Figure 3.3. Thermal-infrared emissivity measurement for “carbonate” and “pelagic top-layer” samples compared to end-member library spectra for calcite and aragonite. “Carbonate” measurements match best with library calcite spectra, while “pelagic top-layer” measurements match best with library aragonite spectra.

Emissivity spectra for the “amphibole-rich fault rock” type show two broad absorptions and two minor absorptions. A broad asymmetric absorption occurs at high wavenumbers, with an emissivity minimum of ~996 cm^{-1} (10.0 µm), two minor absorptions at 757 and 684 cm^{-1} (~13.2

and 14.6 µm), and a broad absorption with an emissivity minimum at 529 cm^{-1} (18.9 µm). The emissivity spectrum for the “amphibole-rich fault rock” closely matches tremolite spectra from our library (**Figure 3.4**c).

Lost City “serpentinite” rock types showed the most TIR spectral variability. Five different spectral types are distinguished across the five different “serpentinite” rock samples (**Figure 3.5**). Samples #1, 6, 8, and 9 showed “serpentinite” spectral Type A, which has three broad absorptions centered near 978 cm^{-1} (~10.2 µm), 632 cm^{-1} (~15.8 µm), and 455 cm^{-1} (~22.0 µm). Different surfaces of Sample #4 show spectral types B and C. Type B has three dominant absorptions, a narrow absorption near 1035 cm^{-1} (~9.7 µm), a minor absorption near 641 cm^{-1} (~15.6 µm), and a

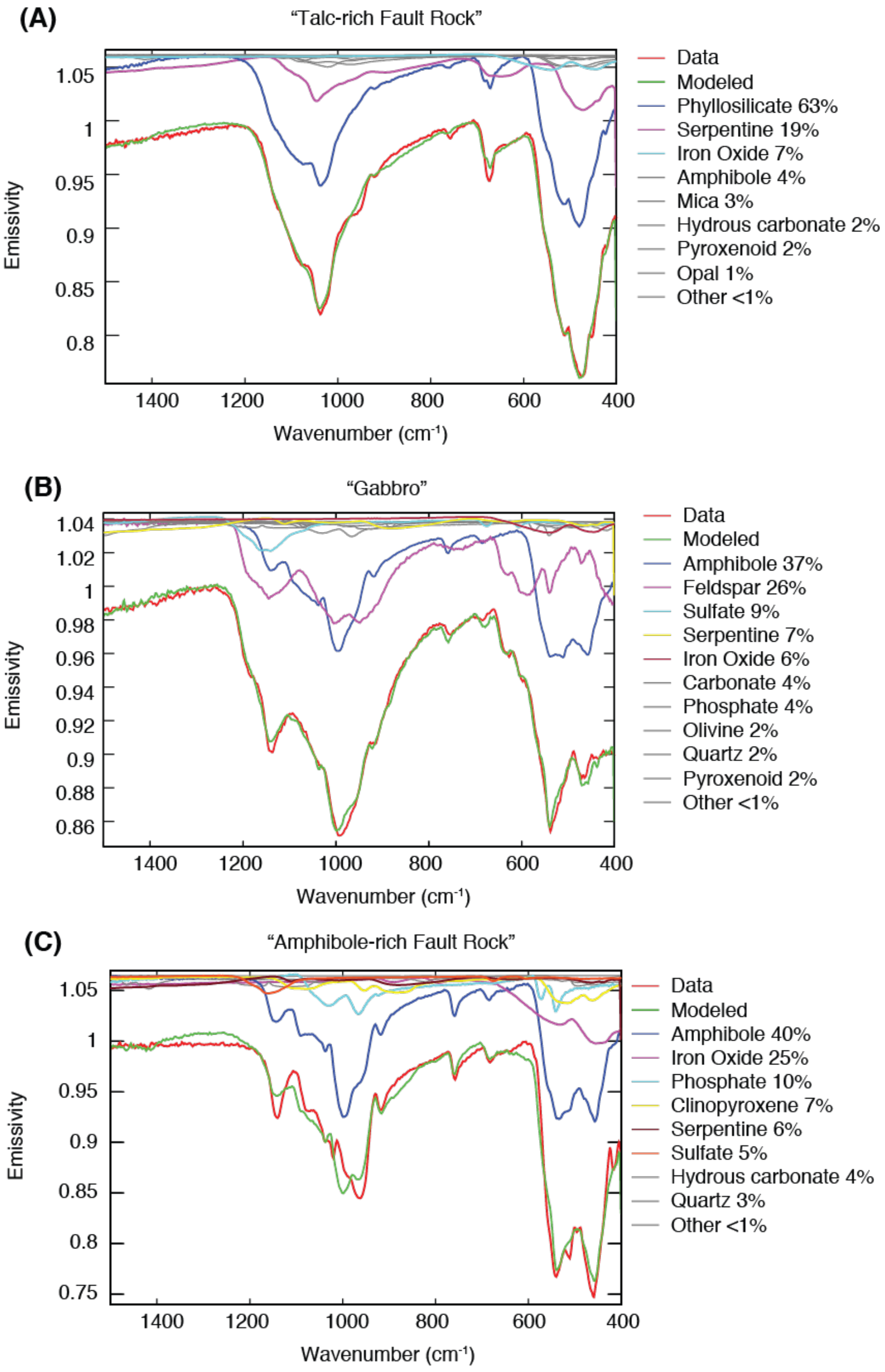

Figure 3.4. Deconvolution results for non-"serpentinite" Lost City samples. Any mineral group with abundances calculated to less than 5% have been grayed out.

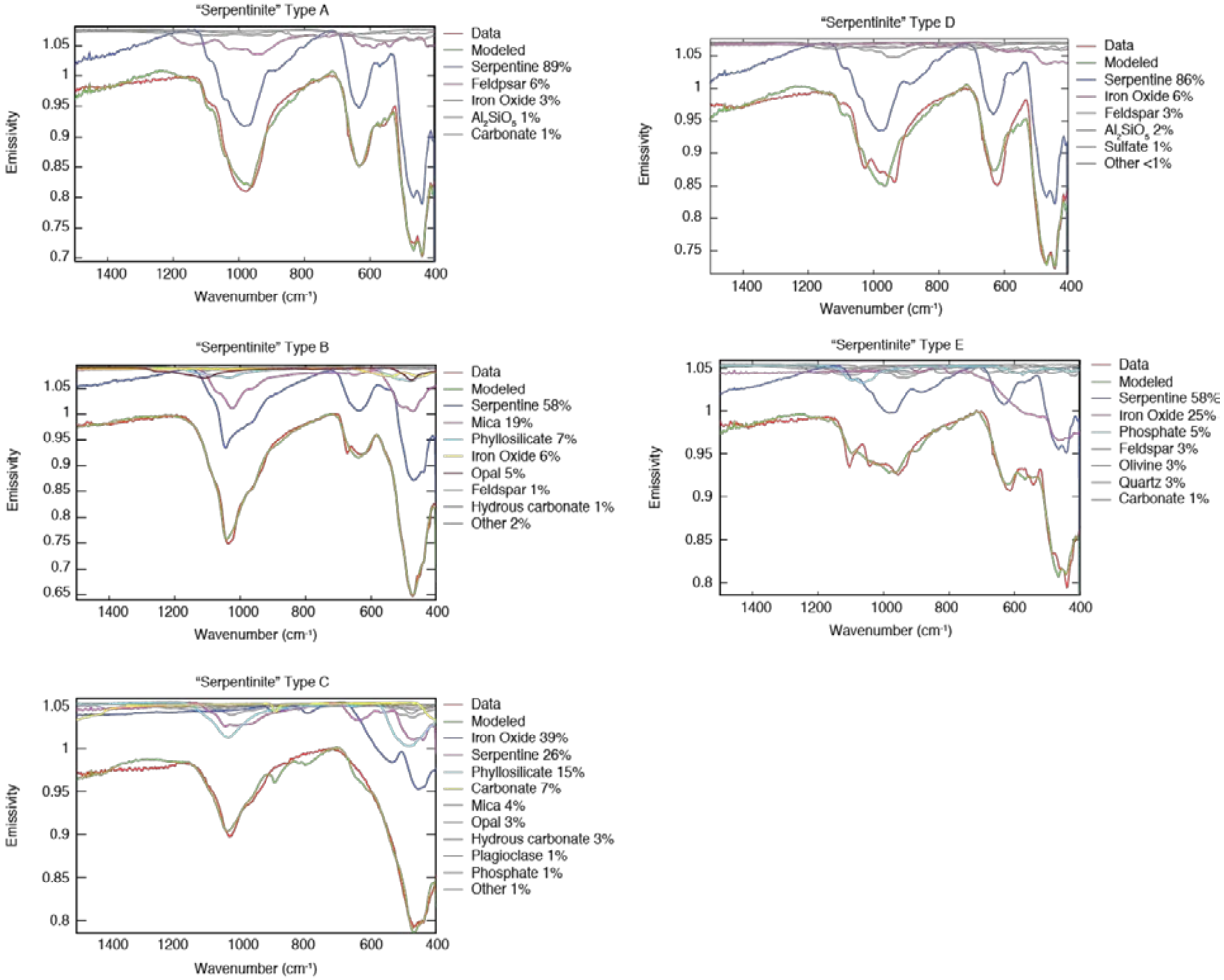

Figure 3.5. Deconvolution results for "serpentinite" Lost City samples. "Serpentinite" emissivity measurements showed the greatest spectral variability and were therefore broken-down into five Spectral Types A-E. Any mineral group abundances calculated to less than 5% have been grayed out.

deep absorption near 471 cm^{-1} (~21.23 µm). Type C has two dominant absorptions, one near 1031 cm^{-1} (~9.7 µm) and the other near 455 cm^{-1} (~22.0 µm). Only Sample #8 shows spectral Type D with three major absorptions; the first, a wide absorption centered near 983 cm^{-1} (~10.2 µm), followed by two narrow absorptions near 620 and 455 cm^{-1} (~16.1 and 22.0 µm). Lastly, Sample #9 shows spectral Type E with a broad, flat bottomed absorption near 1017 cm^{-1} (~9.8 µm), and three absorptions near 616, 540, and 455 cm^{-1} (~16.2, 18.5, and 22.0 µm). This variability in “serpentinite” type rocks may be attributed in particular to mineralogical heterogeneity at the scale of the spectrometer’s field of view (~1 cm^2). The “serpentinite” rocks are characterized by large veins of differing composition, gradational alteration, and variable textures (**Table 3.3** and **Figure 3.2**). All measurements showed absorptions consistent with the presence of serpentine phases with only minor differences from the serpentine end-members in our spectral library.

3.3.1.2 Thermal-infrared Deconvolution Modeling of Mineral Abundances

TIR deconvolution modeling was performed to determine mineral abundances for appropriate emissivity spectra. Deconvolution modeling was not performed on the “carbonate” or “pelagic top-layer” rocks because they were fine-grained and porous. Fine-particulate surfaces can create particle size effects in TIR emissivity spectra that cannot be modeled using the linear deconvolution model, and therefore do not produce quantitatively useful mineral abundances (e.g., Lyon, 1965; Ramsey and Christensen, 1998; Lane, 1999). However, their apparent absorptions allow for qualitative comparison to spectral library end-member samples, and the emissivity spectra can still be used to identify major phases. “Carbonate” rocks are clearly dominated by aragonite (**Figure 3.3**) as the shape and emissivity minimum for the low and high wavenumber absorptions match those of aragonite library spectra. Likewise, “pelagic top-layer” rocks are dominated by calcite (**Figure 3.3**).

All other TIR emission spectra were suitable for linear deconvolution modeling to determine quantitative bulk-rock mineral abundances. There are two different approaches to looking at these results. First, the results can be viewed in terms of the dominant contributing mineral *groups* (e.g., feldspar, amphibole, phyllosilicate) (**Figure 3.4** and **Figure 3.5**) for a given spectrum. For this study, serpentine phases (e.g., antigorite, chrysotile, and lizardite) have been separated from the phyllosilicate group and are their own stand-alone serpentine mineral group.

The data can also be viewed in terms of individual end-member abundances (**Supplementary Table 5.17**). To an extent, this allows us to understand what particular phases are contributing to the mineral group abundances observed (e.g., whether lizardite or antigorite is the dominant phase contributing to the serpentine group abundance for a particular rock sample). In general, the discriminability between mineral phases under optimal conditions is between 5-7 vol% (Ramsey and Christensen, 1998), however, associated errors and the model's ability to discriminate between mineral phases are impeded when spectral end-members have shallow, nondescript absorptions and/or when phases have similar spectral shapes. The model's ability to distinguish end-members within a given group is less than that of distinguishing between the different groups themselves, but these quantitative results still provide a first order look into what particular phases are likely contributing to the rock's spectrum.

In general, the deconvolution modeling of measured spectra show that the Lost City rock samples include variable mineralogy, but that they are typically dominated by one to two phases. The dominant end-member spectra are serpentine, tremolite (amphibole), labradorite (feldspar), and talc (**Figure 3.4**, **Figure 3.5**, and **Supplementary Table 5.17**). Mineral deconvolution results are typically in agreement with the rock types identified by previous studies (e.g., Karson et al., 2006; Boschi et al., 2007; Delacour et al., 2008).

Deconvolution results for the "talc-rich fault rocks" generally match previous descriptions of the samples, (i.e., a mixture of serpentine, talc, and amphibole (Karson et al., 2005; Boschi et al., 2007)). Mineral deconvolution shows that the measured spectra can be modeled by ~63 vol% phyllosilicate (excluding serpentine phases) and ~19 vol% serpentine phases, with nearly equal spectral contributions from all three polymorphs **(Supplementary Table 5.17**). Talc and saponite are the largest phyllosilicate contributors with approximately 42 vol% talc and 21 vol% saponite.

The deconvolution results did not include amphibole as a dominant contributor within our detection limits. However, all other dominant end-members were confirmed, adding to our confidence that the spectra are well-suited to confirm the bulk mineralogy.

Similarly, deconvolution modeling of the “gabbro” type rocks had good fits with the measured emissivity spectra. These spectra are dominated by feldspar (specifically in the form of labradorite) and amphibole (in the form of tremolite and hornblende); this is consistent with metamorphic alteration of the original gabbroic rock (**Figure 3.4**b, **Supplementary Table 5.17**). The “gabbro” spectrum also has minor spectral contributions from chrysotile (~7 vol%) (**Supplementary Table 5.17**). The estimated 9 vol% sulfate may also be consistent with the observations of sulfates in Lost City hydrothermal fluids (Kelley et al., 2005) and sulfur found in underlying mantle rocks (Delacour et al., 2008).

The “amphibole-rich fault rock” spectra were indeed dominated by 40 vol% amphibole phases, primarily in the form of tremolite and actinolite. The modeled spectrum has significant contributions from iron oxide phases (~25 vol%) and pyroxene and phosphate phases (~7 and 10 vol%, respectively). However, the model fit to the measured emissivity spectra was not ideal, especially for the broad asymmetric absorption near 996 cm^{-1} (~10.0 µm), implying that our spectral library is somewhat incomplete and does not contain all specific phases present within this sample. The overall shape of this absorption is consistent with tremolite emissivity spectra, but the measured spectrum is shifted to slightly lower wavenumbers (**Figure 3.4**c).

Lastly, the deconvolution results for the “serpentinite” samples showed that all samples were dominated by serpentine phases, but have variability in terms of the specific serpentine phases present and other mineral contributors (**Figure 3.5**) The modeled fit for “serpentinite” Type A spectrum is composed of ~89 vol% serpentine, with nearly equal contributions from lizardite and antigorite end-member spectra. “Serpentinite” Type B modeled spectrum is composed of 58 vol% serpentine, mostly in the form of lizardite, but with minor contributions from both chrysotile and antigorite, and 20 vol% mica (chlorite and biotite). Spectral Type C for the “serpentinite” samples has an elevated abundance of iron oxides (~39 vol%) in the modeled spectrum. Serpentine is the second largest mineral group contributor, with a modeled abundance of ~25 vol%, mostly in the form of antigorite. Deconvolution results show ~12 vol% saponite (phyllosilicate group). Deconvolution results for “serpentinite” Spectral Type D, show ~86 vol% serpentine, primarily composed of lizardite and antigorite (~55 and ~31 vol%, respectively). The modeled fit lacks the fine spectral structure in the measured spectrum within the broad 1000 cm^{-1} (~10.0 μm) absorption, but fits well at lower wavenumbers near ~450 cm^{-1} (~22.2 μm), and with the overall shape of the measured spectrum. Lastly, the modeled spectrum for “serpentinite” spectra Type E was composed of 58 vol% serpentine in the form of lizardite and antigorite (~40 and ~15 vol%, respectively) and ~25 vol% iron oxides. In this case, the modeled spectrum has minor spectral features that are not present in the measured spectrum but matches well with the overall shape of the measured spectrum.

Overall, the measured emissivity spectra for the Lost City rocks are consistent with the bulk-rock compositions for these samples. In addition, the deconvolution modeling showed the range of phases within a given rock type. For example, serpentine phases were found within all the silicate rock-types. Specifically, when serpentine phases were present in deconvolution results for the non-“serpentinite” rock types (i.e., the “talc-rich fault rock”, “amphibole-rich fault rock”, and the “gabbro”), they typically contained a higher concentration of chrysotile. The “serpentinite” rock types were predominately composed of lizardite followed by antigorite. In addition, the "gabbro" would be better defined as a metagabbro given its highly altered composition likely implying subsequent deformation.

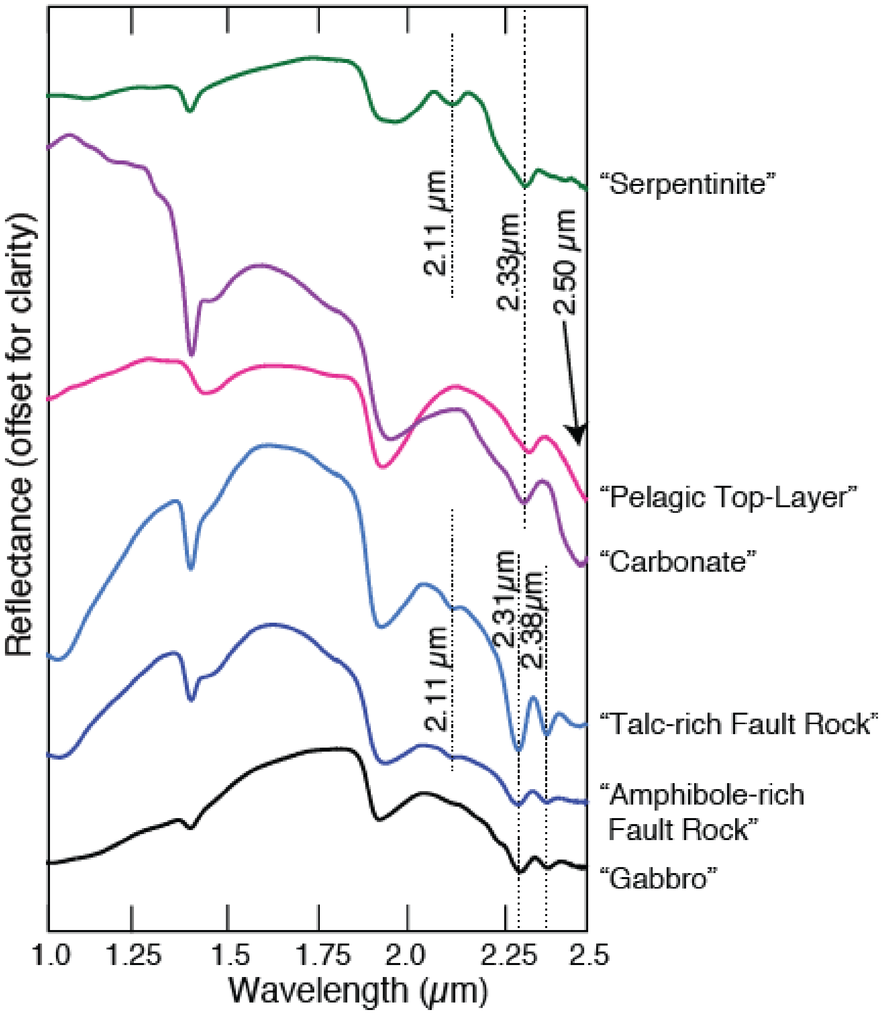

Figure 3.6. Near-infrared reflectance measurements for Lost City rock samples.

3.3.1.3 *Near-infrared Measured Reflectance*

Near-infrared reflectance spectra of the Lost City samples show absorptions typical of mafic rock types and minerals associated with serpentinization. All spectra show clear 1.4 and 1.9 μm absorptions indicative of either structurally-bound or adsorbed OH^- and H_2O (**Figure 3.6**).

Reflectance spectra for the "carbonate" and "pelagic top-layer" samples also show 1.4 and 1.9 μm hydration absorptions, a broad ~2.3 μm absorption, and part of an absorption centered near

2.5 µm (**Figure 3.6**). The combination of 2.3 and 2.5 µm absorptions are overtones and combinations due to C-O stretching and bending fundamental crystal lattice vibrations in carbonates (e.g., Gaffey, 1987). The wavelength minima of the 2.5 µm absorption can typically be used to identify the specific major metal cation (e.g., Mg or Ca), but given that this absorption is not fully sampled by the spectral range of the laboratory spectrometer, we are unable to identify the associated cation from these spectra alone. However, our TIR spectral analysis, as well as previous studies, identify these samples as dominated by aragonite and calcite (Ca-carbonates) (**Figure 3.3**).

Near-infrared reflectance spectra measured for the "talc-rich fault rock", "amphibole-rich fault rock" and the "gabbro" show similar spectral absorptions with only minor differences (**Figure 3.6**). The "talc-rich fault rock" has the deepest absorptions (highest spectral contrast) compared to the other two phases. Reflectance spectra for this sample, a compositional mixture dominated by serpentine, talc, and saponite, as confirmed by the TIR measurements and analysis, show a weak 2.1 µm absorption (consistent with serpentine) and two longer wavelength absorptions at 2.31 and 2.38 µm. The latter two absorptions can be attributed to talc, saponite, or amphibole (e.g., actinolite and/or tremolite), as these phases are difficult to distinguish spectrally at these wavelengths (e.g., Brown et al., 2010; Viviano et al., 2013) (**Figure 3.7**). However, the analysis of the TIR spectra confirms the presence of both talc and saponite phases in the "talc-rich fault rock" with small amounts of amphibole.

Both the "amphibole-rich fault rock" and the "gabbro" samples show the same two long-wavelength absorptions near 2.31 and 2.38 µm as the "talc-rich fault rock" (**Figure 3.6**). Library spectra for amphibole (e.g., tremolite) reflectance measurements show that these two absorptions would also be expected for these amphibole group phases (**Figure 3.7**). The reflectance spectra for these three rock types look extremely similar in the NIR wavelength region. Without the confirmation of bulk mineralogy derived from the TIR measurements, they would be difficult to distinguish.

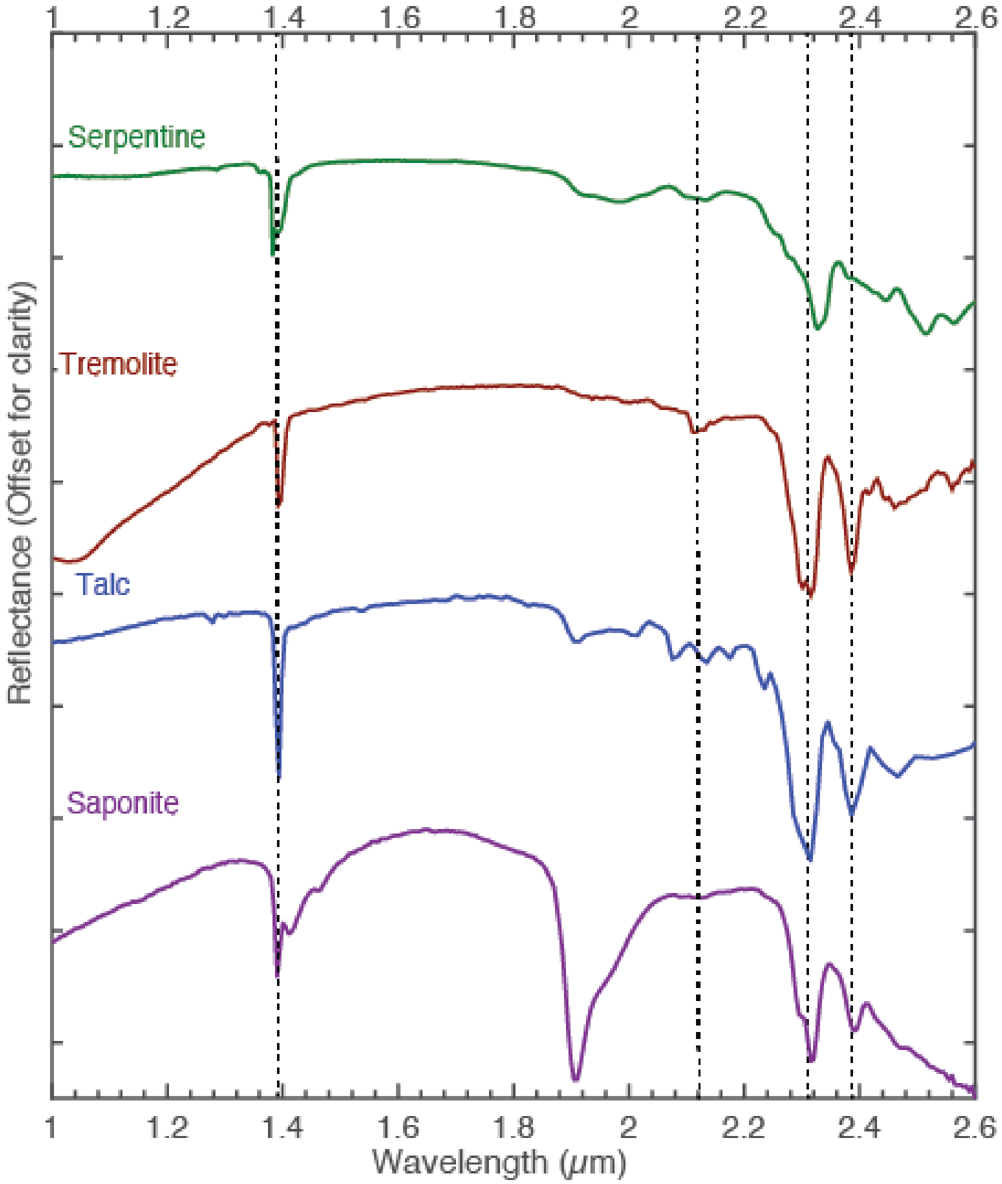

Figure 3.7. Near-infrared library spectra for serpentine, tremolite (amphibole), talc, and saponite. Serpentine can be uniquely identified by an absorption ~2.1 μm. Amphibole, talc, and saponite are difficult to distinguish spectrally in this wavelength region.

Rocks that were described as “serpentinites” by previous work, and confirmed as such by TIR emissivity analysis, show diagnostic absorptions associated with Mg-serpentine phases (i.e., lizardite, antigorite, and chrysotile) in their reflectance spectra. A unique 2.10–2.12 µm absorption in association with a sharp, asymmetric 2.33 µm Mg-OH combination band clearly indicates the presence of serpentine phases (**Figure 3.6**). Mg-serpentine phases also typically have a 2.52 µm absorption but, given the limited spectral range of the measurements, this absorption could not be fully characterized for these samples. A negative slope in the reflectance at wavelengths >2.45 µm is present and is likely due to this expected absorption.

3.3.2 Mars Observations

3.3.2.1 Low-temperature Serpentinization Mineral Assemblage in Nili Fossae, Mars

For this study, we have aggregated all observations of mineral phases in Nili Fossae associated with low-temperature serpentinization processes on Earth (**Figure 3.8**). Previous studies have documented the presence of olivine-rich basalts (Hoefen et al., 2003; Hamilton and Christensen, 2005), carbonates (Ehlmann et al., 2008; Thomas and Bandfield, 2014), and three low-grade metamorphic alteration mineral phases: serpentine, talc and/or saponite (Ehlmann et al., 2009; 2010; Brown et al., 2010; Viviano et al., 2013). We have also included additional observations of serpentine, talc/saponite, and Mg-carbonate using automated factor analysis and target transformation techniques (Thomas and Bandfield, 2016) (**Supplementary Table 5.18**). The following section describes where these phases are observed and their diagnostic spectral characteristics at near-infrared wavelengths, and these spectral observations will be directly compared with Lost City NIR measurements.

Olivine: Serpentine, talc/saponite, and Mg-carbonates have been identified in regional proximity with an extensive olivine-rich basalt unit (e.g., Ehlmann et al., 2009; Viviano et al.,

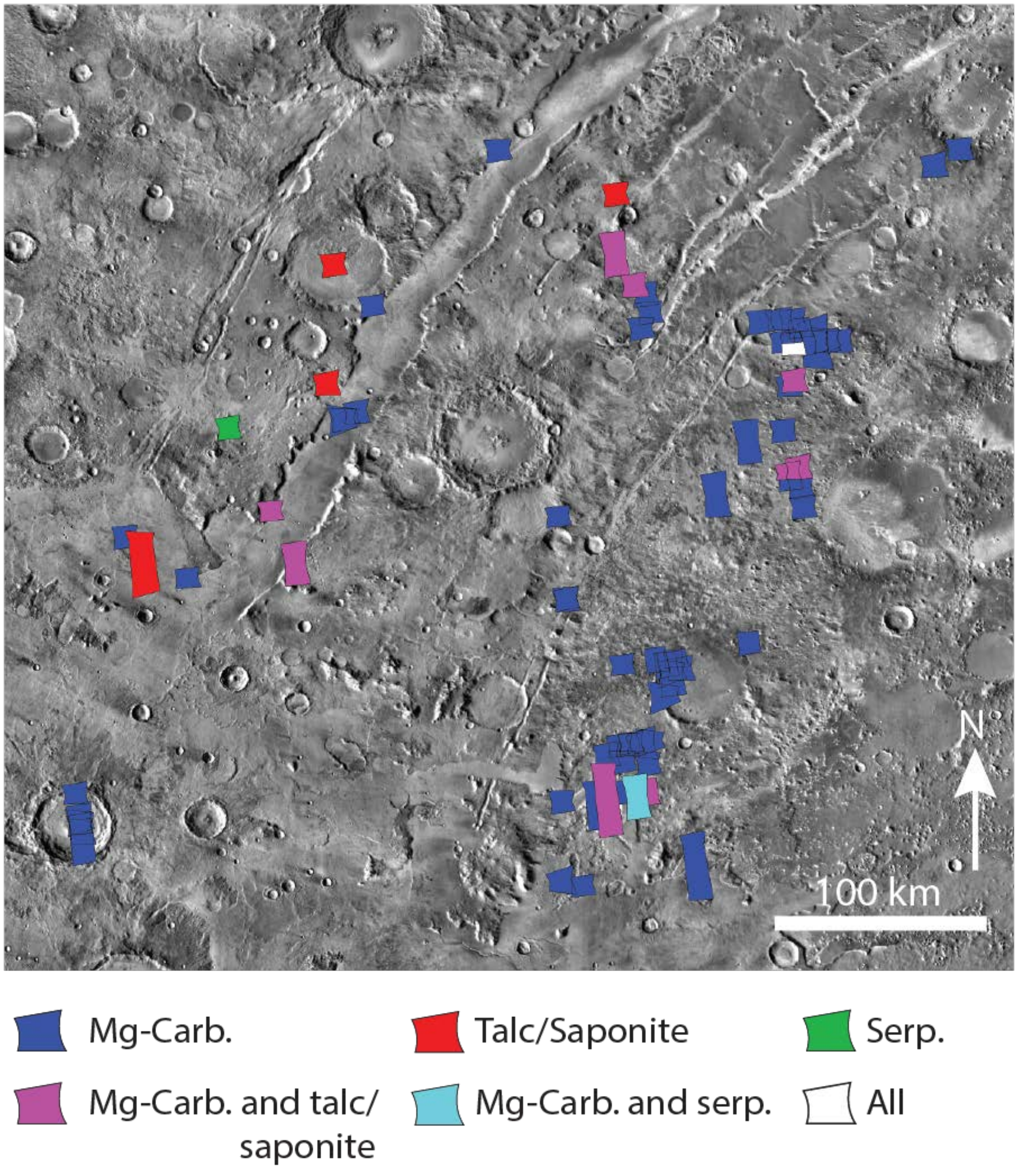

Figure 3.8. Alteration mineral distribution map for Nili Fossae on THEMIS Global Day IR mosaic background centered around 75.7°E, 20.8°N. CRISM stamp colors indicate the identification of one, or multiple, alteration phases of interest within that given CRISM image. Identifications made by this study and Ehlmann et al. (2009), Viviano et al., (2013), and Thomas and Bandfield, 2016.

2013). The largest exposures of the olivine-rich basalt spans an approximately 150 by 300 km^2 region to the northeast of the Nili Fossae troughs, though smaller exposures are observed to the west and south of the main troughs. Quantitative deconvolution analyses of emission spectra from the Mars Global Surveyor (MGS) Thermal Emission Spectrometer (TES) data indicate that this olivine-rich basalt unit contains between 20 and 30 wt.% olivine with compositions ranging from Fo_{68-75}, indicating a Mg-rich olivine end-member (Hoefen et al., 2003; Hamilton and Christensen, 2005; Koeppen and Hamilton, 2008; Edwards and Ehlmann, 2015).

The Mg content of the olivine is also confirmed by NIR spectral data from the OMEGA (Observatoire pour la Mineralogie, l'Eau, les Glaces et l'Activite; Bibring et al., 2004) and the CRISM instruments (e.g., Ody et al., 2013). CRISM ratioed-I/F spectra for this unit show a broad absorption between ~1.1 and 1.9 μm due to the ferrous component of olivine, typical of an olivine-rich basalt (**Figure 3.9**).

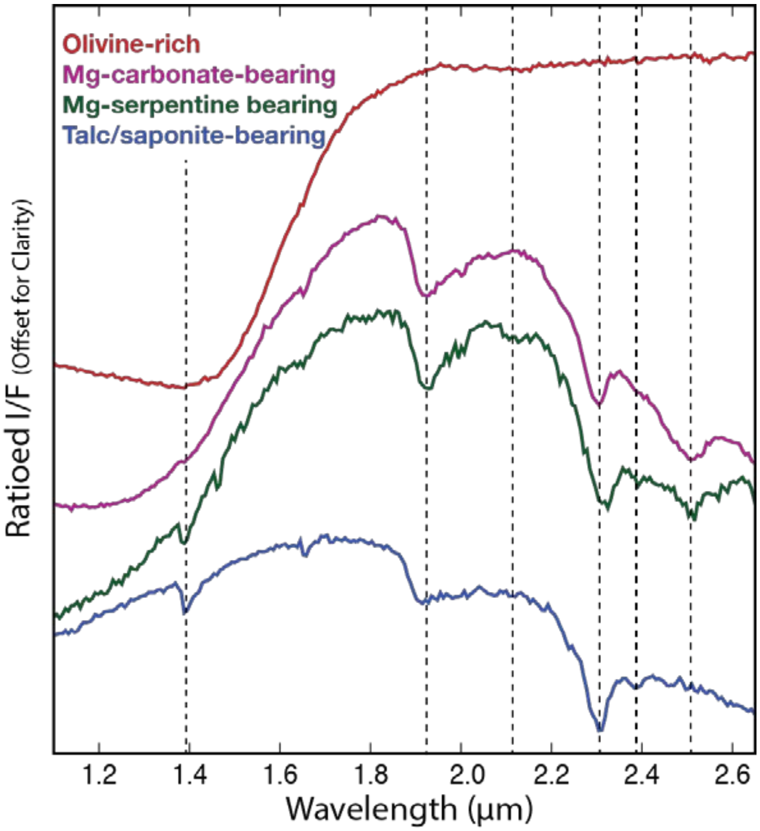

Figure 3.9. CRISM ratioed I/F spectral measurements for the spectral suite associated with low-temperature serpentinization found in Nili Fossae. Olivine and Mg-carbonate spectra from CRISM FRT00003E12_07 (Ehlmann et al., 2008), Mg-serpentine spectrum from CRISM image FRT0000ABCB_07 (Ehlmann et al., 2009), and talc/saponite spectrum from CRISM image FRT0000A053_07 (Viviano et al., 2013) (See **Supplementary Table 5.19** for pixel locations).

Carbonates: In Nili Fossae, Mg-carbonates are always found in association with the olivine-rich basalts and occupy the same stratigraphic unit as the olivine (e.g., Ehlmann et al., 2008). CRISM ratioed I/F spectra for these exposures include a broad 1.10–1.85 µm absorption consistent with the presence of olivine, a 1.9 µm combination overtone from structural H_2O, an asymmetric narrow 2.3 µm absorption, and a broader 2.5 µm absorption (e.g., Ehlmann et al., 2008) (**Figure 3.9**). The wavelength minimum for the 2.5 µm absorption is consistent with Mg-carbonate (Ehlmann et al., 2008).

Serpentine: Three serpentine-bearing exposures have been identified in the region, two by Ehlmann et al. (2009) and one by this study (CRISM FRT0002AE17_01). As for the Mg-carbonate exposures, these exposures are found within the olivine-rich stratigraphic unit. CRISM ratioed I/F spectra of serpentine-bearing surfaces contain a broad short-wavelength absorption consistent with olivine-bearing material, 1.39 and 1.90 µm absorptions consistent with hydration (bound OH^- and H_2O), and a series of longer wavelength absorptions, including a weak 2.10–2.12 µm absorption, and 2.32 µm (Mg-OH), 2.38 µm, and 2.50 µm absorptions (**Figure 3.9**). The combination of the 1.38, 2.10-2.12, 2.32, and 2.50 µm absorptions are unique to Mg-serpentine (e.g., Ehlmann et al., 2010). The 2.38 µm absorption is consistent with the presence of other Mg-phyllosilicates, like talc and saponite – or potentially amphibole.

Talc/Saponite/(amphibole?): Lastly, a phase consistent with talc or possibly saponite has been identified in isolated areas across the Nili Fossae region (e.g., Brown et al., 2010; Viviano et al., 2013). These are typically found near Mg-carbonate bearing exposures, but not necessarily co-spatially (**Figure 3.8**). Spectra for these exposures typically contain a narrow 1.38 µm absorption, a broad asymmetric 1.90 µm OH^-/H_2O absorption, a strong narrow 2.32 µm absorption, and a weaker absorption at 2.38 µm (**Figure 3.9**). It should be noted that as with the NIR laboratory spectra described in Section 3.3.1.3, it is not possible to distinguish talc/saponite from amphiboles like tremolite or actinolite using reflectance spectra at these wavelengths (**Figure 3.6** and **Figure 3.7**). As such, it is unclear whether surfaces with these spectral characteristics represent a single phase, or various combinations of these spectrally ambiguous phases.

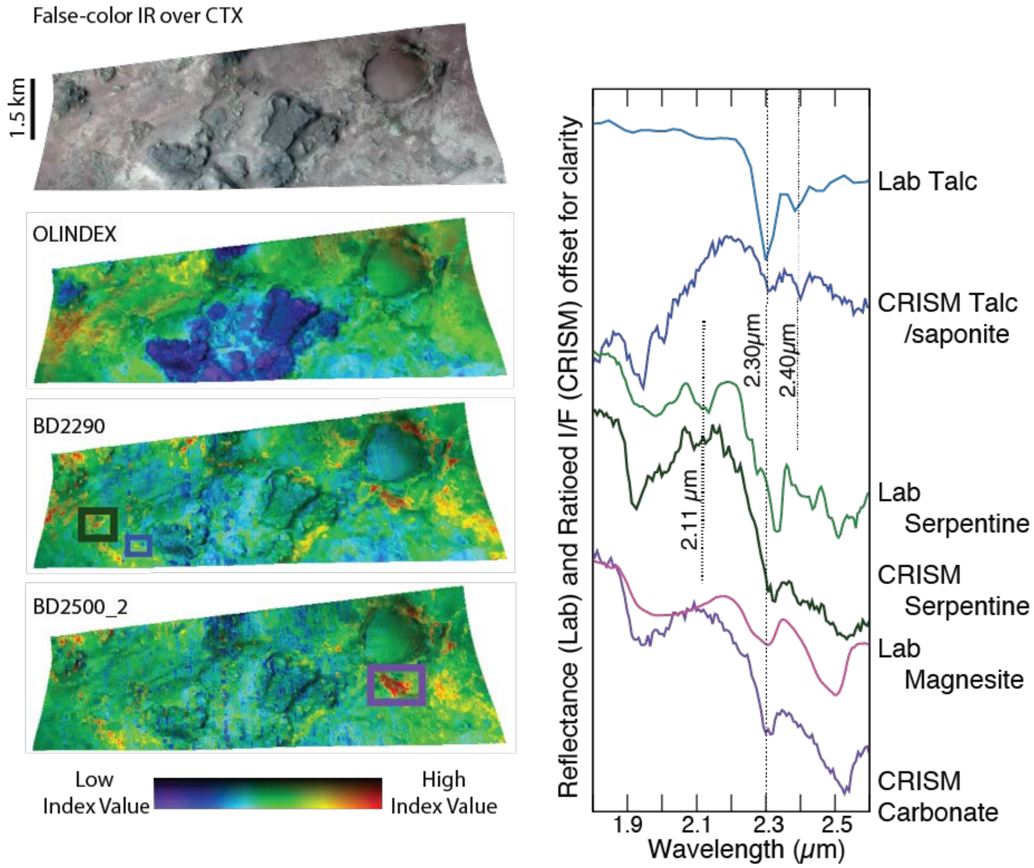

Figure 3.10. CRISM image FRS0002AE17_01 with new detections of serpentine, carbonate, and talc (+/- saponite and amphibole) in association with the olivine-rich basalt unit. See

Supplementary Table 5.19 for CRISM pixel locations for displayed spectra. False-color IR image projects CRISM wavelengths 2.53 µm, 1.50 µm, and 1.08 µm as red, green, and blue, respectively.

There is one CRISM image that contains all four spectral types (olivine, serpentine, carbonate, and talc/saponite/amphibole) within a single scene: FRS0002AE17_01 (**Figure 3.10**). The ratioed I/F spectra for the serpentine-bearing exposures in this image show a clear absorption near 2.11 µm, in addition to absorptions near 1.90 and 2.32 µm. A phase with two absorptions near 2.30 and 2.40 µm may be consistent with talc (and/or saponite and/or amphibole), but was only weakly identified by the BD2290 index, likely because its 2.32 µm absorption is relatively shallow compared to the carbonate and other Fe/Mg-smectite phases found within the image.

3.4 DISCUSSION

3.4.1 Laboratory Measurements

3.4.1.1 Usefulness of Thermal-infrared Measurements

Through this non-destructive analytical method, bulk-rock compositions of rock types from the Lost City Hydrothermal Field agree with past studies; and have been useful in providing a more detailed description of the mineralogy. This has been particularly illuminating with the “serpentinite” rock types, which show considerable variability in their emissivity spectra.

Five different spectral types were documented within the “serpentinite” rocks. Characterization of Types A and B are reproduced well with the spectral end-member library used for deconvolution modeling (**Figure 3.5**), implying that much of phases present within those rock samples were also found in our spectral end-member library. Deconvolution modeling for “serpentinite” Spectral Types C, D, and E shows general agreement with the emissivity measurements for those rocks, but the modeling either added or missed minor absorptions. In these cases, the spectral end-member library was likely incomplete, and did not include the full range of phases present within the rock samples.

Serpentine is a particular case where there is a great deal of expected variability both in terms of mineral phases and spectral characteristics. A search for thermal-infrared emissivity spectra of lizardite, antigorite, and chrysotile across spectral libraries (e.g., the U.S. Geological Survey Spectral Library (Clark et al., 2007), the Arizona State University Spectral Library (Christensen et al., 2000)) show a wide range of spectral characteristics for these phases (**Figure 3.11**), all with similar general shapes but variable detail. Similarly, our serpentinite samples, all from the same low-T hydrothermal system, show a range of observed emissivity spectra, though the overall shapes are still consistent with known serpentine spectra. Therefore, in addition to confirming that these samples are indeed serpentinites, these spectra serve as spectral end-members and demonstrate the spectral variability for this particular low-T serpentinizing environment.

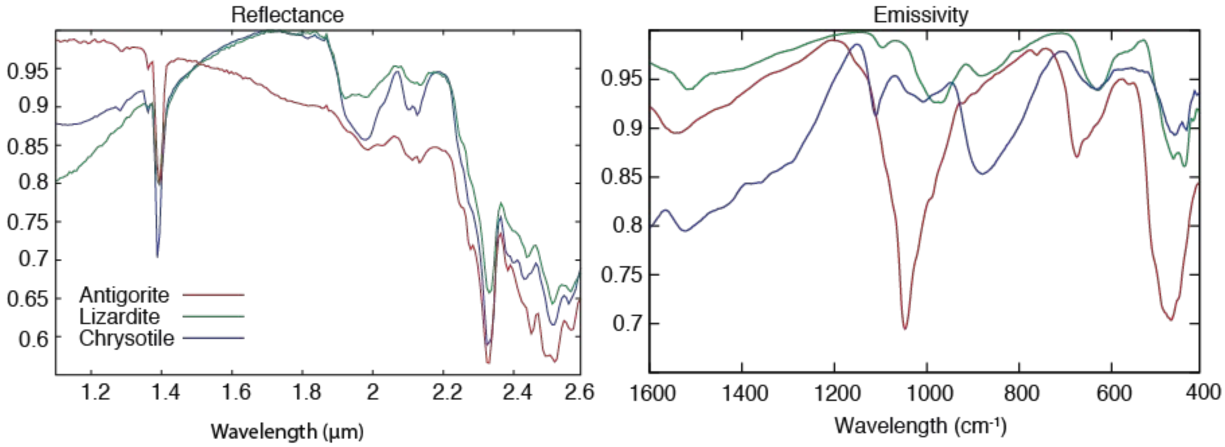

Figure 3.11. Near-infrared reflectance and thermal-infrared emissivity spectra for the three Mg-rich serpentine polymorphs. The polymorphs have nearly indistinguishable spectral absorptions in the near-infrared while having unique spectral shapes and contrast in the thermal-infrared.

3.4.1.2 Observed Patterns in Thermal-infrared Measurements

Several patterns were documented in the TIR emissivity measurements with respect to the different serpentine polymorphs and to which Lost City samples they were predominately observed. The three Mg-rich serpentine polymorphs are lizardite, chrysotile, and antigorite. Lizardite is expected to form in low-temperature serpentinizing environments where fluid temperatures are typically between 50-300°C, and the typical co-products are magnetite and H_2 (+/- brucite) (Evans 2004, 2010). Consistent with the low-temperature regime that they form in, the predominate serpentine polymorph in the Lost City "serpentinites" is lizardite.

As for lizardite, chrysotile growth is favored at low fluid temperatures, but typically under isotropic stress at the micro scale; this generally begins after the active hydration of olivine has ended (Evans, 2004). In this way, lizardite is the initial stable form of serpentine in low-temperature serpentinizing regimes, but is typically recrystallized to chrysotile when under stress, as in a tectonically active setting. Again, consistent with their tectonic and alteration history, chrysotile is typically the predominant serpentine phase in the fault rocks and metagabbro, as those rocks presumably underwent extensive tectonic stress and deformation.

Lastly, antigorite typically forms at temperatures >250°C with brucite, when rates of MgFe diffusion in olivine are orders of magnitude faster than in the low-temperature systems, such as in mantle fore-arc wedges (Evans, 2004, 2010). These increased reaction rates limit the amount of magnetite and H_2 produced (Evans, 2004). We observe modeled antigorite in several "serpentinite" spectral types in the Lost City samples, however, they are never the predominant serpentine polymorph, and this lack of antigorite has been described by others who have studied these rocks previously (e.g., Früh-Green et al., 2004). Additionally, it is common to observe naturally-occurring inter-growths of all three polymorphs (Rinaudo et al., 2003).

3.4.1.3 Observed Phases Compared to Theoretical Serpentinization Reactions

Our deconvolution results of TIR emissivity measurements are generally in agreement with expected mineral phases from theoretical serpentinization reactions (Reactions 1-3). However, notably missing from our derived mineralogy are brucite (Mg-hydroxide) and magnetite (Fe-oxide). Both phases were included in our end-member spectral library but neither was modeled in the deconvolution results. There are several reasons why those phases might not be reflected in the modeled mineralogy. Magnetite has high emissivity values in the thermal-infrared with shallow absorptions near 600 and 300 cm^{-1}. As such, it is difficult to detect magnetite using this technique. Conversely, brucite has distinct spectral absorptions in the thermal-infrared, however, brucite is typically described in previous studies as being found within the carbonate-bearing rocks (Ludwig et al., 2006) but we were unable to use the deconvolution model to determine mineral abundances for these samples due to textural effects. Brucite has been shown to be present within those samples from past studies (Ludwig et al., 2006) and its presence, as detected by others, is consistent with the generalized serpentinization reactions (Reaction 3).

Deconvolution models of the Lost City rock samples indicate significant amounts of talc. Though not a direct product of serpentinization, talc-rich rocks are commonly found in association with serpentinites and have been shown to be present within the Lost City rock assemblages (e.g., Früh-Green et al., 2004). On Earth, the most abundant occurrence of talc is in metamorphosed ultramafic rocks, such as those at the Lost City (Evans and Guggenheim, 1988). Talc is expected to form as a product of the alteration of serpentine by dissolved silica (e.g., Moore and Rymer, 2007) and tends to breakdown at ~800 °C (Evans and Guggenheim, 1988).

3.4.1.4 Near-infrared Spectral Ambiguity

A notable difference between the near- and thermal-infrared measurements is their ability to distinguish between the different rock types and the spectral variability within a given rock type. For example, the "serpentinite" rock types show five different spectral types in the thermal-infrared (**Figure 3.5**), all consistent with a serpentine-rich rock, but with notable variability. The five "serpentinite" rocks measured in the near-infrared have consistent spectral absorptions with limited variability (**Figure 3.6**). The three Mg-serpentine polymorphs that make up the "serpentinite" rocks are distinguishable and identifiable in the thermal-infrared but are spectrally ambiguous in the near-infrared portion of the spectrum. This indicates the importance of having both measurements to properly characterize the suite of minerals within this set of samples.

Similarly, the "talc-rich fault rock", "amphibole-rich fault rock", and the "gabbro" have nearly identical spectral characteristics in the near-infrared portion of the spectrum. Talc and amphibole are known to contain similar, deep spectral absorptions in the near-infrared portion of the spectrum (**Figure 3.7**). In the case of the "gabbro", the observed absorptions are likely due to the ~35 vol% amphibole and serpentine phases modeled in the rock composition (**Supplementary Table 5.17**). The thermal-infrared emissivity measurements were used to determine the specific composition for these three rock types, and the near-infrared measurements indicate the presence of H_2O/OH^- and OH^- stretch and $Mg\text{-}OH^-$ bending modes (e.g., in Mg-phyllosilicates or from hydroxyl in amphiboles).

3.4.2 Mars Observations

3.4.2.1 Compositions as Described by CRISM

As presented by past studies, the mineral assemblages observed in Nili Fossae are consistent with low-temperature hydrothermal alteration of an ultramafic protolith (e.g., Viviano et al., 2013). In particular, the spectral detection of phases consistent with serpentine and magnesite are unambiguous and clearly indicate their presence within the rock record in Nili Fossae. The detection of a phase with absorptions at 1.4, 1.9, 2.3, and 2.4 µm (**Figure 3.9** and **Figure 3.10**) has been attributed to the Mg-rich smectite saponite (e.g., Ehlmann et al., 2009; Brown et al., 2010) and to talc (e.g., Brown et al., 2010; Viviano et al., 2013). As we have shown in earlier sections, talc, saponite, hydroxylated/hydrated amphibole are spectrally ambiguous in the near-infrared portion of the spectrum (**Figure 3.7**). Viviano et al. (2013) argue that talc and saponite are not spectrally ambiguous and that it is possible to differentiate the two phases based on the shape and spectral contrast of the 2.3/2.4 µm absorptions, and they argue that the surfaces in question in Nili Fossae are talc-bearing. Viviano et al. (2013) also argue that the presence of talc is consistent within the greater mineralogical context of the region in that it can form through the carbonation of serpentine to form talc and magnesite (e.g., Viviano et al., 2013).

Despite this spectral conundrum, the spectral ambiguities observed in Nili Fossae are like those we observe in the Lost City rocks. Mg-rich saponite typically forms via the hydrothermal alteration of basalt (Evans and Guggenheim, 1988). Given that there is abundant olivine-poor basalt in the Nili Fossae region (e.g., Amador and Bandfield, 2016) within the same stratigraphic column as the observed talc/saponite exposures, it is possible that saponite formation could occur. In addition, talc and saponite have been shown to grow within mixed-layered structures at submarine hydrothermal sites on Earth (Cuadros et al., 2008; Michalski et al., 2015), making their spectral disambiguation even more difficult and showing that the two phases do form together. Similarly, we have shown with our Lost City rock samples that talc and saponite can both be significant constituents of rocks that form in serpentinizing systems as is the case with the “talc-rich fault rock” (**Supplementary Table 5.17**). So while the distinction of whether this spectral signature in Nili Fossae is due to talc or saponite has specific implications for the alteration trajectory of these rocks, we have shown that these phases are not mutually exclusive and are both well represented within low-temperature serpentinizing systems on Earth.

Lastly, it is important to note that with the CRISM NIR data alone, it is not possible to determine if the ambiguous 1.4/1.9/2.3/2.4 µm spectral signature is due to amphibole phases like tremolite or actinolite. As we have shown with the Lost City rock samples, the “talc-rich fault rock” and “amphibole-rich fault rock” look nearly identical in near-infrared measurements. Amphiboles have been detected in martian meteorites (e.g., Williams et al., 2014) and are possibly present on the surface of Mars. They are potentially present as spectral mixtures of saponite and hornblende (Carter et al., 2013) but otherwise have not been discussed extensively in the martian literature. In the case of Nili Fossae, Viviano et al. (2013) note the spectral ambiguity between talc and actinolite, but argue that the presence of amphibole within the context of the mineral assemblage observed in the region is unlikely. While we agree that talc (and/or talc + saponite) are likely at least partially for the ambiguous spectral signature in Nili Fossae given the nearby presence of magnesite, it is important to note that amphibole does fit into the common assemblage of minerals formed during serpentinization, as shown by the Lost City rock samples.

3.4.3 Spectral Differences between Measurements from the Lost City Hydrothermal Field and Nili Fossae, Mars

There are some clear differences between the spectral characteristics, and therefore mineralogy, of the Lost City terrestrial rock samples and the surface exposures in Nili Fossae, Mars. First, the Nili Fossae assemblage has abundant olivine still present within the stratigraphic section. Interestingly, numerous reactants and products of serpentinization-associated reactions are still present. The fact that abundant olivine remains, unaltered to serpentine (or magnesite), indicates that the serpentinization reactions in the area never went to completion, perhaps indicating a limited period of alteration and/or volume of water. Comparatively, the Lost City serpentinites and associated rocks used for this study no longer show signs of their unaltered protolith, and the most mafic rock in the group acquired is a still an extensively altered metagabbro. This, in-part, is likely a sampling bias for the Lost City rock samples, as the rocks acquired by the DSV Alvin were most often pulled from surface outcrops. However, cores drilled from the southern wall of the Atlantis Massif during the 2016 IODP Expedition 357 show evidence for variable serpentinization with depth (Früh-Green et al., 2016).

Another mineralogical difference between the Lost City rocks and Nili Fossae surface exposures is the presence of different major-metal cations in their respective carbonates. The Lost City carbonates are dominated by either Ca-rich calcite or aragonite depending on whether the rock was formed via the accumulation of pelagic material ("pelagic top-layer rocks", dominated by calcite) or via the precipitation of aragonite as high-pH hydrothermal fluids encounter seawater ("carbonates", dominated by aragonite), though it should be noted that the aragonite-rich chimney rocks revert to calcite over-time (Ludwig et al., 2006). The Nili Fossae carbonate-bearing exposures are Mg-rich, and spectrally consistent with magnesite. There are several potential scenarios for the formation of the martian carbonate in Nili Fossae; one is via the direct alteration of the Mg-rich olivine in the area by near-surface water (Ehlmann et al., 2008). Another potential formation mechanism is the carbonation of the serpentine-bearing rocks (Viviano et al., 2013). This process would not only produce the Mg-rich magnesite but also produce talc, which is also observed near the Mg-carbonates in the region. The carbonates in Nili Fossae and the Lost City Hydrothermal Field were likely produced and controlled by separate processes. The Lost City carbonates used for this study were buffered and controlled by the seawater present at the seafloor/ocean-water interface, while the carbonates produced in Nili Fossae, Mars were likely controlled by the continued subsurface hydrothermal alteration of the bedrock. This is one clear example of where the environmental analog between the Lost City and Nili Fossae is not as strong given the evidence currently at hand.

3.4.4 Implications for Serpentinization in Nili Fossae, Mars

3.4.4.1 Physical Characteristics of Nili Fossae and its Susceptibility to Serpentinization

The Nili Fossae region of Mars is only one of several extensive exposures of olivine-rich basalt on the planet (e.g., layers in Valles Marineris, Terra Tyrrhena, the rim of Argyre Basin (Ody et al., 2013)). However, it is the only region that shows spectral evidence for serpentine in association with other mineral phases known to form in a serpentinizing system. There are several factors that may have contributed to serpentinization in this area beyond just the necessary olivine-rich protolith. For example, the formation of the Nili Fossae likely occurred in association with the Isidis Basin impact event, creating a highly fractured terrain. In addition to the large, regional-scale fractures that make up the main Nili Fossae troughs, the basement phyllosilicate-bearing unit shows abundant local-scale ridges and fractures. They are typically hundreds of meters long and tens of meters wide and appear to be the source of the Fe/Mg-phyllosilicate spectral signatures (Mangold 2007; Mustard 2007, 2009; and Ehlmann et al., 2009, 2010).

Work by Saper and Mustard (2013) shows that the orientation of most of the small-scale ridges and fractures line up with the larger orientation of the main Nili Fossae troughs, implying that these ridges were emplaced by the same mechanism as the large-scale graben around the same time. These local-scale faults, fractures, and dikes, in addition to the regional-scale fossae, would have allowed for substantial fluid circulation pathways. Additionally, there has likely been a long-lived heat-source in the region, induced by both the Isidis Basin impact event as well as the Syrtis Major volcanic province. This early fractured bedrock, combined with the olivine-rich protolith would have created an environment suitable for the initiation of serpentinization. The serpentinization reactions can be self-sustaining given their exothermic and volume-increasing nature, and could produce fresh surface area for continued alteration (e.g., Lowell and Rona, 2002) until the protolith (olivine) is consumed. This volume-increasing nature can also seal the rocks from further alteration, so a region with a previously fractured lithology makes it particularly prone to sustained serpentinization over time. Therefore, in addition to the spectral (and subsequently the mineralogical) evidence for serpentinization occurring in Nili Fossae, this region was likely to be uniquely susceptible to these reactions. It is important to note, however, that the extensive remnants of olivine in the region imply that the serpentinization reactions did not go to completion and that water was likely a limiting resource in driving these reactions forward.

3.4.4.2 Mineralogical Evidence for Serpentinization

The spectra acquired from Nili Fossae are similar to those measurements acquired from rocks collected at the Lost City Hydrothermal Field. As noted by McSween et al. (2015), rather than looking for a single mineral that might be a “smoking gun” for a particular geochemical environment, the search for specific mineralogical *assemblages* can provide greater constraints on the environment in question and narrow the search for once habitable environments. Furthermore, the observation of a suite of minerals indicative of a formation environment provides greater confidence that the environment was indeed present. Reliance on the detection of a singular spectral signature indicative of just one mineral phase is not as robust a result since the interpretation can be more easily confounded by spectral ambiguities and data artifacts.

At both the Lost City Hydrothermal Field and the Nili Fossae analyses conducted in this study document Mg-serpentine phases, carbonate-phases, and talc, saponite, and/or amphibole. Additionally, in Nili Fossae abundant olivine has been documented, a necessary reactant for the serpentinization process, as well as a geologic setting (described in the Section 3.4.4.1) that would favor the transport and circulation of hydrothermal fluids. Apart from serpentine, the other phases documented in Nili Fossae *could* form under non-serpentinizing conditions. For example, the Mg-carbonate could be the direct product of near-surface aqueous alteration of the olivine-rich basalt. Similarly, saponite can form via the hydrothermal alteration of olivine-poor basalt. However, the presence of all these phases together within the same stratigraphic unit, and at times within the same CRISM image, likely implies a connected geochemical story. This appears most consistent with sustained hydrothermal alteration of an olivine-rich protolith in the eastern portions of the Nili Fossae. This alteration triggered serpentinization at the subsurface interface between the olivine-rich basalt and underlying olivine-poor, phyllosilicate-bearing basalt. The serpentine-enriched bedrock was subsequently altered by carbonation to talc and magnesite, consistent with their co-spatial occurrence across the eastern region of the Nili Fossae.

An important consideration is the timing of the serpentinization reactions. The alteration must have occurred after the emplacement of the olivine-rich basalt unit approximately 4 Ga (Wichman and Schultz, 1989). According to the model put forward by Viviano et al. (2013), the suite of alteration minerals that we have described here likely formed prior to the emplacement of the Hesperian-aged Syrtis lava flows, approximately 3.7 Ga. The altered olivine-rich unit has subsequently been eroded by episodic aqueous processes, evidenced by channel networks that cut through the Hesperian-aged lava flows, and atmospherically-driven processes (e.g., dunes and dust abrasion), exposing the suite of alteration minerals today.

3.4.4.3 Implications for Habitability of Nili Fossae

We have shown that the spectral signatures and mineralogical suites present at the Lost City Hydrothermal Field on Earth are similar to those documented in the Nili Fossae region of Mars. This suite of minerals is unique to serpentinization where the reduction of H_2O in the presence of Fe^{2+} generates H_2. Molecular hydrogen is particularly interesting from an astrobiological standpoint because it is a strong electron donor that can drive the synthesis of organic molecules in Fischer-Tropsch-type reactions (e.g., Holm and Charlou, 2001; McCollom and Seewald, 2007). Organic compounds such as various hydrocarbons, formate, and acetate are present at elevated concentrations in Lost City fluids (Proskurowski et al., 2008; Lang et al., 2010). The abiotic production of organic compounds is significant because they can be used as precursors to important biological polymers, and hydrothermal chimneys such as those at Lost City can act as efficient incubators and reaction vessels (Stüeken et al., 2013; Kreysing et al., 2015).

Furthermore, H_2 is directly used as an electron donor in the metabolism of many chemoautotrophic organisms (e.g., Nealson et al., 2005; Schulte et al., 2006; Stüeken et al., 2013). For example, methanogens, which are abundant in Lost City chimneys (Schrenk et al., 2004; Brazelton et al., 2011), use H_2 to fix CO_2 and produce CH_4 and H_2O. This pathway is thought to be one of the most ancient metabolic strategies (Fuchs, 2011), and the catalytic cores of enzymes in this pathway resemble minerals found in hydrothermal systems (Russell and Martin, 2004). These minerals can catalyze some steps of carbon fixation on their own without the scaffolding provided by enzymes, suggesting potential links to prebiotic chemistry (Cody, 2004; Stüeken et al., 2013).

Many of the key pieces necessary for life are produced in rock-hosted serpentinizing systems: liquid water, energy source, reducing power, and abiotically-produced hydrocarbons. Given the evidence for serpentinization in Nili Fossae, it is possible to say that it could have had a habitable subsurface environment present at some point in its history. Additionally, the fractured nature of the Nili Fossae terrain would have provided local-scale faults and fractures for alteration fluids to concentrate. These fluids would likely have been enriched in H_2 and low-order organics, similar to fluids currently venting from chimneys at the Lost City Hydrothermal Field on Earth. The remnants of these fractures and faults would be compelling places to search for potential biosignatures from any hypothetical life that may have been present in the past, or simply to better understand the range of abiotically produced organic compounds on Mars.

It should be acknowledged that it is known that serpentine can form without the production of H_2 (Reactions 2 and 3), however in a natural setting with non-endmember olivine compositions (i.e., fayalite versus forsterite) it is unlikely that only Reactions 2 and 3 would occur without Reaction 1. In particular, given the known olivine composition in Nili Fossae (Fo_{68-75}; Hoefen et al., 2003; Hamilton and Christensen, 2005; Koeppen and Hamilton, 2008; Edwards and Ehlmann, 2015) we expect Reactions 1-3 to take place. In order to confirm the occurrence of H_2 production during serpentinization, future studies should search for the presence of magnetite or other Fe^{3+}-phases (e.g., Fe^{3+}-bearing brucite) in association with the serpentine, as these cannot be detected from current orbital datasets.

For many geological, chemical, physical, and biological reasons, serpentinite-hosted hydrothermal vent systems have been discussed as compelling environments for key steps in the origin of life on Earth before ~3.5 Ga (e.g., Russell et al., 2010; 2014; Stüeken et al., 2013; Sojo et al., 2016). The results of this study provide further evidence that similar geochemical systems would have been active on Mars during the same period in our Solar System’s evolution.

3.5 CONCLUSIONS

This work draws mineralogical and geochemical parallels between the Lost City Hydrothermal Field on Earth and the Nili Fossae region on Mars. There is abundant evidence for active serpentinization to have occurred in the Nili Fossae region during an important period on our own planet. Although it is not possible to determine if life inhabited serpentinizing systems on

Mars from the remote sensing data alone, habitable environments, induced by geochemical processes initiated by abundant geologic constituents, were present. There are several major geological and geochemical differences between the Lost City and Nili Fossae. For example, the initial fluid compositions were likely quite different, additionally, the Lost City Hydrothermal Field is located beneath ~800 meters of seawater and ~15 km away from a slow-spreading oceanic ridge, whereas the serpentinization occurring at Nili Fossae would likely have taken place in the subsurface with a likely limited source of water. Regardless, the fact that serpentinization reactions require such readily available starting materials, and produce biologically accessible byproducts, are what make them so compelling as a process for astrobiological study. The presence of serpentine in Nili Fossae indicates that fluid-rock reactions took place, likely implying that H_2 and abiotically-produced organic compounds were produced in the subsurface. As such, the Nili Fossae, specifically where we see the local grouping of the mineralogical suite presented here, is a compelling site to search for the evidence of past life on Mars. Equally compelling is the opportunity to study a site that parallels in geochemistry and time sites on Earth that likely led to the origin of life. Whether or not life inhabited these sites on Mars would have major implications for how and why life evolved on our own planet.

Chapter 4. **A SEARCH FOR MINERALS ASSOCIATED WITH SERPENTINIZATION ACROSS MARS USING CRISM SPECTRAL DATA**

This chapter is in-preparation for submission to the journal Icarus
Co-authored by: Elena S. Amador, Joshua L. Bandfield, Nancy H. Thomas

4.1 INTRODUCTION

Much of Mars research is driven by the search for past habitable environments. Research has moved beyond simply "follow the water" but now is also driven by "follow the energy", "follow the organics", and "follow the geochemical system". Environments prone to serpentinization are of interest because they imply the presence of several of the "key elements" for life as we know it: liquid water, metabolic energy source (H_2), and abiotic means of forming organics like CH_4 (through fischer-tropsch type reactions) (e.g., Kelley et al., 2001, 2005; Früh-Green et al., 2004; Russell et al., 2010**)**. These reactions are also often discussed and considered relevant for origin-of-life hypotheses for life on Earth (Russell et al., 2010, 2014; Stüeken et al., 2013; Sojo et al., 2016).

Low- temperature serpentinization reactions on Earth produce a specific **suite** of minerals providing evidence for the reactions occurrences. These reactions result in the presence of serpentine, carbonate, talc, saponite, and amphibole (e.g., Frost and Beard, 2007). Additionally, this suite of minerals can be detected from orbit if they are exposed at the surface due to diagnostic absorptions in the near- and thermal-infrared wavelength regions (**Figure 4.1**; e.g., Amador et al., in revision (Chapter 3)). Serpentine has been identified in several locations across Mars and much work has gone into specifically describing its occurrence, particularly in Nili Fossae (Ehlmann et al., 2009, 2010; Brown et al., 2010; Viviano et al., 2013; Amador et al., in revision (Chapter 3)).

The observed serpentine within olivine-rich basaltic exposures in Nili Fossae are associated with both Mg-carbonate and talc/saponite phases that likely indicate a sustained low-temperature serpentinizing system, making it a compelling site for detailed study by future landed missions to search for potential biosignatures.

We would like to understand if sites like Nili Fossae are common on Mars and if there are other sites on the planet that once similarly contained these types of habitable environments that could be studied in detail. Because serpentinization reactions are favored in environments that are enriched in olivine, we might expect to find additional evidence for serpentinization in other regions that are enriched in olivine on Mars, like Nili Fossae.

Initial surveys across Mars have indicated limited exposures of serpentine (Ehlmann et al., 2010), we hypothesize that its paucity may be due to several factors: First, the minor 2.12 µm spectral absorption (**Figure 4.1**) that is unique to serpentine can be difficult to detect, potentially obscuring our ability to detect its presence with the available remote sensing data. Additionally, any serpentine that may be exposed on the surface may be occurring in low concentrations or small exposures, again precluding our ability to detect the serpentine from orbit. Lastly, the paucity of observed serpentine may simply be because serpentinization may not have been common on Mars.

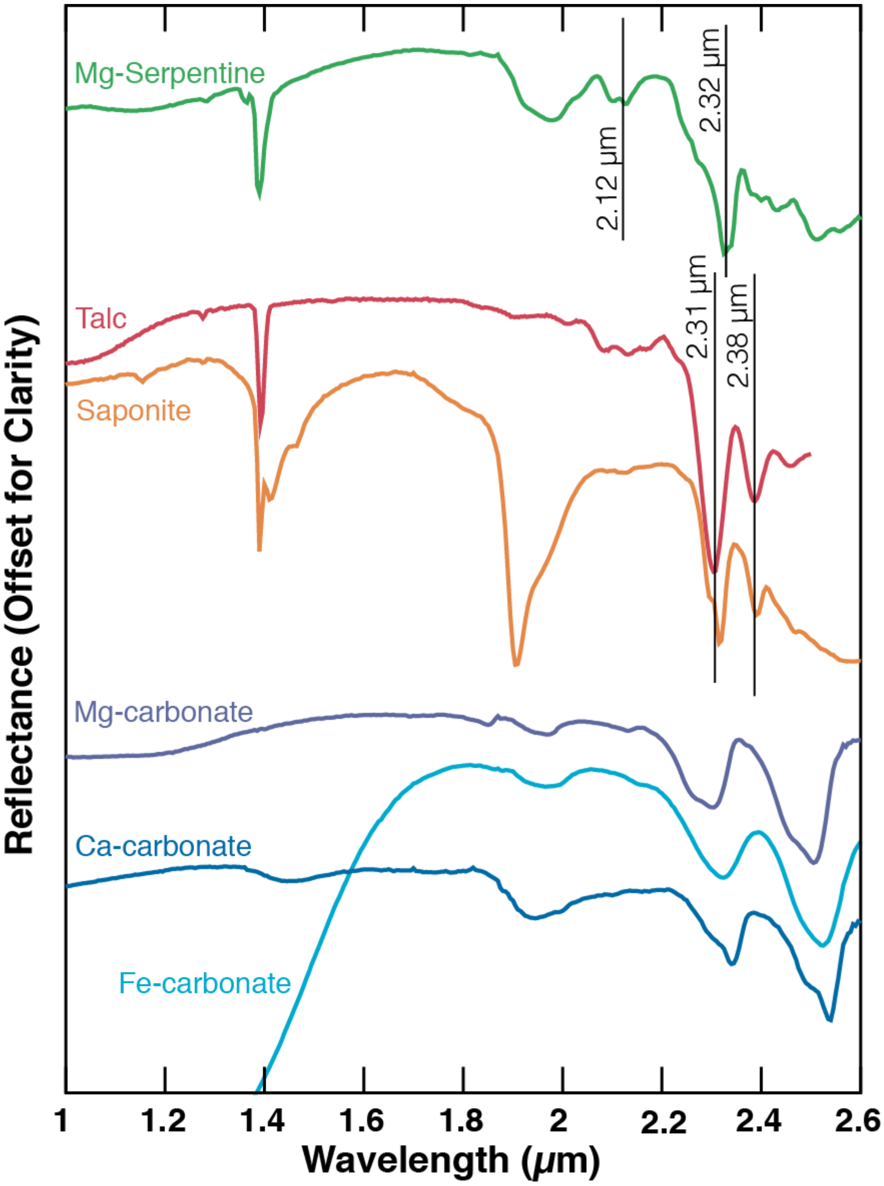

Figure 4.1. Near-infrared reflectance library spectra for minerals associated with serpentinization reactions. See **Supplementary Table 5.20** for references.

To gain a comprehensive understanding of the exposures of serpentine across the planet, especially in the context of past habitable environments suitable for future exploration, we conducted a survey of all Compact Reconnaissance Imaging Spectrometer for Mars (CRISM) data products between 70 °N and 70°S in search for spectral evidence for serpentine. We targeted all hyperspectral CRISM image products in regions with elevated abundances of olivine; additionally, we surveyed a representative sample of the remaining global full-resolution targeted data products outside those targeted regions. To look through thousands of images in a timely manner, we used semi-automated factor analysis and target transformation techniques (Bandfield et al., 2000; Thomas and Bandfield, 2013; Thomas and Bandfield, 2016, in revision) to rapidly and quantitatively determine which CRISM images were likely to contain serpentine, Mg-carbonate, and talc/saponite as dominant spectral contributors. These techniques are particularly helpful when searching for phases, such as serpentine, that have subtle spectral absorptions or are widely distributed at low concentrations.

This study provides a more complete understanding of the spatial distribution of serpentine across the globe and places this distribution into the geologic context in which we observe the phases. This constrains the sites on Mars with the highest potential for once containing habitable environments accessible to future landed missions with relevance to astrobiology. This study also serves as an example application to provide a more thorough understanding of the strengths and weaknesses of using factor analysis and target transformation for informing global spectroscopic studies.

4.2 BACKGROUND

4.2.1 Serpentinization and its Astrobiological Implications

Serpentinization is a geochemical process in which olivine is hydrated to form serpentine, magnetite, and brucite. The oxidation of Fe^{2+} in fayalite (Fe-endmember of olivine solid-solution series) leads to the production of H_2 and can be metabolically exploited by microbial life. Additionally, H_2 is a strong electron donor that can drive the synthesis of organic molecules in Fischer-Tropsch-type reactions (e.g., Holm and Charlou, 2001; McCollom and Seewald, 2007). Serpentinization is common on Earth in locations where olivine-enriched bedrock is in contact with liquid water, typically in tectonically active margins such as at slow-spreading centers (e.g., Lost City Hydrothermal Field, off-axis to the Mid-Atlantic Ridge; Kelley et al., 2001) and obducted ocean-floor sequences (e.g., the Asbestos Ophiolite Complex; Greenberger et al., 2015).

Dense microbial communities have been shown to live in zones of active serpentinization, surviving on the products of these reactions, in the absence of other energetic inputs like solar or volcanic. As an example, H_2 can be directly used as an electron donor in the metabolism of many chemoautotrophic organisms, like the methanogens at the Lost City Hydrothermal Field that use H_2 to fix CO_2 and produce CH_4 and H_2O (Kelley et al., 2001; 2005). Furthermore, the chemistry and mineralogy that exists in these settings suggest potential links to prebiotic chemistry (Cody, 2004; Stüeken et al., 2013) and are often discussed as compelling environments for key steps in the origin of life on Earth (e.g., Russell et al., 2010; 2014; Stüeken et al., 2013; Sojo et al., 2016).

Because serpentine forms in this setting and typically results in the release of bio-accessible H_2, it is considered a unique environmental indicator mineral. In this sense, the identification of serpentine, particularity when found *in-situ*, indicates that serpentinization occurred and that H_2, as well as short-chained organics, were likely released.

4.2.2 Identifying serpentine from remote sensing datasets

In addition to being an indicator mineral for a specific environment, serpentine can also be uniquely identified using readily available remote sensing data, such as CRISM on the Mars Reconnaissance Orbiter (MRO). Near-infrared (defined here as 1.0-3.0 µm) reflectance spectra of serpentine contains a set of five absorptions (**Figure 4.1**). Absorptions near 1.4 and 1.9 µm are due to structurally-bound or adsorbed OH^- and H_2O and are common in hydrated phases (e.g., phyllosilicates). Several longer wavelength absorptions are more diagnostic of serpentine: a unique 2.10-2.12 µm absorption associated with a sharp, asymmetric 2.35 µm Mg-OH combination band, and a 2.52 µm symmetric absorption. The presence of the relatively shallow 2.12 µm absorption is necessary to confidently identify the presence of serpentine in reflectance spectra, as the other absorptions can be found in other hydrated silicate and carbonate phases, for example.

4.2.3 Serpentine on Mars

Ehlmann et al. (2009) first described the occurrence of serpentine on Mars in the Nili Fossae region using near-infrared reflectance spectra of the surface collected by CRISM. A subsequent study described the global occurrences of serpentine (Ehlmann et al., 2010) with the data available at the time. Ehlmann et al. (2010) found that the serpentine observations could be broken down into three geologic settings: 1) mélange terrain, 2) southern highland craters, 3) Noachian bedrock in stratigraphic section, but in general, identifications of serpentine were still quite rare across the globe.

Serpentine exposures outside of Nili Fossae have been identified in several locations across the martian southern highlands. These locations include Mawrth Valles, Claritas Rise, near Baetis Chaos (Ehlmann et al., 2010), and along the Thaumasia Highlands (Viviano-Beck et al., 2017). Ehlmann et al. (2010) also report additional “probable” serpentine detections across the southern highlands, but given the subtle nature of the diagnostic 2.12 µm reflectance absorption, it is not clear how reliable these probable detections may be. Most of these detections (apart from detections made within stratigraphic section) likely represent serpentine that did not form *in-situ* because they are typically associated with impact ejecta (e.g., Chia Crater; Ehlmann et al., 2010) or in knobby terrain with a diverse range of associated minerals that are inconsistent with any one specific formation environment (e.g., Claritas Rise; Ehlmann et al., 2010). In other words, these phases have now been exposed but likely formed elsewhere, either below the surface or more distally and subsequently transported and buried. The identification of these occurrences is interesting in that they help confirm the idea that serpentinization is a favorable process on a basaltic planet – with likely increasing concentration of olivine at depth. However, given that they are not found in-place, the lack of geologic context makes it difficult to further our understanding of habitable environments on Mars.

In contrast, the identification of serpentine within a well-defined stratigraphic section is particularly interesting because it likely implies that the observed serpentine formed *in-situ*, making that site a compelling place to search for biosignatures or biomarkers. For example, the serpentine-bearing rocks in Nili Fossae are found within a well-defined olivine-rich basaltic unit with variable concentrations of Mg-carbonate, and talc and/or saponite (e.g., Amador et al., in revision (Chapter 3)).

This olivine-rich unit is of particular interest for serpentinization as both the spectral signatures and the mineralogy observed are consistent with Earth-based sampled from low-temperature serpentinization environments (Amador et al., 2016, in revision (Chapter 3)). It is the observation of this mineralogical suite that makes this site most compelling for *in-situ* low-temperature serpentinization and its implications for habitability. Rather than the observation of a single mineral (e.g., serpentine) that might be a “smoking gun” for a geochemical environment, the observation of this specific mineralogical suite provides greater constraints on the environment and confidence indeed once present.

4.3 DATA AND METHODS

4.3.1 Approach

To gain a more comprehensive understanding for the distribution of serpentine, and the serpentinization mineral suite (serpentine, carbonate, talc/saponite), on Mars and whether they are related to olivine-enriched regions, it was necessary to survey a globally representative number of images. As of July 2016, there were 13,460 Full Resolution Targeted (FRT), Full Resolution Short (FRS), Half Resolution Long (HRL), and Half Resolution Short (HRS) CRISM images between 70°N and 70°S available at NASA's Planetary Data System (PDS) archive. Traditional CRISM data analysis techniques involve visual inspection of band depth parameter maps that highlight spectral absorptions and slopes that are indicative of phases of interest and manual analysis of I/F (equivalent to reflectance) ratioed spectra. This is a time-consuming process that can take minutes to hours of analysis time for a given image. To systematically examine a representative number of CRISM images, in a timely manner, factor analysis and target transformation techniques were employed to quantitatively describe each image (Section 4.3.3*;* Thomas and Bandfield, 2014, Thomas and Bandfield, 2016, in revision). The CRISM dataset was first separated into seven regions (**Table 4.4**). Five of these include olivine-rich regions: Northern Argyre, Nili Fossae, Terra Sirenum, Tyrhenna Terra/Southern Isidis, and Valles Marineris (e.g., Ody et al., 2013). Claritas Rise was chosen as the sixth regional dataset as this is where Ehlmann et al. (2010) found the best spectral example for serpentine to date, the seventh region represents all the remaining CRISM images bounded by 70°N and 70°S and exclusive of these six regions.

Table 4.4. Regions of Interest

Region	Latitude Range (°N)	Longitude Range (°E)	Number of Images	Images Analyzed
Northern Argyre	-20 to -48	300 to 336	463	463
Claritas Rise	-25 to -42	246 to 264	122	122
Nili Fossae	30 to 15	72 to 80	229	229
Terra Sirenum	-20 to -40	150 to 207	558	558
Tyrhenna Terra/ S. Isidis	8 to -35	50 to 107	1,306	1,306
Valles Marineris	1 to -14	256 to 320	1,092	1,092
Remaining	70 to -70	0 to 360	9,690	6,854

Each image was run through an automated program that calculated the first 15 eigenvectors and corresponding eigenvalues for the image (See Section 4.3.3 for details). These eigenvectors describe the independently varying spectral components of the image and therefore can be used as a test for the presence of certain phases of interest within the scene. For this study, we tested for a set of 12 spectral endmembers from laboratory measurements (Section 4.3.3). Using this test, CRISM images that showed evidence for the presence of carbonate, serpentine, and/or talc/saponite were flagged and subsequently analyzed in detail for the presence or absence of these phases. This approach allowed us to examine thousands of CRISM images and interpret the mineralogical information in a timely manner with a high degree of confidence.

4.3.2 Compact Reconnaissance Imaging Spectrometer for Mars (CRISM)

CRISM is a hyperspectral visible- and near-infrared imager on the Mars Reconnaissance Orbiter with 544 spectral bands between ~0.4 and 4.0 µm (Murchie et al., 2007). CRISM has multiple observation modes with several spectral and spatial samplings. For this work, we used full-resolution short and targeted (FRS and FRT) images with a spatial sampling of ~20 m/pixel and half-resolution short and long (HRS and HRL) images with a spatial sampling of ~40 m/pixel. CRISM mapping products (MSP; 200 m/pixel sampling with 70 bands between 0.4-4 µm) exist with near global coverage, however, these data lack the spatial and spectral sampling necessary to make the measurements we are interested in. For example, these data products would not be able to spectrally resolve the diagnostic 2.12 µm serpentine absorption with a high enough fidelity to confidently identify its presence. In addition, the spatial sampling of the MSP data products may not be sufficient to identify small-scale exposures.

CRISM images were first corrected for atmospheric gas absorptions using the scaled volcano-scan method (McGuire et al., 2009) with additional atmospheric correction techniques adapted from the current CRISM Analysis Tool (Version 7.2.1). Spectral index maps were created in a manner like that described by Pelkey et al. (2007) and Viviano-Beck et al. (2014). Spectral indices map the strength of specific spectral features that are indicative of phases across a CRISM image. For example, the D2300 index maps the depth of the ~2.3 µm Fe/Mg-OH combination band indicative of Fe/Mg-phyllosilicates. Areas of interest within a given image were then further investigated by evaluating I/F spectra (I/F is the radiance observed by the CRISM detector divided by the solar irradiance at the top of the martian atmosphere and is equivalent to reflectance) and spectral ratios to confirm the presence or absence of the spectral feature(s) of interest. Spectral ratios were created by taking a pixel average of I/F values for an area of interest and dividing it by the I/F average for a region considered spectrally neutral (or spectrally known) within the same image columns, to reduce the effects of systematic column correlated noise on the spectral ratios, as well as to accentuate weak spectral absorptions.

4.3.3 Factor Analysis

Factor analysis and target transformation (Malinowski, 1991) enable the search for independently varying spectral components, and to test for the presence of individual endmembers, within a mixed spectral dataset. These methods have previously been applied to laboratory and near- and thermal-infrared spacecraft spectral data (Bandfield et al., 2000; Christensen et al., 2000; Bandfield et al., 2002; Hamilton and Ruff, 2012; Glotch and Bandfield, 2006; Glotch and Rogers, 2013; Geminale et al., 2015; Thomas and Bandfield, 2014; Thomas and Bandfield, in revision*)*, and here we apply these methods at a global scale.

Factor analysis derives a set of orthogonal eigenvectors and associated eigenvalues from a set of measured spectra. The number of significant eigenvectors can be used to estimate the number of independent components present within the mixed system. Additionally, the significant eigenvectors can be used to reconstruct spectral endmembers, even if those endmembers do not exist in the original data in a pure, unmixed state. Therefore, the eigenvectors can be used to test for the presence of independent spectral components, like serpentine or carbonate, that may be present in the system. This test is done by using target transformation, a least squares fit of the significant eigenvectors to a laboratory spectral endmember. If the endmember can be closely matched, then it is likely a component of the system. In cases where the match is good, but not perfect, the resulting fit spectrum typically represents a more accurate endmember than the test spectrum and can be used to identify spectral variations, like those due to cation content (e.g., Mg-, Fe-, or Ca-carbonates) (Bandfield, 2000). This technique allows for the identification of specific endmembers from an image without having to first identify regions containing high and low concentrations of the endmember of interest. Because it is sensitive to the independently variable component anywhere within an image, no spectral ratioing is required to identify the endmember.

For the CRISM dataset, we follow methods like those developed by Thomas and Bandfield, 2014, (Thomas and Bandfield, in revision) and calculate the significant eigenvectors from a range of 133 spectral bands between 1.7 and 2.6 µm (CRISM bands 197 through 330) where spectral features of interest are located. This spectral range includes features due to structurally-bound or adsorbed H_2O, phyllosilicates, smectites, and carbonate phases. Eigenvectors and eigenvalues are calculated from CRISM images after removal of atmospheric gas absorptions. The images are cropped to remove null edge values, as well as right-edge pixels that typically contain significant noise that can interfere with calculations (**Table 4.5**). To reduce processing time, the eigenvectors are calculated from every 5th pixel of every 5th line of a given CRISM image, which is sufficient to reconstruct the weak spectral absorptions associated with serpentine and still capture the dominant spectral components of the image.

Table 4.5. Imagine line/sample/bands used for factor analysis

CRISM Data Product	Column Samples Use	Row Samples Used	Spectral Bands Used
Full-Resolution Short (FRS)	10:592	2:179	197:330
Full-Resolution Targeted (FRT)	10:592	2:389	197:330
Half-Resolution Short (HRS)	7:283	2:224	197:330
Half-Resolution Long (HRL)	7:283	2:419	197:330

Lastly, the eigenvectors were used to test the image for potential spectral endmembers using target transformation. If the reconstructed spectrum produced a good fit to the laboratory endmemeber spectrum, this indicated a high likelihood that the endmember spectrum was an independent spectral constituent of the image. It is possible to calculate the root mean square difference between the reconstructed spectra and the spectral endmember and use this to quantitatively identify matches by goodness-of-fit (Malinowski, 1991), however, we found that the RMS value and therefore the quantitative measure of goodness-of-fit, can be confounded by noisy data, especially around 2.0 µm where residual atmospheric CO_2 features are common in the data, even when the spectra fit well at the particular wavelengths that would indicate the presence of the endmember phase. Therefore, for this study we relied on the visual inspection of the target transformation fits for each CRISM image processed. Compared to traditional CRISM data analysis techniques, this still reduced analysis time to several seconds per image compared to the minutes to hours that were previously required. Future work will aim to understand how to place more stringent, quantitative measures for goodness-of-fit to eliminate by-hand and visual inspection of the target transformation fits and fully automate this process.

The inspection of target transformation fits for all the CRISM images were then used to create a database of images with excellent fits for the mineral suite of interest: serpentine, magnesite, and talc/saponite, in addition to nine other phases that were documented for completeness (calcite, siderite, hydrated silica, gypsum, rozenite, kieserite, kaolinite, nontronite, and illite). Excellent fits indicated that the endmember phases of interest were a spectrally dominant constituent of the given image cube. However, this target transformation fit does not indicate where in the image the phases occur and subsequent parameter map and spectral ratios were necessary to identify outcrops containing phases of interest. This can be particularly tricky in the case of serpentine as the unique and diagnostic absorption at 2.12 µm has a relatively shallow spectral contrast compared to the other dominant absorptions at 1.9, 2.3, and 2.5 µm (**Figure 4.1**). Several attempts at producing a serpentine 2.12 band depth index have been unsuccessful at identifying pixels where known serpentine spectral characteristics exist such as in CRISM image FRS0002AE17_01 (Amador et al., in revision (Chapter 3)) in Nili Fossae. We attribute this inability to map pixels containing serpentine to several factors: 1) the weak spectral contrast of this absorption relative to the typical noise level within a given CRISM image and 2) the fact that this absorption is just long of any absorption due to residual atmospheric CO_2 at 2.0 µm. Because of this, as a first order confidence check that our method was indeed sensitive to serpentine, we confirmed our independent serpentine detection with CRISM images where Ehlmann et al. (2010) reported serpentine.

Additionally, to ensure that no obvious false-positive detections were made, and provide additional confidence in our method, all images that were flagged were first visually inspected to ensure that it was reasonable for the flagged phase to be present within the image. For example, an image that was flagged to contain serpentine, needed to have a clear exposure(s) highlighted by the D2300 index (indicative of a negative spectral slope, or drop-off, at 2.3 µm consistent with Fe/Mg-phyllosilicates) as this would be a necessary absorption for the identification for serpentine.

4.4 RESULTS

In total, we processed and analyzed 10,624 CRISM images, including all data products within the six target regions and 6,854 images outside of these regions between 70°N and 70 °S latitude (**Table 4.1**). Although this only represents ~70% of all hyperspectral images available, these remaining images still provide a global sampling of CRISM images across the planet.

4.4.1 Target Transformation Fits

The modeled target transformation results for the three spectral types of interest (serpentine, Mg-carbonate, and talc/saponite) were visually inspected for goodness of it. Typically, this involved matching diagnostic and unique absorption features (e.g., the 2.12 µm absorption in serpentine; Figure 1), as well as matching appropriate band shapes. Band centers were also taken into consideration but with the awareness that if the fit was closely matched, but not perfect, the fit was likely to be a more accurate endmember than the tested spectrum, indicating slightly different composition (e.g., due to variations in cation content) than the library test spectra.

This section shows typical target transformation fits for the three spectral types of interest and examples of an independent confirmation for each spectral type (e.g., ratioed I/F and band-depth parameters maps). In general, target transformation fits of modeled spectra in the Nili Fossae region are stronger and cleaner than in most other regions. To illustrate the variation in the quality of the results, we have chosen representative spectra from both outside the Nili Fossae region (Sections 4.4.1.1-4.4.1.3) and within the Nili Fossae region (Section 4.4.1.4). Additionally, two other regional and local settings show unique target transformation fits and inferred mineralogy: Leighton Crater (within the Tyrhenna Terra/S. Isidis Region) and Mawrth Vallis ("Remaining" dataset) (Sections 4.4.1.5-4.4.1.6), those specific results are also reported in this section.

4.4.1.1 Serpentine

CRISM images with clear target transformation fits for serpentine always show well-defined absorptions at 2.12 µm and well-defined asymmetric absorption at 2.32 µm or in some cases, just short of 2.32 µm (**Figure 4.2**). The best spectral match for serpentine in both ratioed I/F spectra (Ehlmann et al., 2010) and via target transformation using independent eigenvectors is CRISM image FRT0000634B_07 in Claritas Rise (**Figure 4.2**a). In this case, the target transformation fit matches both the shape and wavelength center of the 2.32 µm absorption. In some cases, the modeled 2.32 µm absorption is shifted short-ward (**Figure 4.2**c), this likely indicates a more realistic spectral endmember for those images relative to the target input spectrum provided. As such, this shift to slightly shorter wavelengths may indicate variable alteration to another Fe/Mg-phyllosilicate mineral phase like talc or saponite.

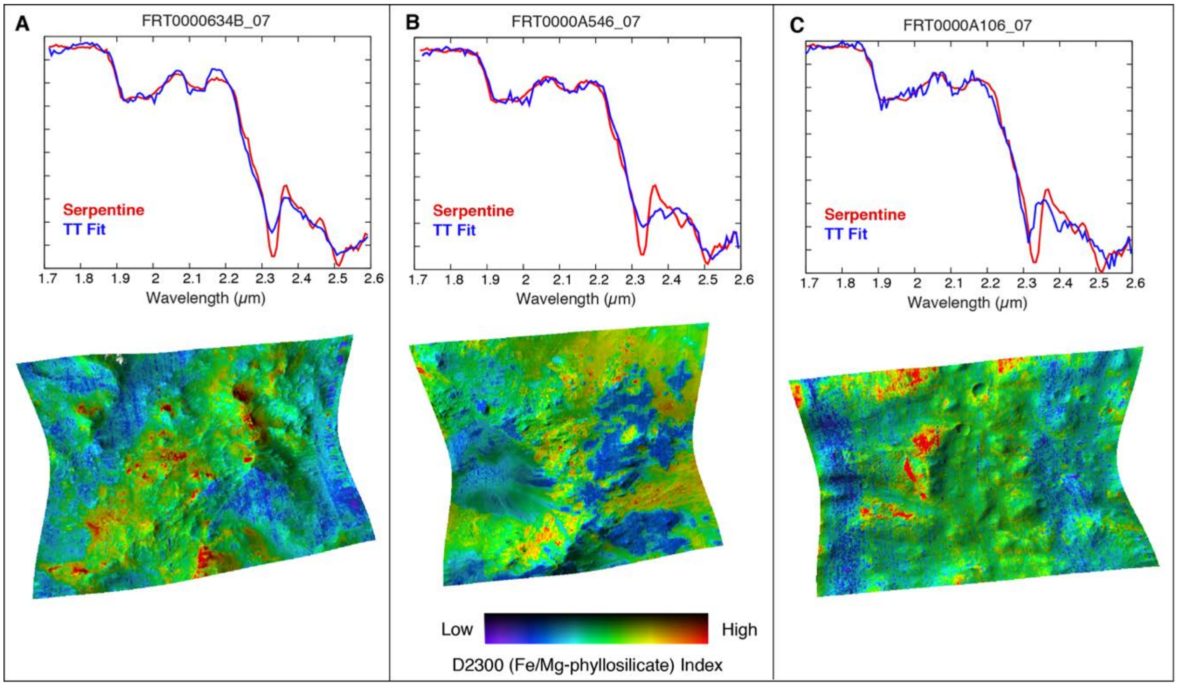

Figure 4.2. Three examples of excellent target transformation fits for serpentine. Panels A-C show examples of CRISM images where serpentine has previously been identified (Panel A; Ehlmann et al., 2010), where serpentine has been speculated (Panel B; Michalski and Niles, 2010), and a new image, outside of Nili Fossae, with a clear fit for serpentine (Panel C). CRISM image FRT0000634B_07 shows the best spectral match for serpentine in both ratioed I/F spectra (Ehlmann et al., 2010) and via target transformation using independent eigenvectors.

It was difficult to independently verify the presence of serpentine in CRISM images that show good target transformation fits for serpentine. Except for surfaces identified in previous studies by Ehlmann et al. (2009; 2010) and Amador et al. (in revision) (Chapter 3) in Nili Fossae, we were unable to independently identify the diagnostic 2.12 μm serpentine feature using ratioed I/F spectra in new flagged images. However, all images flagged showed clear surfaces with associated 2.3 μm absorptions as mapped by the D2300 index (**Figure 4.2**). This absorption is also necessary to uniquely identify serpentine (**Figure 4.1**). This is further discussed in Section 4.5.1.

4.4.1.2 Mg-Carbonate

Target transformation fits for Mg-carbonate show two absorptions at 2.3 and 2.5 µm (Figure 3, Panel A). Mg-carbonate (e.g., magnesite) can be distinguished from Ca/Fe-carbonates (e.g., calcite/siderite) using target transformation by the wavelength center and absorption shape (**Figure 4.1**) (Thomas and Bandfield, 2014; Thomas and Bandfield, in revision). Clear fits to Mg-carbonate consistently show the correct band center and absorption shape in the target transformation modeled spectra (e.g., **Figure 4.3**).

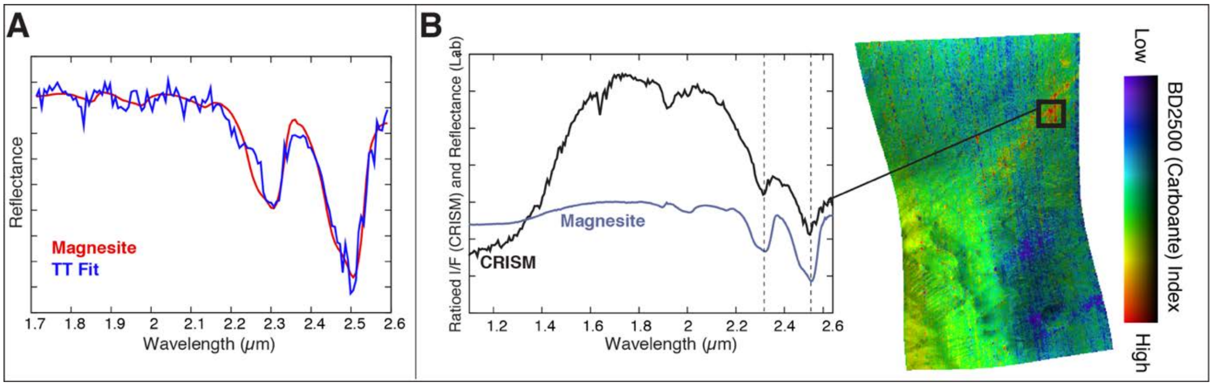

Figure 4.3. Target transformation fit for Mg-carbonate in CRISM image HRL000095C7_07 in Chia Crater. The presence of Mg-carbonate can be independently verified by viewing ratioed I/F spectra and by displaying the BD2500 (Mg-carbonate) index map.

Mg-carbonate can typically be independently confirmed using ratioed I/F spectra, as in CRISM image HRL000095C7, which covers a portion of the southern rim of Chia Crater, north of Juventea Chasma (Valles Marineras Region) (**Figure 4.3**). This example shows a good fit for magnesite in its target transformation modeled fit and can be verified by the 2.5 µm band-depth index map (consistent with Mg-carbonates) as well as by viewing the ratioed I/F CRISM spectra from the image (**Figure 4.3**b) that also show the proper spectral shape and band centers for Mg-carbonate.

4.4.1.3 Talc/Saponite

The third spectral phase we searched for in this study was talc/saponite. In the near-infrared wavelength region, talc and saponite appear spectrally similar and can be difficult to disambiguate (**Figure 4.1**). Both phases have narrow absorptions centered near 2.3 and 2.4 µm with variable spectral contrast in the 2.4 µm absorption (**Figure 4.1**). There is often an additional weak absorption near 2.46 µm present in laboratory spectra for talc, but given the noise level within a typical CRISM image and other interfering factors, this absorption is not expected to be identifiable in CRISM data. The target transformation fits shown in **Figure 4.4** are representative of the type of fits found for talc and saponite globally. Fit spectra are typically quite noisy, indicating the presence of these phases at low levels in the

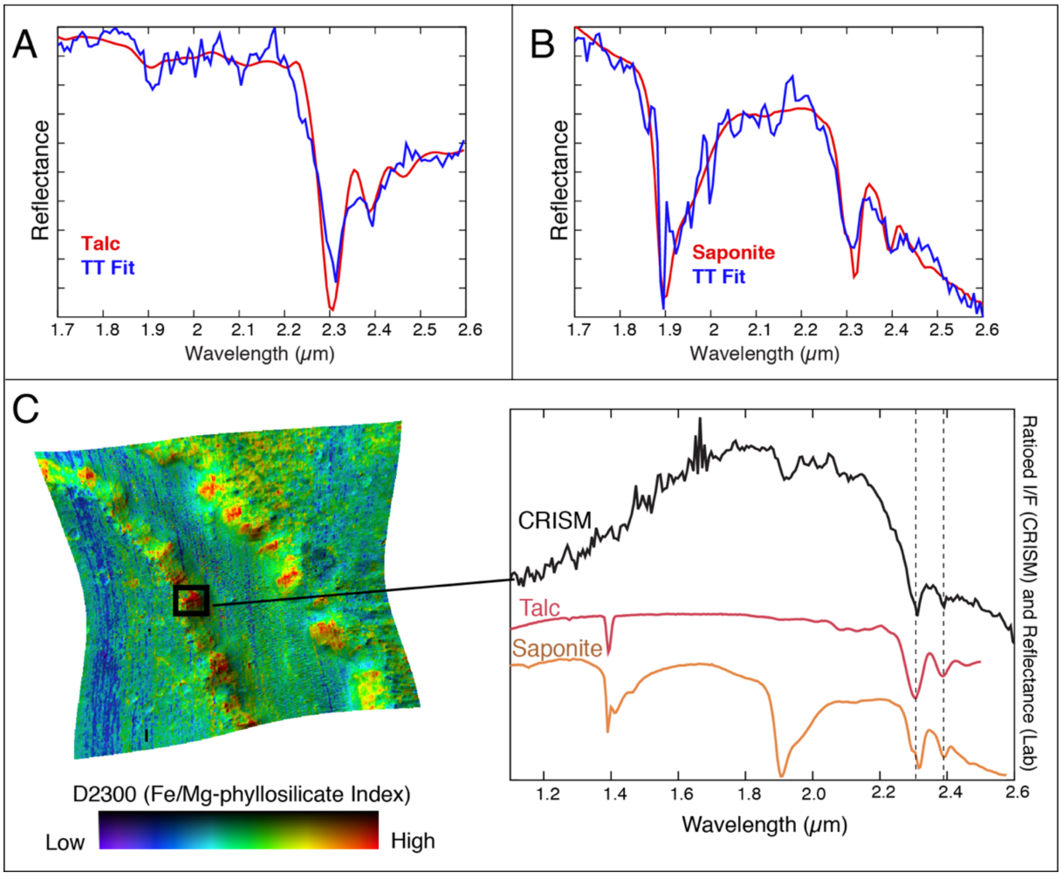

Figure 4.4. Target transformation fits for talc/saponite spectral type. Panels A and B show fits to talc and saponite, respectively, for one image in Her Desher Vallis. Fit can be independently verified using ratioed I/F spectra and D2300 colorized index map (Panel C).

data. We found that with target transformation results alone, it is difficult to determine whether the fits are more consistent with one phase over the other. Despite this, images flagged with positive fits always clearly show the necessary absorptions near 2.3 and 2.4 μm compared to images that were not flagged. Because of the spectral ambiguity between talc and saponite, this spectral type was simply labeled as “talc/saponite”.

CRISM image FRT00001756E_07, (**Figure 4.4**) in Her Desher Vallis (N. Argyre Basin Region) is an example of an image with good target transformation match for talc/saponite. The target transformation flag can be independently verified by both the D2300 band-depth index map as well as in the ratioed I/F spectra (**Figure 4.4**c) that show two well-defined absorptions near 2.3 and 2.4 μm. This image has previously been reported as containing a phyllosilicate spectral signature attributed to saponite (Buczkowski et al., 2010), again giving confidence in this technique’s ability to independently identify mineral phases of interest.

4.4.1.4 Nili Fossae (~76.695°E, 22.018°N)

The Nili Fossae region has the highest concentration of images with strong target transformation modeled fits for serpentine and Mg-carbonate, as well as five images that contain strong fits for a talc/saponite spectral type. Previously, three images were known in Nili Fossae to show spectral evidence for serpentine (Ehlmann et al., 2009; 2010; Amador et al., in revision (Chapter 3)). With this study, there are now a total of 16 images that show evidence for serpentine. This region has been extensively studied, and this study now provides additional and independent evidence for the presence of the spectral types of interest in the area. CRISM image FRT000028BA_07 is one of two images in Nili Fossae where all three spectral types are found within a single CRISM scene. These phases have previously been detected in this region using spectral ratios and band indices (e.g., Ehlmann et al., 2009; 2010; Brown et al., 2010; Viviano et al., 2013; Amador et al., 2016, in revision (Chapter 3)). Here we show an independent means of identifying this mineralogical suite using factor analysis and target transformation (**Figure 4.5**). Target transformation spectra fit the diagnostic 2.12 µm absorption well, follows the overall shape for the ~2.3 µm absorption, as well as the position and shape of the broad 2.5 µm absorption (**Figure 4.5**a).

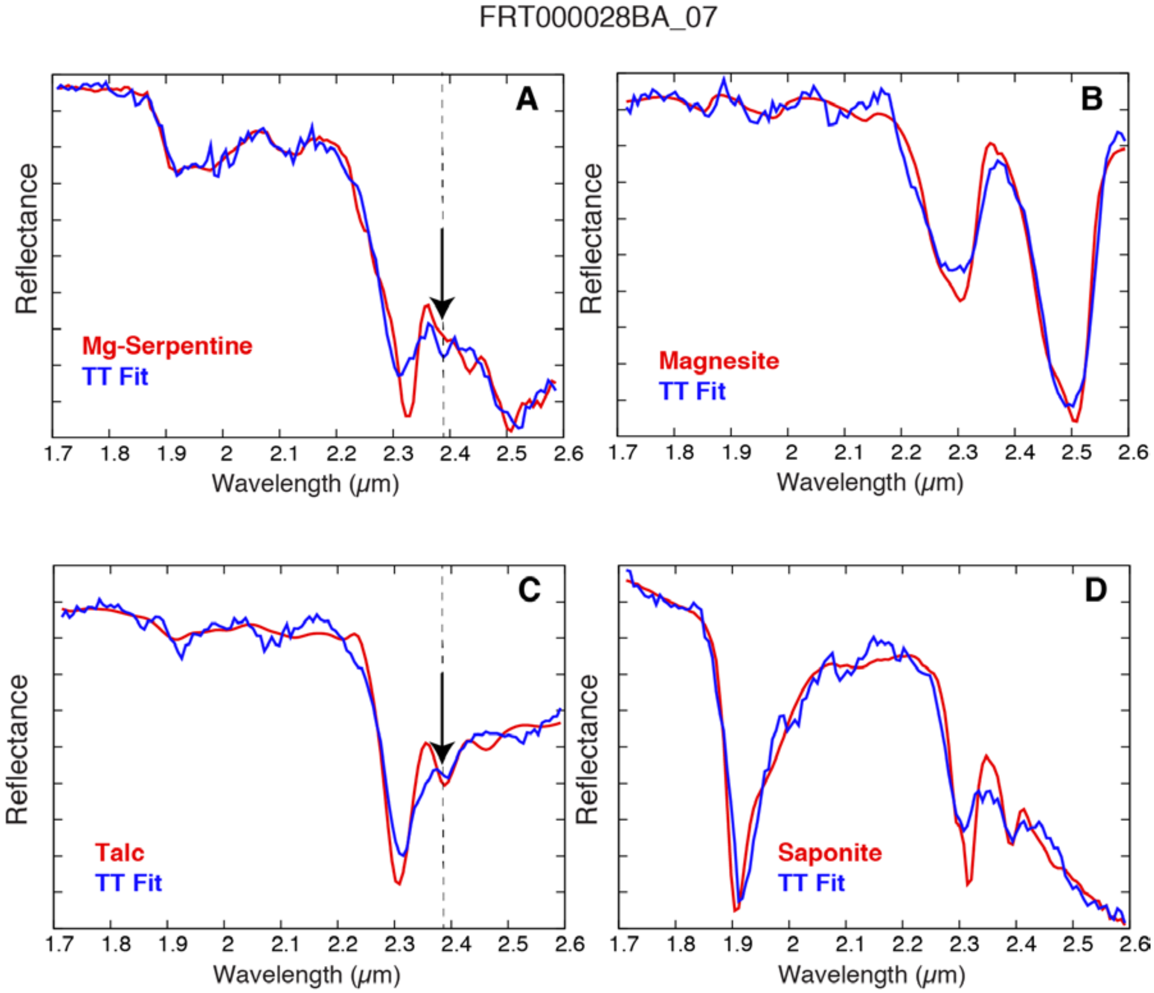

Figure 4.5. Representative target transformation fits for all spectral types in Nili Fossae from CRISM image FRT000028BA_07. Target transformation fits for serpentine exhibit diagnostic 2.12 µm absorption and an additional minor absorption near 2.4 µm, similar to talc and saponite, implying variable alteration of serpentine to a talc/saponite phase.

Notably, the 2.32 µm absorption is shifted slightly shorter than is typical of endmember serpentine measured in the lab and the modeled spectrum shows an additional minor absorption near 2.38 µm where both talc and saponite have a minor absorption (**Figure 4.5**a; **Figure 4.1**). In this case, the modeled target transformation spectrum is likely a more accurate spectral endmember than the test endmember shown. The modeled target transformation fit for magnesite is clear both in band center and shape. Lastly, the target transformation fits for both talc and saponite show that there is clearly a spectral phase present with an absorption near 2.3 and 2.4 µm, but this test does not provide confidence in distinguishing between one over the other. **Figure 4.5** is representative of the types of positive fits for the spectral types of interest within Nili Fossae.

4.4.1.5 Leighton Crater (57.752°E, 3.08°N)

Target transformation fits for images in Leighton Crater, a ~60 km diameter impact crater on the southwestern flank of Syrtis Major, were clear and matched well with a range of mineral phases including magnesite, siderite, serpentine, talc/saponite, and montmorillonite (Al-smectite) (**Figure 4.6**). Target transformation fits for CRISM image FRT0000A546_07, for example, are most consistent with a Ca/Fe-carbonate, such as siderite (**Figure 4.6**ab) and fits for serpentine show an additional absorption near 2.4 µm likely indicating that serpentine is found mixed with a talc/saponite phase (**Figure 4.6**c). Target transformation fits for a talc/saponite spectral type are most consistent with saponite in this image (**Figure 4.6**de) and target transformation results also point to an Al-phyllosilicate endmember, most consistent with montmorillonite (**Figure 4.6**f).

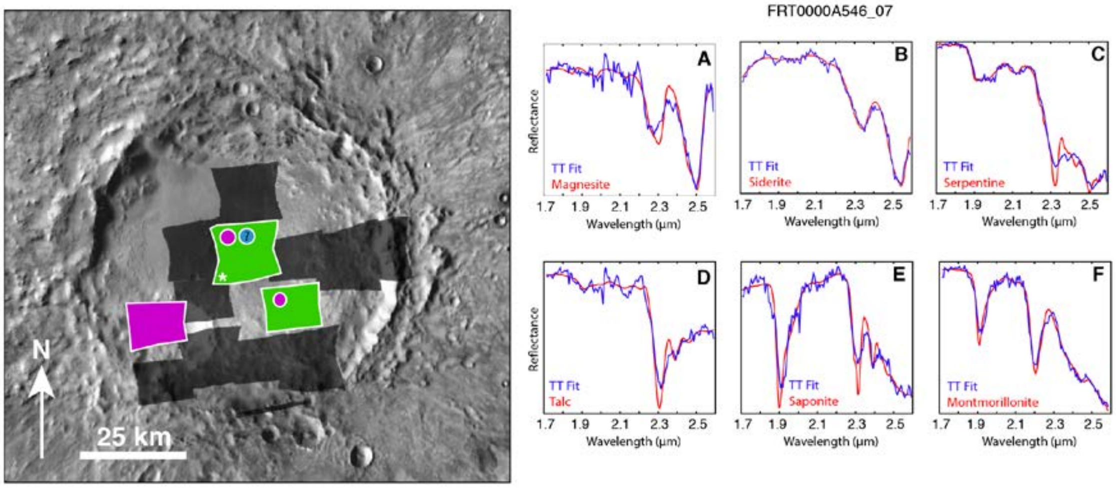

Figure 4.6. CTX mosaic of Leighton Crater with outlines of all overlapping CRISM images. Green stamps indicate images with fits for serpentine, magenta stamp and magenta circles, indicate images with fits for Mg-carbonate, gray stamps indicate images with no fits for investigated phases. Spectra come from CRISM image FRT0000A546_07 (starred). Fits are strong for all investigated phases and an Al-phyllosilicate phase consistent with montmorillonite.

4.4.1.6 Mawrth Vallis (~ 343.027°E, 22.43°N)

Target transformation fits for CRISM images found in the Mawrth Vallis region similarly showed a range of interesting mineral phases. Four images showed clear fits for serpentine in the region, three of which are within the main Mawrth Vallis plateau where high concentrations of phyllosilicates have been identified previously (e.g., Bishop et al., 2008; Poulet et al., 2014). As with previously discussed target transformation fits for serpentine, those matched in Mawrth Vallis show the diagnostic 2.12 µm absorption and an ~2.30 µm absorption shifted to slightly shorter wavelength centers compared to library endmember spectra for serpentine (**Figure 4.1**; **Figure 4.7**a). Mg-carbonates are detected in 12 CRISM images throughout the Mawrth Vallis region (**Figure 4.7**b), including a confirmation of Mg-carbonate previously reported in nearby McLaughlin Crater (Michalski et al., 2013). One CRISM image (HRS0000307A_07) shows evidence for talc, and a poor target transformation fit for saponite (**Figure 4.7**cd). In this case, the talc/saponite spectral type is more consistent with a talc spectral endmember. Target transformation modeled fits also showed abundant evidence for a Fe/Mg-phyllosilicate phase consistent with nontronite (**Figure 4.7**e), as well as several fits consistent with an Al-phyllosilicate like montmorillonite (**Figure 4.7**f).

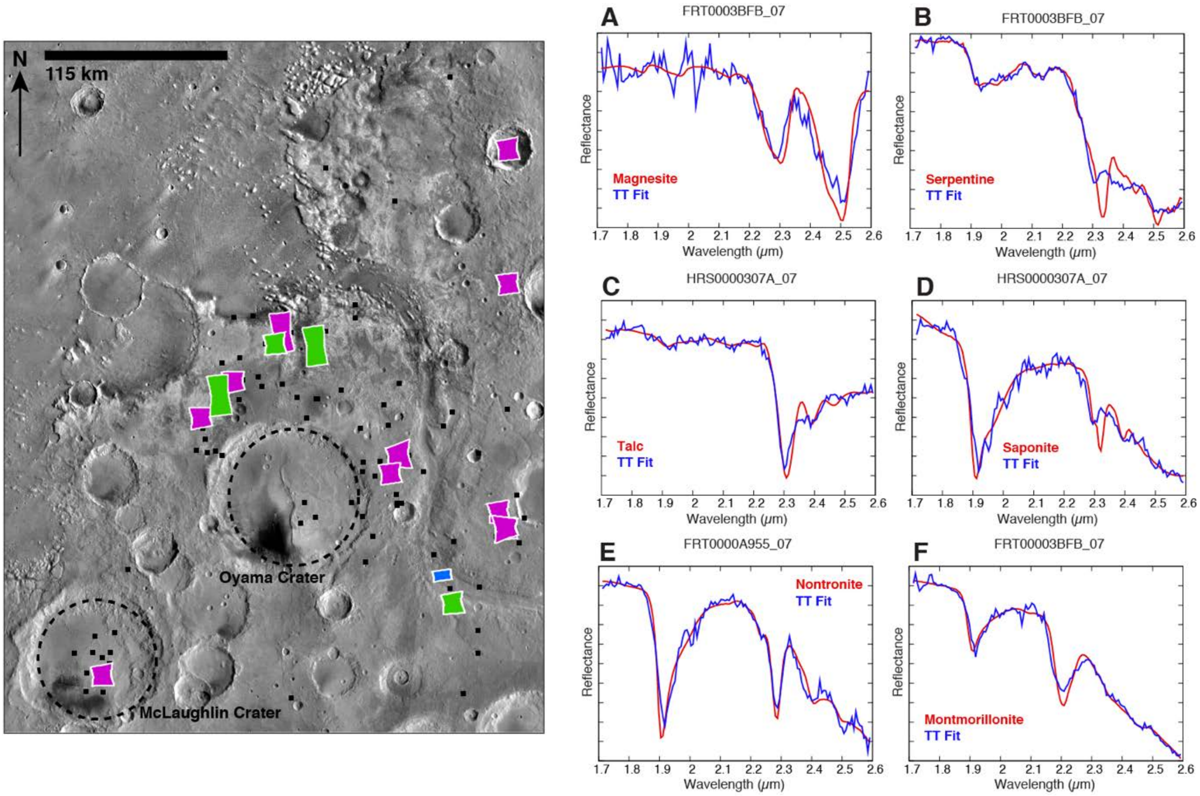

Figure 4.7. Viking MDIM 2.1 mosaic of the Mawrth Vallis region with all overlapping CRISM images. Small black squares indicate CRISM images with no fits for investigated phases. Green stamps indicate images with fits for serpentine, magenta stamps indicate fits for Mg-carbonate, and blue stamp indicates fit for talc/saponite. Representative target transformation fits shown to the right. Mg-carbonate and serpentine fits are clear, talc/saponite fits appear more consistent with talc. Additionally, target transformation techniques clearly identify a Fe/Mg-phyllosilicate phase consistent with nontronite and an Al-phyllosilicate phase consistent with montmorillonite.

4.4.2 Global Distributions

Globally, fifty-one CRISM images were identified with good fits to serpentine. All the CRISM images flagged also contained Fe/Mg-phyllosilicate-bearing surfaces as highlighted by the D2300 index (e.g., **Figure 4.2**). Additionally, none of the CRISM images flagged occur in unlikely geologic settings where these general phases have not been previously identified (**Figure 4.8**). Serpentine occurrences are distributed across the southern highlands and are concentrated in Nili Fossae, Mawrth Vallis, along the Thaumasia Highlands, and south-west of Meridiani Planun. In addition, several occurrences are present around Hellas Basin and Tyrhenna Terra (**Figure 4.8**). We consistently find serpentine where Ehlmann et al. (2010) show confident detections, and corroborate one out of their six “probable” detections from that study (**Figure 4.8**). Similarly, we also find serpentine in five of the seven locations that Viviano-Beck et al. (2017) identified near Claritas Rise, Valles Marineris, and the Thaumasia Highlands (**Figure 4.8**).

CRISM images identified with good fits for serpentine often show additional mineralogical diversity; nearly half of those images flagged also showed spectral evidence for Mg-carbonate or Ca/Fe-carbonate phases (**Table 4.6**). All images flagged (except HRL00006C8A_07 located in the Thaumasia Highlands) either have olivine-enriched surfaces within the image scene or have phyllosilicate-bearing surfaces with a ferrous component to its spectral signature (e.g., McKeown et al., 2009), as indicated by a steep positive slope between 1.0 and ~1.8 µm. This ferrous component could be due to olivine or ferrous chlorites or ferrous micas (McKeown et al., 2009). The geologic context for these exposures are quite diverse and range from layered exposures in crater rims and valley walls to layers within knobby eroded terrain (**Table 4.6**).

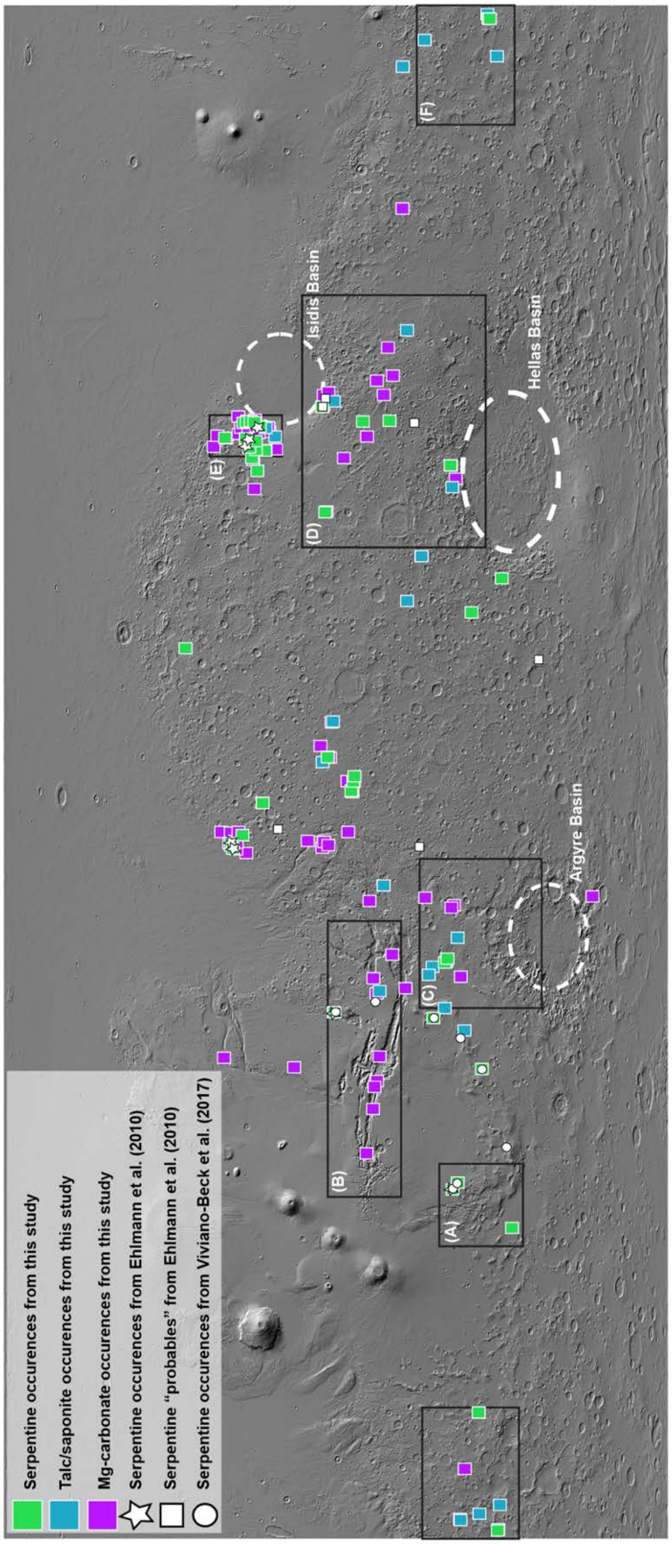
Serpentine occurences from this study
Talc/saponite occurences from this study
Mg-carbonate occurences from this study
Serpentine occurences from Ehlmann et al. (2010)
Serpentine "probables" from Ehlmann et al. (2010)
Serpentine occurences from Viviano-Beck et al. (2017)
Isidis Basin
Hellas Basin
Argyre Basin
(A)
(B)
(C)
(D)
(E)
(F)

Figure 4.8. Global distribution of target transformation fits for serpentine (green squares), Mg-carbonate (magenta squares), and talc/saponite (blue squares) over MOLA shaded relief map. Results from this study are shown with serpentine detections from previous studies (Ehlmann et al., 2010 and Viviano-Beck et al., 2017). Regions of interest are marked with black boxes. Region A: Claritas Rise, Region B: Valles Marineris, Region C: N. Argyre Basin, Region D: S. Tyrhenna Terra/S. Isids, Region E: Nili Fossae, and Region F: Terra Sirenum.

Table 4.6. Description of Images with Serpentine Detections

Region	CRISM Image ID	Associated Olivine?	Associated Secondary Minerals	Geologic Context
N. Argyre Basin	FRT00001756E_07	Ferrous component	Talc/Saponite	Layered outcrop on walls of Her Desher Vallis
N. Argyre Basin	HRL00009B61_07	Ferrous component	-	Layered outcrop on wall of Her Desher Vallis
Claritas Rise	FRT000040DB_07	Ferrous component	Siderite	Eroding/mobilized layered from crater rim
Claritas Rise	FRT0000634B_07	Ferrous component	Illite	Knobby terrain
Claritas Rise	FRS00032AF6_01	Ferrous component	-	Knobby terrain
Nili Fossae	FRT000028BA_07	Yes	Magnesite, talc, nontronite	Carbonate plains
Nili Fossae	FRT00003584_07	Yes	Magnesite, nontronite	Carbonate plains
Nili Fossae	FRT00003FB9_07	Yes	Magnesite, kaolinite (?)	Carbonate plains
Nili Fossae	FRT000064D9_07	Ferrous component	Carbonate (?), nontronite	Nili Fossae trough floor, near original proposed MSL proposed landing site ellipse
Nili Fossae	FRT00007BC8_07	Yes	Magnesite (?)	Nili Fossae trough floor, near original

				proposed MSL proposed landing site ellipse
Nili Fossae	FRT000088D0_07	Yes	-	Eastern wall of Nili Fossae main trough
Nili Fossae	FRT000095FE_07	Yes	Magnesite, hydrated silica	Carbonate plains
Nili Fossae	FRT00009971_07	Yes	-	Western rim of main trough
Nili Fossae	FRT0000A09C_07	Yes	Magnesite, talc (?)	Carbonate plains
Nili Fossae	FRT0000AA03_07	Yes	Magnesite	Carbonate plains
Nili Fossae	FRT0000ABCB_07	Yes	Magnesite, kaolinite	Layered outcrop
Nili Fossae	FRT0001B615_07	Ferrous component	-	Layered outcrop exposed on elevated terrain through Syrtis Major lava flow
Nili Fossae	HRL000040FF_07	Yes	Magnesite	Carbonate plains
Nili Fossae	HRL000095A2_07	Yes	-	Wall of main trough
Nili Fossae	HRL00009ABE_07	Yes	Kaolinite	Layered outcrop
Nili Fossae	HRL0000AB0A_07	Yes	Nontronite	Layered outcrop
Terra Sirenum	FRT00008C90_07	Ferrous component	Magnesite, hydrated silica, talc/saponite	Knobby terrain between Ariadnes Colles Collis and Kārūn Valles
Terra Sirenum	FRT0000A106_07	Ferrous component	Talc/saponite	Knobby terrain in Caralis Chaos
Terra Sirenum	HRL00007C95_07	Yes	-	Small-scale knobby plains with widespread phyllosilicate
Terra Sirenum	HRL0000D002_07	Ferrous component	Talc/saponite	Small-scale knobby plains with widespread phyllosilicate
Tyrhenna Terra/S. Isidis	FRT00008144_07	Yes	-	Exposed layer
Tyrhenna Terra/S. Isidis	FRT0000A33C_07	Yes	-	Exposed/eroded layer from crater rim
Tyrhenna Terra/S. Isidis	FRT0000A377_07	Yes	Carbonate (?)	Erosional unit coming from ridges south of Isidis Basin

Tyrhenna Terra/S. Isidis	FRT0000A546_07	Ferrous component	Siderite, kaolinite, Al-phyllosilicate	Central peak of Leighton Crater
Tyrhenna Terra/S. Isidis	HRS0000AA3A_07	Ferrous component	Magnesite (?)	Floor of Leighton Crater
Tyrhenna Terra/S. Isidis	HRL000067B5_07	?, ferrous component	Siderite	Central peak of crater near Oenotria Scopuli
Valles Marineris	HRL000095C7_07	Ferrous component	Magnesite	Floor of Chia Crater
Remaining: Mawrth Vallis	FRT00003BFB_07	?, ferrous component	Nontronite, kaolinite	Layered exposures south of Mawrth Vallis
Remaining: Nilo-Syrtis	FRT0000406B_07	Ferrous component	-	Syrtis Major lava flow, south-east of Antoniadi Crater
Remaining: Toro Crater	FRT00009786_07	Ferrous component	Magnesite, hydrated silica, talc/saponite (?)	Rim of Toro Crater on Syrtis Major
Remaining: SW Meridiani Planum	FRT0000979C_07	Yes	Magnesite (?)	Continuous exposure at southern Meridiani Planum edge
Remaining: SW Meridiani Planum	FRT0000A063_07	Yes	Magnesite	Exposures in elevated terrain near southern Meridiani Planum edge
Remaining: West of Mare Serpentis	FRT0000A22D_07	Ferrous component	-	Crater rim
Remaining: Mawrth Vallis	FRT0000A425_07	Ferrous component	Magnesite, nontronite, Al-phyllosilicate	Layered exposures within Mawrth Vallis MSL/Mars2020 proposed landing ellipse
Remaining: Rutherford Crater (East of Mawrth Vallis)	FRT0000A8CE_07	Ferrous component	Magnesite, nontronite, Al-phyllosilicate	Exposed terrain on outer rim of Rutherford Crater

Remaining: Mawrth Vallis	HRL000043EC_07	Ferrous component	Nontronite, Al-phyllosilicate	Layered exposures west of Mawrth Vallis MSL/Mars2020 proposed landing ellipse
Remaining: SW Meridiani Planum	HRL00005865_07	Yes	Magnesite (?)	Small-scale exposures around and near craters
Remaining: Thaumasia Highlands	HRL00006C8A_07	No	Siderite	Heterogeneous terrain, continuous exposures
Remaining: West of Hellas Basin	HRL0000814A_07	Yes	-	Crater floor, discontinuous exposures
Remaining: Mawrth Vallis	HRL00009A5F_07	?, ferrous component	Nontronite	Layered exposures within Mawrth Vallis MSL/Mars2020 proposed landing ellipse
Remaining: Nilo-Syrtis	HRS00002FC5_07	Yes	Magnesite, nontronite, Al-phyllosilicate	Discontinuous exposures, mobilized sediments, east of Negril Crater
Remaining: Nilo-Syrtis	HRS000030A2_07	Yes	Magnesite	Discontinuous exposures, mobilized sediments coming from elevated ridges, south of Negril Crater
Remaining: Thaumasia Planum	HRS0000A8D3_07	Ferrous component	Al-phyllosilicate (?)	Heterogeneous exposed layer

Of the images surveyed, 143 showed good fits for Mg-carbonate, 72 of which are located within the heavily CRISM targeted Nili Fossae region and have generally been reported by previous studies (e.g., Ehlmann et al., 2008; Ehlmann and Edwards, 2015; Thomas and Bandfield, 2014; Thomas and Bandfield, in revision, Amador et al., in revision (Chapter 3)). Other Mg-carbonate detections are concentrated near and on the walls of Valles Marineris, in the Mawrth Vallis region, within Aram Chaos, and in Tyrhenna Terra (**Figure 4.8**).

Lastly, there are 38 images with good fits for talc/saponite distributed across the southern highlands (**Figure 4.8**). Of the regions of focus for this study, Terra Sirenum has the largest fraction of images with excellent fits for talc/saponite (**Table 4.7**). Similarly, the walls of Her Desher Valles and Nirgal Vallis north of Argyre Basin also show talc/saponite spectral signatures.

Table 4.7. Detections for investigate spectral types

Region	Northern Argyre	Claritas Rise	Nili Fossae	Terra Sirenum	Tyrhenna Terra/ S. Isidis	Valles Marineris	Remaining Global
Total Images	463	122	229	558	1,306	1,092	6,854
Images with Serpentine	2	3	16	4	6	1	19
Images with Mg-Carbonate	3	0	72	3	13	9	43
Images with Talc/Saponite	6	0	5	10	4	2	12

4.5 DISCUSSION

4.5.1 Usefulness of Factor Analysis and Target Transformation in Searching for phases Associated with Serpentinization

The use of factor analysis and target transformation has been successful in globally mapping the CRISM images and locations with the highest probability of containing serpentine, Mg-carbonate, and talc/saponite spectral phases. This corroboration of previous detections using an alternative method provides additional confidence in the ability of target transformation to identify specific phases of interest.

Our positive fits for a talc/saponite phase and Mg-carbonate phases were more easily confirmed independently using traditional I/F spectral ratios and band-depth parameter maps. In contrast, in most cases it was not possible to independently identify serpentine-bearing surfaces in CRISM images even with clear target transformation fits to a serpentine library spectrum. One of the values of the factor analysis and target transformation method, is that if the significant eigenvectors can be reconstructed to fit a test library spectrum, then that endmember *is* a component of the system as a whole, in this case the entire CRISM scene, and that it is *possible* that this endmember exists in its pure form in the image (Bandfield et al., 2000). This method can also find components to the system even if the endmember only exists as a spectral mixture in the scene (Bandfield et al., 2000). Therefore, even though for our application we were unsuccessful in finding specific CRISM pixels that contained enough serpentine to be detectable in their reflectance spectra, it does not indicate that our technique was incorrect in predicting its presence. Rather, it likely indicates that serpentine exists at low enough concentrations across the entire CRISM scene to affect the independently varying eigenvectors of the scene. The target transformation uses the statistical variation present within all the data used to calculate the eigenvectors. If the phase of interest is present, but variable at a low concentration within a CRISM image, it may still be identified even though it may be undetectable in spectral ratios and index images. Additionally, the serpentine that is present is likely to be variably altered, evidenced by the slight variation in the reconstructed modeled target transformation fits for serpentine compared to the laboratory endmember spectrum (e.g., **Figure 4.2**bc; **Figure 4.5**a).

In addition to corroborating previous detections of serpentine, this study consistently predicts serpentine in regions where we would most expect it to occur from regional geologic context and past studies, for example in the carbonate plains in Nili Fossae (*S*ee Section 4.5.2.4 for more details). In this sense, this method has enabled the detection/prediction of surfaces containing serpentine that would otherwise be missed using traditional CRISM data analysis techniques. Given these confidence checks on our technique, for the remainder of this study we will refer to CRISM images with clear target transformation fits for phases of interest as *identifications* or *detections*, acknowledging that these are not direct detections and the discussed uncertainties of this method.

4.5.2 Global Distributions, Spatial Correlations between Phases, and Regions of Interest

In general, occurrences of serpentine, Mg-carbonate, and a talc/saponite spectral type are still quite rare across the planet (**Figure 4.8**). New identifications of serpentine, especially around Tyrhenna Terra, Terra Sirenum, and in Meridiani Planum, show no spatial correlation with other phases of interest that would indicate a common geologic or geochemical process. Similarly, the serpentine detections do not appear to be directly associated with ultramafic exposures or regions other than in Nili Fossae, although 9 of 35 CRISM images with serpentine detections outside of Nili Fossae show spectral evidence for olivine-enriched surfaces within the image scene.

The one spatial factor that all detections have in common is their association with relatively dust-free regions (**Figure 4.9**). The global surface (and atmospheric) dust on Mars obscures much of the surface from these types of spectroscopic analyses resulting in an observational bias to the compositional interpretations that can be made from orbit. The dusty regions often hinder our interpretation of the surface composition using orbital instrumentation. However, this is a commonality shared amongst most secondary alteration products observed to date (e.g., Carter et al., 2013).

The lack of spatial correlation between spectral types of interest does provide value to our understanding of how these phases formed and under what conditions. For example, the talc/saponite spectral type that was investigated because of its mineralogical and spectral context in Nili Fossae has been observed across the southern highlands. Given that it is rarely found in association with serpentine and Mg-carbonate outside of Nili Fossae, it is more likely that this spectral type is due to a saponite phase rather than a talc. Saponite can readily form from the low-temperature alteration of basalt whereas on Earth, talc is most commonly found in association low-grade metamorphosed ultramafic rocks (Evans and Guggenheim, 1988). Given that the martian crust is predominantly composed of basalt, and most sites do not show elevated mafic compositions, the more favorable alteration sequence results in the formation of saponite, not talc.

The global distribution of serpentine detections appears to fall into one of two categories. Most detections are seemingly isolated occurrences found within crater walls, knobby terrain, or impact ejecta (such as in Chia Crater), though they tend to be distributed widely across the southern highlands. The second category includes detections that appear to be part of a greater regional/local context with respect to the geology (such as in Claritas Rise and along the Thaumasia Highlands boundary) or other phases identified within the image scene or nearby scenes (such as Leighton Crater, Mawrth Vallis, and Nili Fossae). These two categories, and specific locales within them, have different implications for local and regional habitability as well as implications for general, global serpentinization processes throughout Mars' history. We will discuss the importance of the first category of detections for global-scale serpentinization on Mars and then focus on three local regions from the first group and discuss their implications for serpentinization induced habitable environments.

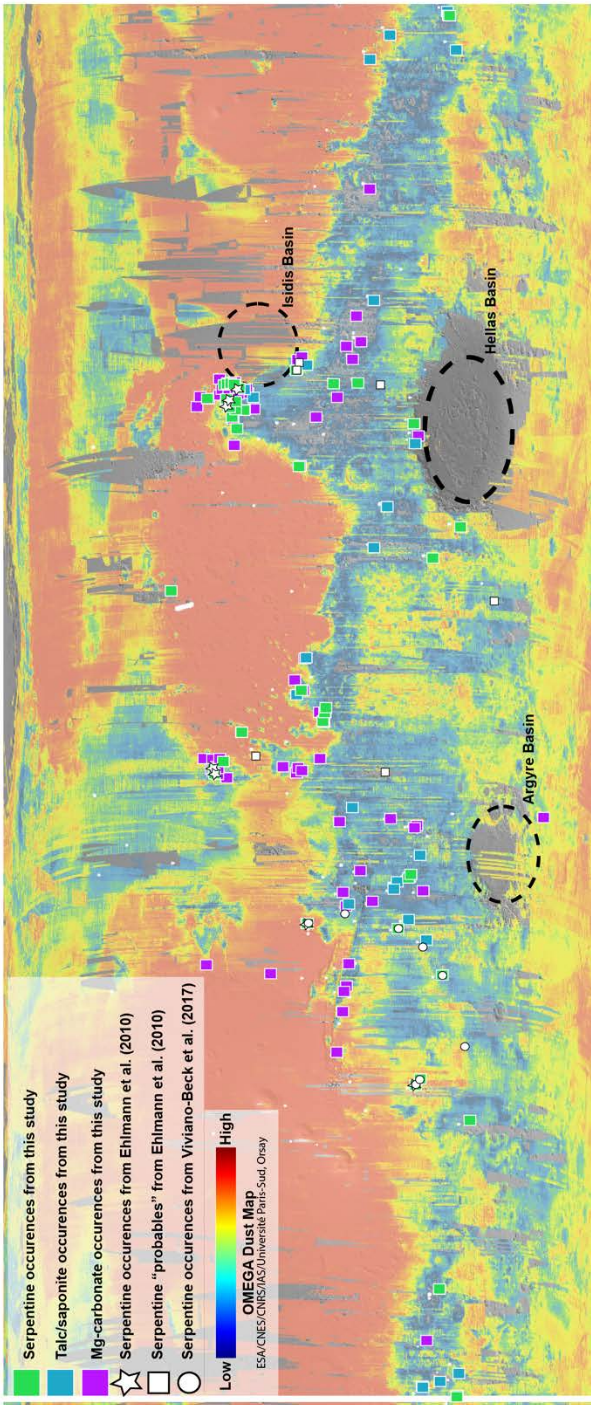

Figure 4.9. Global distribution of target transformation fits for investigated spectral types over colorized OMEGA dust map. As expected, and consistent with other studies searching for secondary alteration minerals, our detections are associated with relatively low dust covered areas. This low dust coverage provides an orbital window to interpret the mineralogy of exposed surfaces.

4.5.2.1 Globally Isolated Detections of Serpentine

Most detections of serpentine occur in seemingly isolated occurrences across the southern highlands. These detections are not often found with other investigated minerals and often do not relate to any general geologic or geochemical process that would have formed them. We attribute these detections to low concentrations of serpentine that likely formed during past subsurface serpentinization at depth. We can speculate that this may be evidence for variable olivine-compositions at depth across the martian subsurface, or indicate variations in crustal heat flow and fluid circulation, perhaps due to local magmatic processes or impact induced hydrothermal systems. However, most of these detections are in CRISM images that show exposures of reworked ancient terrains, with little geologic context. Regardless, though the number of serpentine detections are still low compared to other hydrated minerals on Mars, they are found across the southern highlands.

4.5.2.2 Leighton Crater

Michalski and Niles (2010) found spectral evidence in Leighton Crater for both carbonates (likely a Ca or Fe-bearing carbonate, such as siderite) and phyllosilicate phases (including a speculated spectral mixture of serpentine/vermiculite/saponite, though without the necessary 2.12 μm absorption for serpentine). It was suggested that these exposures are evidence for a deep crustal reservoir of sedimentary carbonate that was subsequently altered by volcanic lava flows and ultimately exposed by the impact that formed Leighton Crater (Michalski and Niles, 2010).

Detections from this study are consistent with the mineralogical interpretation put forth by Michalski and Niles (2010). We present strong evidence that a serpentine spectral component is present within Leighton Crater, as well as saponite likely implying that these exposures have experienced subsurface serpentinization (**Figure 4.6**). This study also corroborates Michalski and Niles, (2010) interpretation of a Ca or Fe-bearing carbonate versus a Mg-carbonate (**Figure 4.6**) and illustrates the sensitivity of this method to varying cation content. As hypothesized by Michalski and Niles (2010), given the serpentine's association with Al-bearing clays, it is unlikely that the impact simply excavated evidence for serpentinization of an ultramafic protolith, but instead has exposed a complicated series of alteration assemblages.

The exposures in Leighton Crater present clear mineralogical evidence for serpentinization, a set of reactions that imply a habitable environment. Additionally, the range of carbonate chemistry, and Fe/Mg- and Al-phyllosilicate phases implies that exposed rocks in Leighton Crater have experience a range of aqueous alteration processes that likely promoted habitable environments However, given that these reactions likely occurred in the subsurface and were later chemically altered and ultimately excavated by violent impact processes (Michalski and Niles, 2010), the astrobiological implications for these samples are less clear.

4.5.2.3 Mawrth Vallis

Mawrth Vallis has been studied extensively using both near-infrared (e.g., Bishop et al., 2008; Wray et al., 2008; McKeown et al., 2009; Loizeau et al., 2015) and thermal-infrared spectral datasets (Rogers and Bandfield, 2009; Michalski et al., 2013). The compositional stratigraphy found in Mawrth Vallis has been identified in several other martian locales, including western Nili Fossae, and consists of Fe/Mg-phyllosilicates (e.g., nontronite) overlain by Al-phyllosilicates (e.g., kaolinite, montmorillonite). This compositional stratigraphy is thought to be produced by extensive surface leaching and weathering of the upper unit (e.g., Murchie et al., 2009). Additionally, the Mawrth Vallis region exposes some of the highest concentration of phyllosilicates on the planet (Poulet et al., 2014; Rogers and Bandfield, 2009).

From this study, serpentine and Mg-carbonate appear to be common in the area, with most detections concentrated on the main Mawrth Vallis plateau where the highest concentration of phyllosilicates has been observed by others (e.g., Poulet et al., 2014). This supports previous identifications of serpentine around Mawrth Vallis (Ehlmann et al., 2010) and detections of Mg-carbonate in McLaughlin Crater (Michalski et el., 2013), with additional new detections (**Figure 4.7**).

We were unable to directly detect Mg-carbonate or serpentine-enriched surfaces using I/F spectral ratios or using band-depth parameters maps in the images flagged using factor analysis and target transformation. However, as discussed in Section 4.5.1, this does not preclude the existence of these spectral phases as being components of the overall CRISM scene. Given that this area has been highly weathered from the late-Noachian through the early-Hesperian (Loizeau et al., 2015), it may be possible that serpentinization was an active process in the past, perhaps an early global process. However, the geologic context for these reactions in Mawrth Vallis is less clear and somewhat ambiguous compared to other martian regions. There is not abundant evidence for olivine-rich basalts as in Nili Fossae, nor is there any evidence for an initial source of heat such as a nearby volcanic source or an impact-induced hydrothermal system.

The target transformation results in Mawrth Vallis are consistent with the known high mineralogical diversity in the region. Detections from target transformation fits for phases not specifically associated with serpentinization where clearly identified in this region. Exceptional fits for a Fe/Mg-phyllosilicate phase like nontronite and an Al-phyllosilicate phase like a montmorillonite/kaolinite mixture are present (**Figure 4.7**f). These identifications are not new (e.g., Bishop et al., 2008; Wray et al., 2008; McKeown et al., 2009; Loizeau et al., 2015), but are clearly observed and corroborated using this independent technique, speaking to the quality, and likely volume, of phyllosilicate exposures in Mawrth Vallis.

From an astrobiological perspective, Mawrth Vallis presents one (water) of the three (water, energy, nutrients/organics) key ingredients for life. The region shows clear evidence for sustained aqueous alteration for a long enough period to produce the globally recognized compositional stratigraphy of Fe/Mg-phyllosilicates overlain by Al-phyllosilicates. Our detections of serpentine implies that evidence for past serpentinization exists within these exposures, but the geologic context and timing for when the serpentinization reactions occurred and what subsequent geochemical processes have since occurred, makes the astrobiological potential of this region less clear. However, the rich diversity of mineralogical products in this region implies an extremely interesting aqueous history that likely connects to a global process that led to the globally recognized compositional stratigraphy discussed (such as in western Nili Fossae).

4.5.2.4 Nili Fossae

Nili Fossae is considered one of the most mineralogically diverse regions on Mars with a range of both primary and secondary alteration minerals (Hoefen et al., 2003, Hamilton and Christensen, 2005; Poulet et al., 2005; Bibring et al., 2006; Mangold et al., 2007; Mustard et al., 2007, 2009; Ehlmann et al., 2008, 2009, 2010; Tornabene et al., 2008; Brown et al., 2010; Viviano et al., 2013; Edwards and Ehlmann, 2015). Previous studies using traditional I/F spectral ratios and band-depth parameters maps showed evidence for three CRISM images in the region with serpentine-bearing surfaces (**Figure 4.10**; Ehlmann et al., 2009; 2010; Amador et al., in revision (Chapter 3)). The evidence for serpentine-bearing surfaces in Nili Fossae from these studies were limited and the diagnostic 2.12 μm absorptions are often weak and less clear than other serpentine examples elsewhere, such as in Claritas Rise (Ehlmann et al., 2010). The target transformation fits for serpentine presenting in this study show well defined 2.12 μm absorptions (e.g., **Figure 4.5**a) that are often more clear than those retrieved from traditional I/F spectral ratios.

Though the implications for serpentinization and habitability in Nili Fossae have been discussed by several other studies (e.g., Ehlmann et al. 2009; 2010; Brown et al., 2010; Viviano et al., 2013; Amador et al., in revision (Chapter 3)), this work presents several new components to the story that could only be gathered with the aid of factor analysis and target transformation. Modeled target transformation fits for serpentine are consistent with a variably altered spectral endmember. Given that the 2.32 µm absorption is shifted to slightly shorter wavelengths and the presence of a minor absorption near 2.4 µm, it is likely that serpentine exposures have been partially altered to a talc/saponite phase. The process of carbonation, the alteration of serpentine

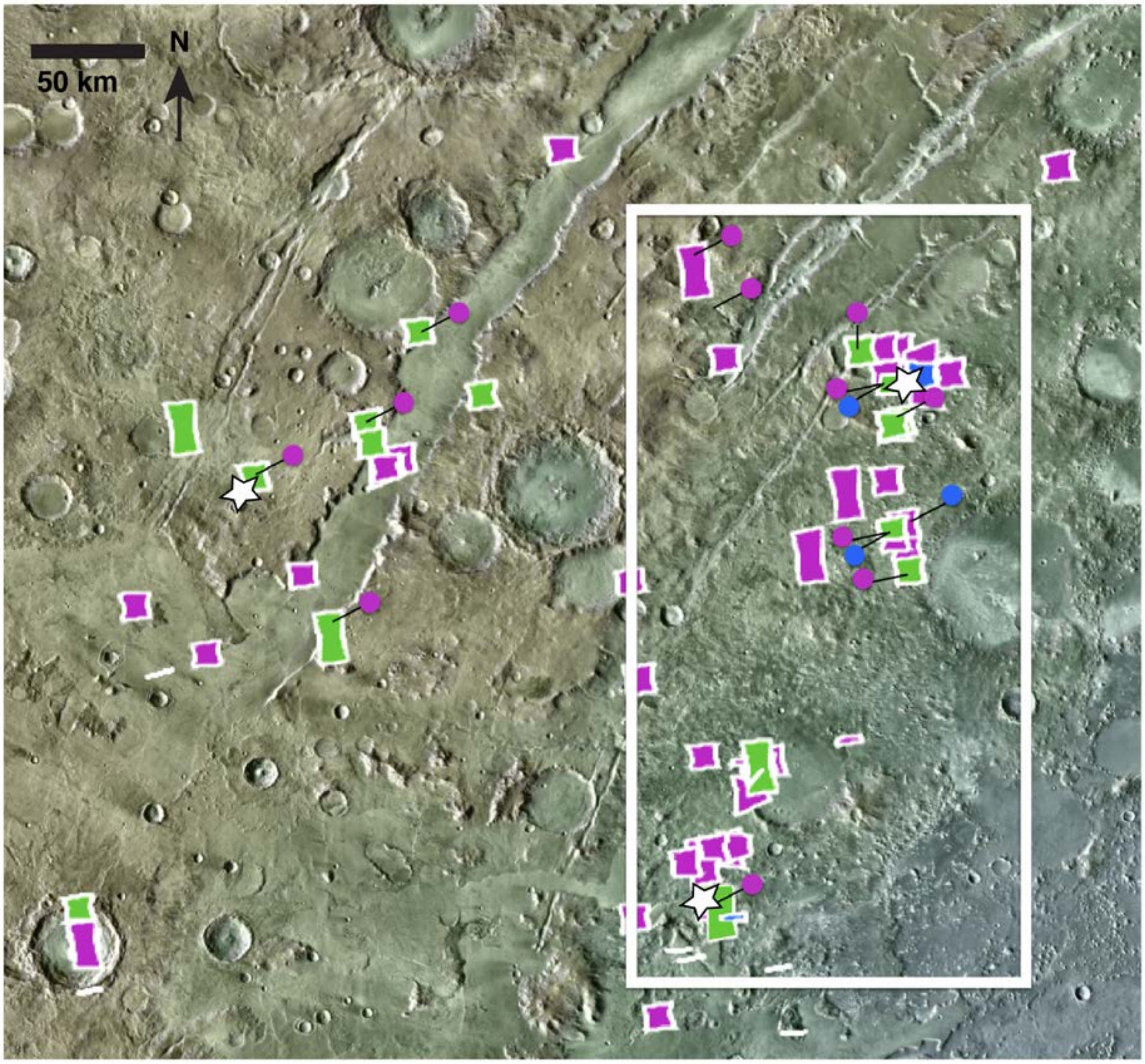

Figure 4.10. Colorized MOLA over THEMIS Day-IR mosaic of Nili Fossae centered around 76.09°E, 19.98°N. White inset shows area described in **Figure 4.11**. Colored stamps and circles indicate CRISM images with target transformation fits for investigated spectral types. Green indicates serpentine, magenta indicates Mg-carbonate, and blue indicates talc/saponite. The three starred CRISM images (FRT0000ABCB_07, FRS0002AE17_01, and HRL0000B8C2_07) are where previous studies have detected serpentine previously

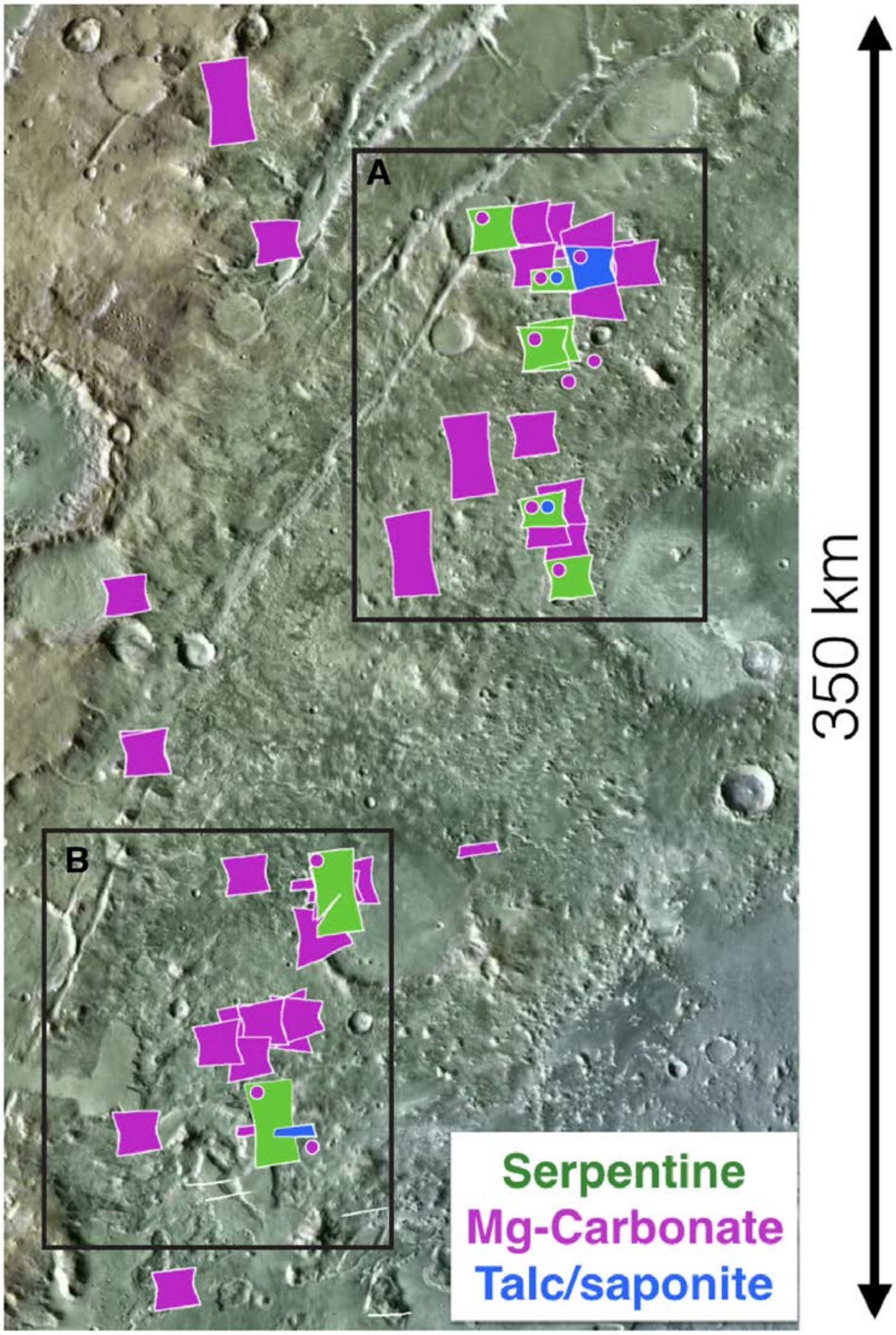

Figure 4.11. Colorized MOLA over THEMIS Day-IR mosaic. Most serpentine detections are concentrated in this region, east of the main Nili Fosse troughs. Black insets indicate areas shown in detail in **Figure 4.12**.

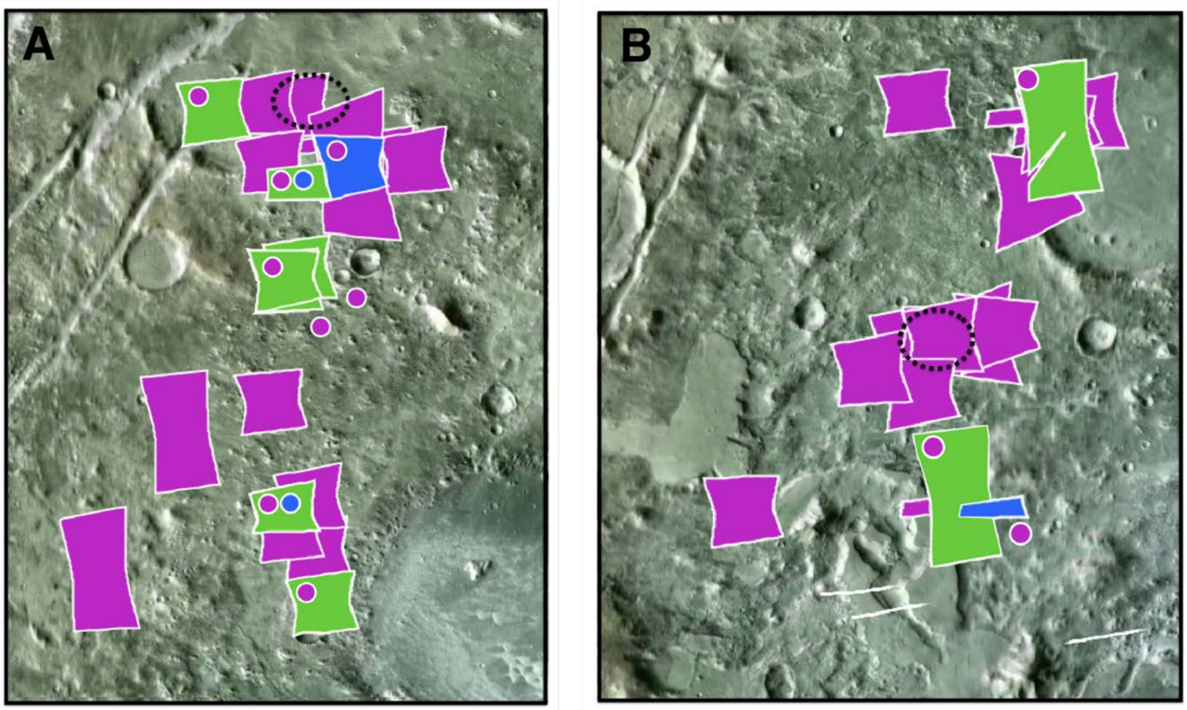

Figure 4.12. Colorized MOLA over THEMIS Day-IR mosaic. Panel A shows proposed Mars2020 landing site “Carbonate Plains”. Panel B shows proposed Mars2020 landing site “NE Syrtis”. Both landing sites would put a rover near the spectral types of interest.

to form talc and magnesite, has been proposed for this region by Viviano et al. (2013), and our results corroborate this idea, as the target transformation fits for serpentine consistently show this additional absorption at ~2.4 µm. Furthermore, given the mineralogical context in Nili Fossae specifically, the observed ~2.4 µm absorption is likely to be due to talc and/or talc+saponite rather than saponite alone, as this region, with high abundances of ultramafics, has undergone low-grade metamorphic processes (e.g., Viviano et al., 2013; Amador et al., in revision (Chapter 3)). In this sense, there is a clear geochemical means to produce talc in this region, unlike other observations of a talc/saponite spectral type, such as in Her Desher Vallis (See Section 4.4.1.3). These three phases (serpentine, Mg-carbonate, and talc) found in association with olivine-rich basalt point to low-temperature serpentinization processes followed by carbonation in this region as discussed by other studies (e.g., Viviano et al., 2013; Amador et al., in revision (Chapter 3)).

Here, we have also shown that serpentine is much more widespread across the Nili Fossae region than previously recognized and it is commonly found in association with Mg-carbonate (**Figure 4.10**). Known serpentine occurrences have expanded from three isolated images found across the region (Ehlmann et al., 2009; 2010; Amador et al, in revision (Chapter 3)) to 16 images, predominately clustered in the eastern "carbonate plains" (**Figure 4.10** inset, **Figure 4.11**, **Figure 4.12**). This area also corresponds to the highest concentrations of olivine within the olivine-rich basalt stratigraphic unit in the region (e.g., Ody et al., 2013). Talc detections are also concentrated in the eastern portion of Nili Fossae, though they are less common and geographically dispersed (**Figure 4.10**). These results are consistent with the overall story that serpentinization and carbonation reactions were likely the cause of the mineral suite observed in the eastern portion of Nili Fossae (e.g., Viviano et al., 2013), and were more pervasive than previously thought.

There are other isolated exposures of olivine-enriched basalt across the Nili Fossae region, but the mineral assemblage associated with serpentinization appears to be most common within the olivine-enriched exposures in the east, though there are some occurrences of serpentine, carbonate, and talc on the plateau west of the main Nili Fossae trough. There are several unique geologic factors that could have promoted the serpentinization and subsequent carbonation of the subsurface in the eastern portion of Nili Fossae. This is the area with the most expansive and highest concentration of olivine in the region (e.g., Hamilton and Christensen, 2005; Ody et al., 2013) – this would have provided the necessary protolith for the initiation and continuation of serpentinization. Additionally, the "carbonate plains" are found within a lower topographic elevation compared to much of the plateau around the Nili Fossae troughs as there is a south-east trending topographic gradient in the region, towards the Isidis Basin to the east (**Figure 4.13**). This may point to a path for fluid migration during the late-Noachian/early-Hesperian

Eras when these processes were likely occurring (e.g., Viviano et al., 2013; Amador et al., in revision (Chapter 3)), likely concentrated fluids towards the now exposed "carbonate plains" and making this location particularly susceptible to serpentinization and subsequent alteration to Mg-carbonate and talc.

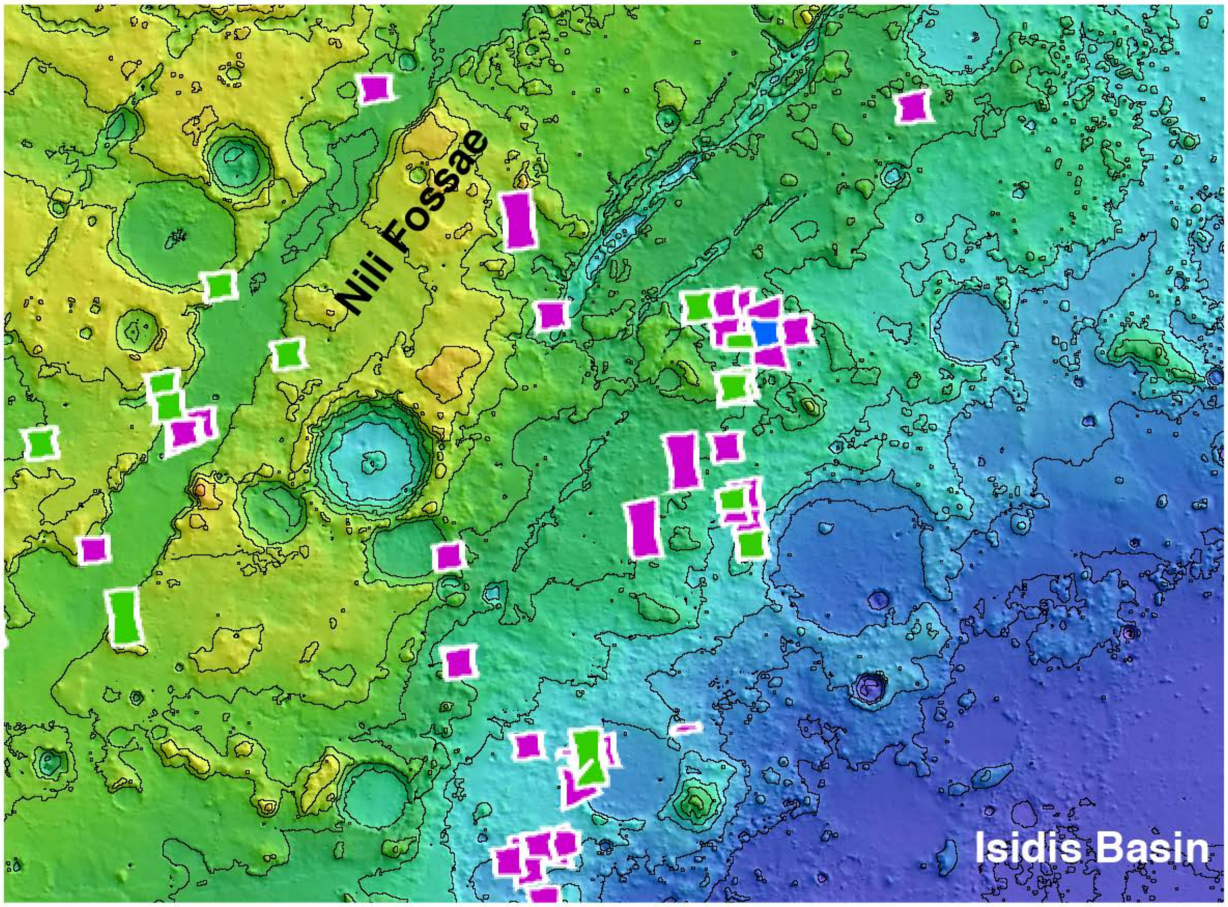

Figure 4.13. Colorized MOLA topography over THEMIS Day-IR mosaic with 200 m contour lines. Color stamps indicate CRISM image with target transformations fits for serpentine (green), Mg-carbonate (magenta) and talc/saponite (blue). The highest concentration of the mineral suite of interest is found at lower elevations relative to Nili Fossae, possibly along a hydrologic flow gradient from the higher Nili Fossae plateau towards Isidis Basin.

The Nili Fossae region particularly around and to the south of the "carbonate plains", provides abundant evidence for a once habitable environment. The observed mineralogical suite indicates that low-temperature serpentinization was once an active process in the region and this study shows how pervasive those reactions were. Additionally, the presence of this mineralogical suite associated with serpentinization, found within an olivine-rich unit, indicates that these reactions took place *in-situ*, with minimal geochemical and tectonic reworking, making the eastern portion of Nili Fossae a particularly compelling site to study with respect to past habitability.

4.5.3 Implications for global serpentinization processes on Mars and searching for regions with the highest potential for containing once habitable environments?

This study had shown abundant spectral evidence for the presence of serpentine across the southern highlands of Mars. For the most part, serpentine occurrences are isolated and occur at low enough concentrations that its detection in the available CRISM data necessitates the use of factor analysis and target transformation. Though these detections are somewhat ambiguous and their context can be difficult to place within a larger habitability framework, their detection is very interesting. Clearly, large-scale regional serpentinization processes in the near-subsurface (like in Nili Fossae) were rare on Mars. However, the fact that these low-concentration occurrences are found distributed across the southern highlands implies a global process. Given that the concentrations for these occurrences are so low and the serpentine is typically not found with other minerals that are usually associated with serpentinization, they probably represent old and reworked material. This may mean that serpentinization was a more common process very early on in Mars' history when the planet was more geologically active.

Only several regions on the planet contain serpentine-bearing exposures at high enough concentrations that they are detectable directly from ratioed I/F spectral data: Claritas Rise (Ehlmann et al., 2010; Viviano-Beck et al., 2017), along the Thaumasia Highlands (Viviano-Beck et al., 2017), Chia Crater (Ehlmann et al., 2010), and in Nili Fossae (Ehlmann et al., 2009; 2010; Amador et al., in revision (Chapter 3)). The geologic context and the processes that led to the exposure of serpentine-bearing surfaces in Claritas Rise and in Nili Fossae appear to be most straightforward. In Claritas Rise and along the edge of the Thaumasia Highlands, the serpentine-bearing rocks have likely been excavated from substantial depth, uplifted and exposed at the modern-day surface (e.g., Viviano-Beck et al., 2017). This region has been tectonically modified, due to its position to the southeast of the Tharsis region, for much of the Noachian and Hesperian (e.g., Carr and Head, 2010). This region also shows spectral evidence for zeolites and chlorite (Viviano-Beck et al., 2017), further implying that this region has been exposed to secondary alteration processes that are not associated with serpentinization but controlled by the tectonics of the region, inducing low-grade metamorphism. The serpentine exposed in this region helps constrain the tectonic setting of the region as described by Viviano-Beck et al., 2017, however, the astrobiological and habitability implications are limited given how reworked these surfaces are.

The geologic setting of serpentine-exposures in Nili Fossae is also unique compared to others across the planet. Serpentine-bearing surfaces are all found within an expansive olivine-rich basalt unit (Hoefen et al., 2003; Hamilton and Christensen, 2005; Mustard et al., 2007; Tornabene et al., 2008), approximately 30,000 km^2 in area. This unit is the largest, continuous exposures of olivine-rich bedrock on the planet (Ody et al., 2013) and contains between 20 and 30 wt% olivine ranging in composition from Fo_{68-75} (Hamilton and Christensen, 2005; Koeppen and Hamilton, 2008; Edwards and Ehlmann, 2015), implying a more Mg-rich composition along the olivine solid-solution series. This olivine-rich unit may have formed contemporaneously as an Isidis-related impact melt (Mustard et al., 2009) or, alternatively as post-Isidis impact event volcanic lava flows (Hamilton and Christensen, 2005; Tornabene et al., 2008).

It may be that this expansive olivine-rich unit makes Nili Fossae a unique setting for serpentinization on Mars. The other large impact basins on Mars, Argyre and Hellas Basins, also have circumferential olivine-rich exposures (e.g., Ody et al., 2013). However, we did not identify any serpentine-bearing surfaces near the olivine-rich exposures around Argyre Basin and only identified one location with serpentine *regionally* near an olivine-enriched exposure on the northern rim of Hellas Basin (**Figure 4.8**). Additionally, the olivine-rich surfaces near Nili Fossae have morphological and compositional differences from those found around the other large impact basins. The circumferential olivine associated with both Argyre and Hellas Basins are typically discontinuous and are found on the crests of knobs in hilly terrain (e.g., Ody et al., 2013). Additionally, the concentration of olivine at Nili Fossae is higher than for the other two large-scale circumferential olivine exposures around Argyre and Hellas Basins and may also have a larger olivine grain sizes (Ody et al., 2013). It may be that the expansive and continuous exposures of relatively high olivine abundances in Nili Fossae (e.g., Ody et al., 2013) aided in the initiation and continuation of serpentinization in the region. However, the fact that unaltered olivine remains in the area and it is only variably altered to serpentine, carbonate, and talc/saponite implies that the amount of serpentinization that occurred in the area was limited and the reactions did not go to completion, perhaps due to limited water availability (Amador et al., in revision (Chapter 3)).

The other geologically unique aspect to Nili Fossae relative to other sites with olivine-enriched bedrock is its proximity to the large Syrtis Major volcanic province. Syrtis Major was active beginning in the early-Hesperian (~3.7 Gya) (Hiesinger and Head, 2004); this regional heat source, in conjunction with the extensively fractured nature of the region (e.g., Saper and Mustard, 2013) and the olivine-enriched protolith may have provided the necessary conditions for a well-established low-temperature serpentinizing system, likely in the subsurface. These reactions would have lasted long enough to variably alter the olivine-rich basalt to serpentine, with subsequent alteration to both Mg-carbonate and talc (e.g., Viviano et al., 2013; Amador et al., in revision (Chapter 3)).

4.6 SUMMARY AND CONCLUSIONS

Minerals associated with serpentinization reactions such as serpentine, Mg-carbonate, talc/saponite have been identified across the southern highlands of Mars. Though found widespread, occurrences of these phases are still limited. These detections are not typically spatially correlated with one another or with ultramafic exposures as initially predicted except for in Nili Fossae.

Serpentine detections were typically only made possible using target transformation techniques of the available spectral data, not using I/F spectral ratios, implying that serpentine concentrations are low albeit present when taking all the available spectral information from a given scene into account. However, their presence across the southern highlands is widespread, implying global serpentinization processes likely occurring early in martian history as most exposures are reworked Noachian terrains.

Some exceptional regional to local settings were also highlighted using factor analysis and target transformation. Leighton Crater and Mawrth Vallis, though previously recognized as having highly altered phases, at exceptionally high volumes in Mawrth Vallis, now show additional evidence for more pervasive serpentinization (and other phases such Ca- or Fe-carbonate and Al-phyllosilicates). The serpentine detected in these two regions are low in concentration relative to the other phases identified in the region, and similarly necessitated the use of target transformation, and may be representative of the global low-concentration serpentine detected across the highlands. Especially in the case of Mawrth Vallis, the results of this study highlight the range and concentration of phyllosilicates present in the region.

Lastly, Nili Fossae stands out as a unique locale with clear detections of serpentine, Mg-carbonate, and a talc/saponite spectral phase (likely to be more consistent with talc, in this case) all within a well-defined olivine-rich layer indicating a once *in-situ* low-temperature serpentinizing system in the region. The astrobiological potential for Nili Fossae due to serpentinization has been discussed in detail in **Amador et al., in revision (Chapter 3).** This study shows that a) minerals associated with serpentinization are more pervasive in Nili Fossae than previously thought, and b) that this region is unique across Mars where we have access to exposures of the martian surface from available remote sensing data.

In the search for once habitable environments on Mars, Nili Fossae provides some of the most direct evidence for once having substantial aqueous activity under relatively low temperatures, a chemical means for metabolic energy in the form of H_2, and the geochemical means for creating low-order organics that are common in serpentinizing systems like CH_4. These reactions appear to have occurred *in-situ*, particularly concentrated in the eastern portion of Nili Fossae around and to the south of the “carbonate plains”. From an astrobiological standpoint, this region stands out as a compelling site for detailed analyses by future landed missions.

Chapter 5. CONCLUSIONS

The search for habitable environments on Mars will continue over the next decades with several new rovers and landers slated for launch by NASA and the European Space Agency, in addition to the inevitable human exploration of the martian surface that is to come. To send these exploration missions to the most promising locales for the highest scientific return requires the detailed interrogation of available orbital datasets. Given that many of NASA's scientific objectives rally behind the common goal of understanding the potential for habitable environments beyond modern Earth, the future of Mars exploration will require the adjustment of goals currently driven by the search for hydrated and aqueous environments to the more refined search for environments that show compelling evidence for metabolic energy sources, a means for acquiring organics and nutrients, in addition to clement aqueous conditions. Furthermore, with the ever-increasing load of planetary mission data being returned to Earth from Mars, new ways of analyzing spectral datasets will provide a more comprehensive understanding of the martian surface.

This dissertation advances our understanding of the past aqueous history and habitability potential of key locales on Mars by: 1) demonstrating that the Nili Fossae capping unit, previously thought to be unaltered, shows evidence for elevated concentrations of bulk-silica likely due to increased aqueous activity and adding to the known mineralogical diversity in the region, 2) demonstrating that the spectral suite and therefore minerals observed within the olivine-rich basalt unit in Nili Fossae are similar to those from the Lost City Hydrothermal Field on Earth implying a once habitable low-temperature serpentinizing system in the regions past, and 3) investigating the distributions of minerals associated with serpentinization across the martian surface from available orbital data, concluding that regional-scale near-surface serpentinizing systems were rare on Mars with the exception of the Nili Fossae region. Furthermore, this dissertation advances our understanding of ways to best leverage and analyze spectral wavelength regions and datasets by: 1) developing the “Weighted Absorption Center” Colorized Index maps with THEMIS multispectral data and showing that these indices can be correlated with near-infrared CRISM spectral data, 2) using thermal-infrared emissivity measurements in concert with near-infrared reflectance measurements to fully describe the bulk composition and spectral characteristics of an Earth astrobiological and spectral analog site to Nili Fossae, Mars, and 3) applying factor analysis and target transformation methods to the CRISM dataset in a global and comprehensive manner to find locales containing minerals associated with serpentinization that would have otherwise been missed using traditional analysis techniques. I include summaries of these findings below.

5.1 SUMMARY OF WORK

Chapter 2. The Nili Fossae region of Mars contains some of the most mineralogically diverse bedrock on the planet. Previous studies have established three main stratigraphic units in the region: a phyllosilicate-bearing basement rock, a variably altered olivine-rich basalt, and a capping rock. Chapter 2 presents evidence for the localized alteration of the northeast Nili Fossae capping unit, previously considered to be unaltered. Both near-infrared and thermal-infrared spectral datasets were analyzed, including the application of a method for determining the relative abundance of bulk-silica (SiO_2) over surfaces using Thermal Emission Imaging System (THEMIS) images. Elevated bulk-silica exposures are present on surfaces previously defined as unaltered capping rock. Given the lack of spectral evidence for phyllosilicate, hydrated silica, or quartz phases coincident with the newly detected exposures - the elevated bulk-silica may have formed under a number of aqueous scenarios, including as a product of the carbonation of the underlying olivine-rich basalt under moderate water:rock scenarios and temperatures. Regardless of formation mechanism, the detection of elevated bulk-silica exposures in the Nili Fossae capping unit extends the history of aqueous activity in the region to include all three of the main stratigraphic units.

Chapter 3. Low-temperature serpentinization is a critical process with respect to Earth's habitability and the Solar System. Exothermic serpentinization reactions often produce hydrogen as a direct byproduct and typically produce short-chained organic compounds indirectly. Chapter 3 presents the spectral and mineralogical variability in rocks from the serpentine-driven Lost City Hydrothermal Field on Earth and the olivine-rich region of Nili Fossae, Mars. Near- and thermal-infrared spectral measurements were made from a suite of Lost City rocks at wavelengths like those for instruments collecting measurements of the martian surface. Results from Lost City show a spectrally distinguishable suite of Mg-rich serpentine, Ca-carbonates, talc, and amphibole minerals. Aggregated detections of low-grade metamorphic minerals in rocks from Nili Fossae were mapped and yielded an additional serpentine exposure in the region, previously undetected. Direct comparison of the two spectral suites indicate similar mineralogy at both the Lost City Hydrothermal Field, Earth and in the Noachian (4 to 3.7 Ga) bedrock of Nili Fossae, Mars. Based on mapping of these spectral phases, the implied mineralogical suite appears to be extensive across the region and implies that serpentinization was once an active process, implying sustained liquid water, an energy source, and a means for prebiotic chemistry during a period when life was first emerging on Earth. Although the mineralogical assemblages identified on Mars are unlikely to be directly analogous to rocks that underlie the Lost City Hydrothermal Field, it is likely that similar geochemical processes (and associated sources of biologically-accessible energy) were once present in the subsurface, making Nili Fossae a compelling candidate for a once-habitable environment on Mars.

Chapter 4. Chapter 4 aimed to understand the global distribution of minerals associated with serpentinization, like those found in Nili Fossae and their relationship, if any, to other ultramafic regions on Mars. This distribution would provide a better understanding of the regions on Mars that once had the highest potential for habitability. To do this, we performed a comprehensive analysis of the entire CRISM spectral dataset. Given the magnitude of images (>13,000) and the subtle/weak spectral features associated with serpentine, we used factor analysis and target transformation methods to efficiently parse through the available CRISM data. These methods not only allow for the timely analysis of thousands of images, but provide a quantitative means to determine the significant spectral constituents of an image, even if they are only contained as spectral mixtures. These methods resulted in a global distribution map of CRISM images with a significant likelihood of containing the spectral types of interest. The methods used were successful in corroborating previous detections of serpentine using traditional CRISM analysis techniques, and found additional detections across the martian southern highlands. Serpentine detections were not particularly associated with ultramafic regions or with other mineral phases investigated (Mg-carbonate and talc/saponite), other than in Nili Fossae. Most serpentine detections were found in isolated exposures, associated with crater ejecta, knobby terrain, or as part of discontinuous layers in crater or valley walls. Some serpentine detections were found within a more complicated geologic or mineralogical context, such as in Claritas Rise, in Mawrth Vallis, and in Nili Fossae. Overall, the detection of serpentine from orbit were quite rare, though detections were found dispersed across the southern Highlands. Nili Fossae showed more pervasive and extensive detections of serpentine than previously thought, particularly in the eastern portion of Nili Fossae where the highest concentration of olivine-rich basalts is located. These findings imply that large, regional-scale near surface serpentinizing systems were likely rare on Mars, at least as observable today. Low-concentration serpentine detections across the southern highlands do however point to a global serpentinization system, likely early in Mars history when the planet was more geologically active. Nili Fossae appears to be unique amongst other olivine-enriched regions, potentially due to its proximity to the nearby Syrtis Major volcanic province. Northeast Nili Fossae shows the strongest evidence for a sustained, low-temperature serpentinizing system in its history, and is a compelling site for further study with respect to astrobiology.

5.2 FUTURE WORK

The fourth chapter of this dissertation demonstrated the power of factor analysis and target transformation applied to specific scientific questions, like the distribution of minerals associated with serpentinizing systems on Mars. Similar global-scale questions remain elusive in Mars research and the ability to parse through thousands of images in an efficient, and quantitative manner can provide substantial support to the types of interpretations made from the terabytes of available data.

One of these outstanding questions that could be supported using factor analysis and target transformation involves the nature of the martian atmosphere and the reconciliation of contradicting predications for atmospheric CO_2 stored as carbonate in the surface and near-subsurface of Mars. Orbital and ground based observations indicate episodes of sustained liquid water on the martian surface, while both empirical observations and theoretical models indicate low atmospheric pressure for much of Mars' history, thereby precluding the stability of liquid water. One important piece to this puzzle is understanding the occurrence of carbonates, a potential sink for atmospheric CO_2 in contact with liquid water. Additionally, recent literature provides highly varying constraints on the martian carbonate reservoir. Lacking to date is a rigorous and systematic interrogation of the martian surface to identify the presence of local-scale carbonate exposures. The methods used in Chapter 4 that leverage quantitative tools and techniques can also serve to better constrain the extent of carbonate identifiable from terabytes of spectral data of Mars. Results from Chapter 4 already demonstrated these techniques' ability to distinguish between Mg-, Ca-, and Fe-carbonate (e.g., in Leighton Crater), and initial mapping of all carbonate phases indicated a wider distribution than previously thought (e.g., Wray et al., 2016). The study of carbonate distribution on Mars is a natural, and compelling, next step after the completion of this dissertation work and would provide a firm handle on the distribution and abundance of carbonate exposures detectable from orbit thereby advancing our understanding of crustal carbonate reservoir on Mars.

BIBLIOGRAPHY

Abrajano, T.A., Sturchio, N.C., Bohlke, J.K., Lyon, G.L., Poreda, R.J., Stevens, C.M., 1988. Methane-hydrogen gas seeps, Zambales Ophiolite, Phillipines: Deep or shallow origin? Chemical Geology 71, 1-3, 211-222. doi: 10.1016/0009-2541(88)90116-7.x

Amador, E.S., Bandfield, J.L., 2016. Elevated bulk-silica exposures and evidence for multiple aqueous alteration episodes in Nili Fossae, Mars. Icarus 276, 39–51. doi:10.1016/j.icarus.2016.04.015

Bandfield, J.L., 2008. High-silica deposits of an aqueous origin in western Hellas Basin, Mars. Geophys. Res. Lett. 35, 1–5. doi:10.1029/2008GL033807

Bandfield, J.L., 2002. Global mineral distributions on Mars. J. Geophys. Res. 107, 5042. doi:10.1029/2001JE001510

Bandfield, J.L., 2000. A Global View of Martian Surface Compositions from MGS-TES. Science (80-). 287, 1626–1630. doi:10.1126/science.287.5458.1626

Bandfield, J.L., Christensen, P.R., Smith, M.D., 2000. Spectral data set factor analysis and end-member recovery: Application to analysis of Martian atmospheric particulates. J. Geophys. Res. 105, 9573. doi:10.1029/1999JE001094

Bandfield, J.L., Edwards, C.S., Montgomery, D.R., Brand, B.D., 2013a. The dual nature of the martian crust: Young lavas and old clastic materials. Icarus 222, 188–199. doi:10.1016/j.icarus.2012.10.023

Bandfield, J.L., Amador, E.S., Thomas, N.H., 2013b. Extensive hydrated silica materials in western Hellas Basin, Mars. Icarus 226, 1489–1498. doi:10.1016/j.icarus.2013.08.005

Bandfield, J.L., D. Rogers, M.D. Smith, P.R. Christensen, Atmospheric correction and surface spectral unit mapping using Thermal Emission Imaging System data 2004a, Journal of Geophysical Research, 10.1029/2004JE002289.

Bandfield, J.L., Hamilton, V.E., Christensen, P.R., McSween, H.Y., 2004b. Identification of quartzofeldspathic materials on Mars. J. Geophys. Res. E Planets 109, 1–14. doi:10.1029/2004JE002290

Barnes, I., Neil, J.., Trescase, J.J., 1978. Present day serpentinization in New Caledonia , Oman and Yugoslavia. Geochim. Cosmochim. Acta 42, 144–145.

Bibring J.-P, et al., 2004. OMEGA: Observatoire pour la Mineralogie, l'Eau, les Glaces et l'Activite, in Mars Express; The Scientific Payload, edited by Andrew Wilson, pp. 37-49, ESA Publication Division, ESTEC, Noordwijk, Netherlands

Bibring, J.-P., Langevin, Y., Mustard, J.F., Poulet, F., Arvidson, R., Gendrin, A., Gondet, B., Mangold, N., Pinet, P., Forget, F., Berthé, M., Bibring, J.-P., Gendrin, A., Gomez, C., Gondet, B., Jouglet, D., Poulet, F., Soufflot, A., Vincendon, M., Combes, M., Drossart, P., Encrenaz, T., Fouchet, T., Merchiorri, R., Belluci, G., Altieri, F., Formisano, V., Capaccioni, F., Cerroni, P., Coradini, A., Fonti, S., Korablev, O., Kottsov, V., Ignatiev, N., Moroz, V., Titov, D., Zasova, L., Loiseau, D., Mangold, N., Pinet, P., Douté, S., Schmitt, B., Sotin, C., Hauber, E., Hoffmann, H., Jaumann, R., Keller, U., Arvidson, R., Mustard, J.F., Duxbury, T., Forget, F., Neukum, G., 2006. Global mineralogical and aqueous mars history derived from OMEGA/Mars Express data. Science 312, 400–404. doi:10.1126/science.1122659

Bishop, J.L. and Pieters, C.M., 1995. Low-temperature and low atmospheric pressure infrared reflectance spectroscopy of Mars soil analog materials. Journal of Geophysical Research, 100, 5369-5379.

Bishop J. L., Murad E. and Dyar M. D., 2002. The Influence of Octahedral and Tetrahedral Cation Substitution on the Structure of Smectites and Serpentines as Observed Through Infrared Spectroscopy. Clay Miner., 37, 617-628.

Bishop, J.L., and 11 colleagues, 2008. Phyllosilicate Diversity and Past Aqueous Activity Revealed at Mawrth Vallis, Mars. Science, 321, 830101.1126/science.1159699

Boschi, C., Fruh-Green, G.L., Delacour, A., Karson, J.A., Kelley, D.S., 2006. Mass transfer and fluid flow during detachment faulting and development of an oceanic core complex, Atlantis Massif (MAR 30 ° N). Geo 7. doi:10.1029/2005GC001074

Brazelton, W.J., Schrenk, M.O., Kelley, D.S., Baross, J., 2006. Methane- and sulfur-metabolizing microbial communities dominate the lost city hydrothermal field ecosystem. Appl. Environ. Microbiol. 72, 6257–6270. doi:10.1128/AEM.00574-06

Brazelton, W.J., Ludwig, K.A., Sogin, M.L., Andreishcheva, E.N., Kelley, D.S., Shen, C., Edwards, R.L., Baross, J.A., 2010. Archaea and bacteria with surprising microdiversity show shifts in dominance over 1,000-year time scales in hydrothermal chimneys. Proc. Natl. Acad. Sci. USA 107, 1612–1617. doi:10.1073/pnas.0905369107

Brazelton, W.J., Mehta, M.P., Kelley, D.S., Baross, J.A., 2011. Physiological differentiation within a single-species biofilm fueled by serpentinization. mBio 2(4):e00127-11. doi:10.1128/mBio.00127-11.

Brown, A.J., Hook, S.J., Baldridge, A.M., Crowley, J.K., Bridges, N.T., Thomson, B.J., Marion, G.M., de Souza Filho, C.R., Bishop, J.L., 2010. Hydrothermal formation of Clay-Carbonate alteration assemblages in the Nili Fossae region of Mars. Earth Planet. Sci. Lett. 297, 174–182. doi:10.1016/j.epsl.2010.06.018

Buczkowski, D.L., Seelos, K., Murchie, S., Seelos, F., Malaret, E., Hash, C., and the CRISM Team, 2010. Extensive phyllosilicate-bearing layer exposed by valley systems in North-West Noachis Terra, LPSC XXXXI, Abstract #1458.

Carr, M.H., and Head, J.W., 2010. Geologic history of Mars. Earth and Planetary Science Letters, 294 (3-4), 185-203. Doi: 10.1016/j.epsl.2009.06.042

Carter, J., and F. Poulet, 2013. Ancient plutonic processes on Mars inferred from the detection of possible anorthositic terrains, Nature Geosci, 6(12), 1008-1012, doi: 10.1038/ngeo1995

Carter, J., Poulet, F., Bibring, J.-P., Mangold, N., Murchie, S., 2013. Hydrous minerals on Mars as seen by the CRISM and OMEGA imaging spectrometers: Updated global view. J. Geophys. Res. Planets 118, 831–858. doi:10.1029/2012JE004145.

Christensen, P.R., Bandfield, J.L., Hamilton, V.E., Howard, D.A., Lane, M.D., Piatek, J.L., Ruff, S.W., Stefanov, W.L., 2000. A Thermal Emission Spectral Library of Rock-forming Minerals, J. Geophys. Res., 105, 9735-9739.

Christensen, P.R., Jakosky, B.M., Kieffer, H.H., Malin, M.C., McSween, H.Y., Nealson, K., Mehall, G.L., Silverman, S.H., Ferry, S., Caplinger, M., Ravine, M., 2004. The Thermal Emission Imaging System (THEMIS) for the Mars 2001 Odyssey Mission. Space Sci. Rev. 110, 85–130. doi:10.1023/B:SPAC.0000021008.16305.94

Christensen, P.R.; Engle, E.; Anwar, S.; Dickenshied, S.; Noss, D.; Gorelick, N.; Weiss-Malik, M.; JMARS – A Planetary GIS, http://adsabs.harvard.edu/abs/2009AGUFMIN22A..06C

Clark, R.N., King, T.V. V., Klejwa, M., Swayze, G. a., Vergo, N., 1990. High spectral resolution reflectance spectroscopy of minerals. J. Geophys. Res. 95, 12653. doi:10.1029/JB095iB08p12653

Clark, R.N., Swayze, G.A., Wise, R., Livo, E., Hoefen, T., Kokaly, R., Sutley, S.J., 2007. USGS Digital Spectral Library splib06a: U.S. Geological Survey, Digital Data Series 231.

Cuadros, J., Dekov, V.M., Diore, S., 2008. Crystal chemistry of the mixed-layer sequence talc-talc-smectite-smectite from submarine hydrothermal vents. Am. Mineral. 93, 1338-1348.

Delacour, A., Früh-Green, G.L., Bernasconi, S.M., Schaeffer, P., Kelley, D.S., 2008. Carbon geochemistry of serpentinites in the Lost City Hydrothermal System (30°N, MAR). Geochim. Cosmochim. Acta 72, 3681–3702. doi:10.1016/j.gca.2008.04.039

Denny, A.R., Kelley, D.S., Fruh-Green, G.L., 2016. Geologic evolution of the Lost City Hydrothermal Field, Geochemistry, Geophysics, Geosystems. Geobiology 17, 375–394. doi:10.1002/2015GC005869

Domagal-Goldman, S.D., Wright, K.E., Adamala, K., Anderson, R., Arney, G., Atri, D., Azua-Bustos, A., Bowman, J.S., Brazelton, W.J., Brennecka, G.A., Carns, R., Chopra, A., Colangelo-Lillis, J., Crockett, C.J., DeMarines, J., Frank, E.A., Frantz, C., de la Fuente, E., Galante, D., Glass, J., Gleeson, D., Glein, C.R., Goldblatt, C., Horak, R., Horodyskyj, L., Kacar, B., Kereszturi, A., Knowles, E., Mayeur, P., Mcglynn, S., Miguel, Y., Montgomery, M., Neish, C., Noack, L., Rugheimer, S., Stueken, E.E., Tamez-hidalgo, P., Walker, S.I., Wong, T., 2016. The Astrobiology Primer v2.0. Astrobiology 16, 561–653. doi:10.1089/ast.2015.1460

Edwards, C.S. and Ehlmann, B.L., 2015. Carbon sequestration on Mars. Geology 43, G36983.1. doi:10.1130/G36983.1

Edwards, C.S., Nowicki, K.J., Christensen, P.R., Hill, J., Gorelick, N., Murray, K., 2011. Mosaicking of global planetary image datasets: 1. Techniques and data processing for Thermal Emission Imaging System (THEMIS) multi-spectral data. J. Geophys. Res. E Planets 116, 1–21. doi:10.1029/2010JE003755

Ehlmann, B. L. and C. S. Edwards, 2014. The Composition of the Martian Surface from Infrared Spectroscopy, Annual Reviews in Earth and Planetary Sciences, 42(1), 291-315, doi: 10.1146/annurev-earth-060313-055024

Ehlmann, B.L., Mustard, J.F., Murchie, S.L., 2010. Geologic setting of serpentine deposits on Mars. Geophys. Res. Lett. 37, 1–5. doi:10.1029/2010GL042596

Ehlmann, B.L., Mustard, J.F., Murchie, S.L., Poulet, F., Bishop, J.L., Roach, L.H., Roush, T.L., Swayze, G.A., Wray, J.J., 2008. Orbital identification of carbonate-bearing rocks on Mars. Science (80-.). 322, 1828–1832.

Ehlmann, B.L., Mustard, J.F., Swayze, G. a., Clark, R.N., Bishop, J.L., Poulet, F., Des Marais, D.J., Roach, L.H., Milliken, R.E., Wray, J.J., Barnouin-Jha, O., Murchie, S.L., 2009. Identification of hydrated silicate minerals on Mars using MRO-CRISM: Geologic context near Nili Fossae and implications for aqueous alteration. J. Geophys. Res. E Planets 114, 1–33. doi:10.1029/2009JE003339

Evans, B.W., 2010. Lizardite versus antigorite serpentinite : Magnetite , hydrogen , and life (?). Geology 38, 879–882. doi:10.1130/G31158.1

Evans, B.W., 2004. The Serpentinite Multisystem Revisited: Chrysotile Is Metastable. Int. Geol. Rev. 46, 479–506. doi:10.2747/0020-6814.46.6.479

Evans, B.W. and S. Guggenheim, 1988. Talc, Pyrophyllite, and Related Minerals. In: Hydrous Phyllosilicates (exclusive of micas), edited by S.W. Bailey, Reviews in Mineralogy Volume 19, Mineralogical Society of America, pp 225-294.

Feely, K.C., Christensen, P.R., 1999. Application to igneous and metamorphic rocks. October 104.

Frost, B. R., and J. S. Beard (2007), On silica activity and serpentinization, *J. Petrol.*, **48**, 1351–1368, doi:10.1093/petrology/egm021.

Früh-Green, G.L., Kelley, D.S., Bernasconi, S.M., Karson, J.A., Ludwig, K.A., Butterfield, D.A., Boschi, C., Proskurowski, G., 2003. 30,000 years of Hydrothermal Activity at the Lost City Hydrothermal Field. Science 301 (5632), 495-498.

Früh-Green, G.L., Connolly, J.A.D., Plas, A., Kelley, D.S., and Groberty, B., (2004). Serpentinization of Oceanic Peridotites: Implications for Geochemical Cycles and Biological Activity. In: The Subseafloor Biosphere at Mid-Ocean Ridges, eds., W.S.D. Wilcock, E. F. DeLong, D.S. Kelley, J.A. Baross, S.C. Cary, Geophysical Monograph Series 144, 119-136.

Füh-Green, G.L., Orcutt, B.N., Green, S., Cotterill, C., and the Expedition 357 Scientists, 2016. Expedition 357 Preliminary Report: Atlantis Massif Serpentinization and Life. International Ocean Discovery Program.http://dx.doi.org/10.14379/iodp.pr.357.2016

Fuchs, G., 2011. Alternative pathways of carbon dioxide: Insights into the early evolution of life? Annu. Rev. Microbiol, 65:631-58. doi:10.1146/annurev-micro-090110-102801.

Gaffey, S., 1987. theory . Mn 2 + and Fe 2 + produce very strong using the Gaussian Fitting (GFIT) routine. J. Geophys. Res. 92, 1429–1440

Gillespie, A.R., Kahle, A.B., Walker, R.E., 1986. Color enhancement of highly correlated images. I - Decorrelation and HSI contrast stretches. Remote Sens. Environ. 235, 209–235. doi:10.1016/0034-4257(86)90044-1

Geminale, A., Grassi, D., Altieri, F., Serventi, G., Carli, C., Carrozzo, F.G., … Frigeri, A., 2015. Removal of atmospheric features in near infrared spectra by means of principal component analysis and target transformation on Mars: I. Method. Icarus, 253, 51-65. Doi: 10.1016/j.icarus.2015.02.012

Glotch, T.D. and Bandfield, J.L., 2006. Determination and interpretation of surface and atmospheric Miniature Thermal Emission Spectrometer spectral endmembers at the Meridiani Planum landing site. Journal of Geophysical Research: Planets, 111(12), 1-12. Doi:10.1029/2005JE002671

Glotch, T.D. and Rogers, A.D., 2013. Evidence for magma-carbonate interactions beneath Syrtis Major, Mars. Journal of Geophysical Research: Planets, 118(1), 126-137. Doi:10.1029/2012JE004230

Greenberger, R.N., Mustard, J.F., Cloutis, E.A., Pratt, L.M., Sauer, P.E., Mann, P., Turner, K., Darby Dyar, M., Bish, D., (2015) Serpentinization, iron oxidation, and aqueous conditions in an ophiolite: Implications for hydrogen production and habitability on Mars, Earth and Planetary Science Letters, 416, 21-34, doi:10.1016/j.epsl.2015.02.002

Hamilton, V.E. and Ruff S.W., (2012). Distribution and characteristics of Adirondack-class basalt as observed by mini-TES in Gusev Crater, Mars and its possible volcanic source. Icarus, 218(2), 917-949. Doi:10.1016/j.icarus.2012.01.011

Hamilton, V.E., Christensen, P.R., 2000. Determining the modal mineralogy of mafic and ultramafic igneous rocks using thermal emission spectroscopy 105, 9717–9733.

Hamilton, V.E., Christensen, P.R., 2005. Evidence for extensive, olivine-rich bedrock on Mars. Geology 33, 433–436. doi:10.1130/G21258.1

Hamilton, V.E., Christensen, P.R., McSween, H.Y., Bandfield, J.L., 2003. Searching for the source regions of Martian meteorites using MGS TES: Integrating Martian meteorites into the global distribution of igneous materials on Mars. Meteorit. Planet. Sci. 38, 871–885. doi:10.1111/j.1945-5100.2003.tb00284.x

Heinen W. and A.M Lauwers, 1996. Organic sulfur compounds resulting from the interaction of iron sulfide, hydrogen sulfide and carbon dioxide in anaerobic aqueous environments. Origins of Life and Evolution of the Biosphere 26, 131-150.

Hiesinger, H., Head III, J.W., 2004. The Syrtis Major volcanic province, Mars: Synthesis from Mars Global Surveyor data. J. Geophys. Res. 109, E01004. doi:10.1029/2003je002143

Hoefen, T.M., Clark, R.N., Bandfield, J.L., Smith, M.D., Pearl, J.C., Christensen, P.R., 2003. Discovery of olivine in the Nili Fssae region of Mars. Science 302, 627–630. doi:10.1126/science.1089647

Holm, N.G. and J.L. Charlou, 2001. Initial indications of abiotic formation of hydrocarbons in the Rainbow ultramafic hydrothermal system, Mid-Atlantic Ridge. Earth and Planetary Science Letters, 191, 1-8, doi:10.1016/S0012-821X(01)00397-1.

Hostetler, P.B., Coleman, R.G., Mumpton, F.A., Evans, B.W., 1966. Brucite in Alpine Serpentinites, Am. Mineral., 51, 75-98

Huang, J., Edwards, C.S., Ruff, S.W., Christensen, P.R., Xiao, L., 2013. A new method for the semiquantitative determination of major rock-forming minerals with thermal infrared multispectral data: Application to THEMIS infrared data. J. Geophys. Res. Planets 118, 2146–2152. doi:10.1002/jgre.20160

Hunt, G.R., 1980. Electromagnetic radiation: The communication link in remote sensing. In B.S. Siegel and A.R. Gillespie (Eds.), Remote sensing in Geology (pp. 5-45). New York: John Wiley.

Hunt, G.R., and J.W. Salisbury, 1971. Visible and Near-infrared Spectra of Minerals and Rocks: II Carbonates. Mod. Geol. 2, 23-30

Hunt, G.R., 1977. Spectral signatures of particulate minerals in the visible and near infrared. Geophysics 42, 501–413.

Hynek, B.M., Beach, M., Hoke, M.R.T., 2010. Updated global map of Martian valley networks and implications for climate and hydrologic processes. Journal of Geophysical Research: Planets, 115, E9, 2156-2202.

Karson, J. a., Früh-Green, G.L., Kelley, D.S., Williams, E. a., Yoerger, D.R., Jakuba, M., 2006. Detachment shear zone of the Atlantis Massif core complex, Mid-Atlantic Ridge, 30 °n. Geochemistry, Geophys. Geosystems 7. doi:10.1029/2005GC001109

Kelemen, P. B., and J. Matter (2008), In situ carbonation of peridotite for CO2 storage, PNAS, 105(45), 17295-17300, doi: 10.1073/pnas.0805794105.

Kelley, D.S., Karson, J. a, Früh-Green, G.L., Yoerger, D.R., Shank, T.M., Butterfield, D. a, Hayes, J.M., Schrenk, M.O., Olson, E.J., Proskurowski, G., Jakuba, M., Bradley, A., Larson, B., Ludwig, K., Glickson, D., Buckman, K., Bradley, A.S., Brazelton, W.J., Roe, K., Elend, M.J., Delacour, A., Bernasconi, S.M., Lilley, M.D., Baross, J. a, Summons, R.E., Sylva, S.P., 2005. A serpentinite-hosted ecosystem: the Lost City hydrothermal field. Science 307, 1428–1434. doi:10.1126/science.1102556

Kelley, D.S., Karson, J.A., Butter, D.A., Lilley, M.D., Blackman, D.K., Fru, G.L., Olson, E.J., Schrenk, M.O., Roe, K.K., Lebon, G.T., Rivizzigno, P., Party, A.-S., 2001. An off-axis hydrothermal vent field near the Mid-Atlantic Ridge at 30 8 N. Nature 412, 8–12.

Klein and Garrido, 2011. Thermodynamic constraints on mineral carbonation of serpentinized peridotite, Lithos, 126, 147-160.

Koeppen, W.C., Hamilton, V.E., 2008. Global distribution, composition, and abundance of olivine on the surface of Mars from thermal infrared data. J. Geophys. Res. 113, 1–23. doi:10.1029/2007JE002984

Kraft, M.D., Michalski, J.R., and Sharp, T.G, 2003. Effects of pure silica coatings on thermal emission spectra of basaltic rocks: Considerations for Martian surface mineralogy. Geophys. Res. Lett. 30, 2288. doi:10.1029/2003GL018848

Kreysing, M., Keil, L., Lanzmich, S., Braun, D., 2015. Heat flux across an open pore enables the continuous replication and selection of oligonucleotides towards increasing length. Nature Chemistry, 7, 203-208. doi: 10.1038/NCHEM.2155.

Lane, M.D., 1999. Midinfrared optical constants of calcite and their relationship to particle size effects in thermal emission spectra of granular calcite. J. Geophys. Res. Planets 104, 14099–14108. doi:10.1029/1999JE900025

Lang, S.Q., Butterfield, D.A., Schulte, M., Kelley, D.S., Lilley, M.D., 2010. Elevated concentrations of formate , acetate and dissolved organic carbon found at the Lost City hydrothermal field. Geochim. Cosmochim. Acta 74, 941–952. doi:10.1016/j.gca.2009.10.045

Loizeau, D., Mangold, N., Poulet, F., Bibring, J.-P, Bishop, J.L., Michalski, J., Quantin, C., 2015. High resolution mapping of the martian candidate landing site at Mawrth Vallis: history of the clay-rich unit. Journal of Geophysical Research, 120, 11, 2169-9100.

Lopez-Garcia, P., Vereshchaka, A., 2007. Eukaryotic diversity associated with carbonates and fluid-seawater interface in Lost City hydrothermal field. Environmental Microbiology, 9(2), 546-554, doi:10.1111/j.1462-2920.2006.01158.x

Lowell, R.P., Rona, P.A., 2002. Seafloor hydrothermal systems driven by the serpentinization of peridotite. Geophys. Res. Lett. 29, 0–3.

Ludwig, K.A., Kelley, D.S., Butterfield, D.A., Nelson, B.K., Früh-Green, G.F., 2006. Formation and evolution of carbonate chimneys at the Lost City Hydrothermal Field, Geochimica et Cosmochimica Acta 70, 3625-3645.

Ludwig, K.A., Shen, C.-C., Kelley, D.S., Cheng, H., Edwards, R.L., 2011. U–Th systematics and 230Th ages of carbonate chimneys at the Lost City Hydrothermal Field. Geochim. Cosmochim. Acta 75, 1869–1888. doi:http://dx.doi.org/10.1016/j.gca.2011.01.008

Lyon, R.J.P., 1965. Analysis of rocks by spectral infrared emission (8 to 25 microns), Econ. Geol. 60:715-736.

Malamud, U., Prialnik, D., 2013. Modeling serpentinization : Applied to the early evolution of Enceladus and Mimas. Icarus 225, 763–774. doi:10.1016/j.icarus.2013.04.024

Malinowski, E.R., 1991. Factor Analysis in Chemistry, 2nd ed., New York: John Wiley.

Malin, M.C., Bell, J.F., Cantor, B.A., Caplinger, M.A., Calvin, W.M., Clancy, R.T., Edgett, K.S., Edwards, L., Haberle, R.M., James, P.B., Lee, S.W., Ravine, M.A., Thomas, P.C., Wolff, M.J., 2007. Context Camera Investigation on board the Mars Reconnaissance Orbiter. J. Geophys. Res. 112, E05S04. doi:10.1029/2006JE002808

Mangold, N., Poulet, F., Mustard, J.F., Bibring, J.-P., Gondet, B., Langevin, Y., Ansan, V., Masson, P., Fassett, C., Head, J.W., Hoffmann, H., Neukum, G., 2007. Mineralogy of the Nili Fossae region with OMEGA/Mars Express data: 2. Aqueous alteration of the crust. J. Geophys. Res. 112, E08S04. doi:10.1029/2006JE002835

McCollom, T.M., Seewald, J.S., 2007. Abiotic Synthesis of Organic Compounds in Deep-Sea Hydrothermal Environments on Abiotic Synthesis. Chem. Rev. 107, 382–401.

McGuire, P.C., Bishop, J.L., Brown, A.J., Fraeman, A. a., Marzo, G. a., Frank Morgan, M., Murchie, S.L., Mustard, J.F., Parente, M., Pelkey, S.M., Roush, T.L., Seelos, F.P., Smith, M.D., Wendt, L., Wolff, M.J., 2009. An improvement to the volcano-scan algorithm for atmospheric correction of CRISM and OMEGA spectral data. Planet. Space Sci. 57, 809–815. doi:10.1016/j.pss.2009.03.007

McKeown, N,K., Bishop, J.L, Noe Dobrea, E.Z., Ehlmann, B.L., Parente, M., Mustard, J.F., Murchie, S.L., Swayze, G.A., Bibring, J.-P, Silver, E.A., 2009. Characterization of phyllosilicates observed in the central Mawrth Vallis region, Mars, their potential formation processes, and implications for past climate. Journal of Geophysical Research, 114. Doi:0.10.1029/2008JE003301

McSween, H.Y., Taylor, G.J., Wyatt, M.B., 2009. Elemental Composition of the Martian Crust. Science, 324, 5928, 736-739. doi:10.1126/science.1165871

McSween, H.Y., Labotka, T.C., Viviano-Beck, C.E., 2015. Metamorphism in the Martian crust. Meteorit. Planet. Sci. 50, 590–603. doi:10.1111/maps.12330

Michalski, J.R., and Niles, P.B., 2010. Deep crustal carbonate rocks exposed by meteor impact on Mars. Nature Geosciences, 3(11), 751-755. Doi:10.1038/ngeo971

Michalski, J.R., Cuadros, J., Niles, P.B., Parnell, J., Rogers, A.D., Wright, S.P., 2013. Groundwater activity on Mars and implications for a deep biosphere. Nature Geoscience, 6, 133-138. Doi: 10.1038/ngeo1706

Michalski, J.R., Cuadros, J., Bishop, J.L., Darby Dyar, M., Dekov, V., Fiore, S., 2015. Constraints on the crystal-chemistry of Fe/Mg-rich smectitic clays on Mars and links to global alteration trends, Earth and Planetary Science Letters. doi:10.1016/j.epsl.2015.06.020

Moore, D.E., Rymer, M.J., 2007. Talc-bearing serpentinite and the creeping section of the San Andreas fault. Nature 448, 795–797.

Murchie, S., Arvidson, R., Bedini, P., Beisser, K., Bibring, J.-P., Bishop, J., Boldt, J., Cavender, P., Choo, T., Clancy, R.T., Darlington, E.H., Des Marais, D., Espiritu, R., Fort, D., Green, R., Guinness, E., Hayes, J., Hash, C., Heffernan, K., Hemmler, J., Heyler, G., Humm, D., Hutcheson, J., Izenberg, N., Lee, R., Lees, J., Lohr, D., Malaret, E., Martin, T., McGovern, J.A., McGuire, P., Morris, R., Mustard, J., Pelkey, S., Rhodes, E., Robinson, M., Roush, T., Schaefer, E., Seagrave, G., Seelos, F., Silverglate, P., Slavney, S., Smith, M., Shyong, W.J., Strohbehn, K., Taylor, H., Thompson, P., Tossman, B., Wirzburger, M., Wolff, M., 2007. Compact Connaissance Imaging Spectrometer for Mars (CRISM) on Mars Reconnaissance Orbiter (MRO). J. Geophys. Res. E Planets 112, E05S03. doi:10.1029/2006JE002682

Mustard, J.F. and Pieters, C.M., 1989. Photometric phase functions of common geologic minerals and applications to quantitative analysis of mineral mixture reflectance spectra. Journal of Geophysical Research, 94, B10, 13,619-13,634.

Mustard, J.F., Ehlmann, B.L., Murchie, S.L., Poulet, F., Mangold, N., Head, J.W., Bibring, J.P., Roach, L.H., 2009. Composition, morphology, and stratigraphy of Noachian crust around the Isidis basin. J. Geophys. Res. E Planets 114, 1–18. doi:10.1029/2009JE003349

Mustard, J.F., Poulet, F., Head, J.W., Mangold, N., Bibring, J.-P., Pelkey, S.M., Fassett, C.I., Langevin, Y., Neukum, G., 2007. Mineralogy of the Nili Fossae region with OMEGA/Mars Express data: 1.

Ancient impact melt in the Isidis Basin and implications for the transition from the Noachian to Hesperian. J. Geophys. Res. 112, E08S03. doi:10.1029/2006JE002834

Nealson, K.H., Inagaki, F., Takai, K., 2005. Hydrogen-driven subsurface lithoautotrophic microbial ecosystems (SLiMEs): do they exist and why should we care? Trends in Microbiology, 13, 9, doi: 10.1016/j.tim.2005.07.010.

O'Hanley, D.S., 1996. Serpentinites: Records of Tectonics and Petrological History. Oxford University Press, New York.

Ody, A., Poulet, F., Bibring, J.-P., Loizeau, D., Carter, J., Gondet, B., Langevin, Y., 2013. Global investigation of olivine on Mars: Insights into crust and mantle compositions. J. Geophys. Res. Planets 118, 234–262. doi:10.1029/2012JE004149

Palandri, J.L. and Reed, M.H., 2004. Geochemical models of metasomatism in ultramafic systems: serpentinization, rodingitization, and sea floor carbonate chimney precipitation. Geochim. Comochim. Acta.68, 1115-1133.

Pelkey, S.M., Mustard, J.F., Murchie, S., Clancy, R.T., Wolff, M., Smith, M., Milliken, R.E., Bibring, J.P., Gendrin, a., Poulet, F., Langevin, Y., Gondet, B., 2007. CRISM multispectral summary products: Parameterizing mineral diversity on Mars from reflectance. J. Geophys. Res. E Planets 112, 1–18. doi:10.1029/2006JE002831

Poulet, F., Bibring, J.-P., Mustard, J.F., Gendrin, a, Mangold, N., Langevin, Y., Arvidson, R.E., Gondet, B., Gomez, C., Berthé, M., Erard, S., Forni, O., Manaud, N., Poulleau, G., Soufflot, a, Combes, M., Drossart, P., Encrenaz, T., Fouchet, T., Melchiorri, R., Bellucci, G., Altieri, F., Formisano, V., Fonti, S., Capaccioni, F., Cerroni, P., Coradini, a, Korablev, O., Kottsov, V., Ignatiev, N., Titov, D., Zasova, L., Pinet, P., Schmitt, B., Sotin, C., Hauber, E., Hoffmann, H., Jaumann, R., Keller, U., Forget, F., 2005. Phyllosilicates on Mars and implications for early martian climate. Nature 438, 623–627. doi:10.1038/nature04274

Poulet, F., J. Carter, J. L. Bishop, D. Loizeau, and S. M. Murchie (2014) Mineral abundances at the final four curiosity study sites and implications for their formation. Icarus, 231, 65-76 10.1016/j.icarus.2013.11.023.

Proskurowski, G., Lilley, M.D., Kelley, D.S., Olson, E.J., 2006. Low temperature volatile production at the Lost City Hydrothermal Field, evidence from a hydrogen stable isotope geothermometer. Chem. Geol. 229, 331–343. doi:http://dx.doi.org/10.1016/j.chemgeo.2005.11.005

Proskurowski, G., Lilley, M.D., Seewald, J.S., Früh-Green, G.L., Olson, E.J., Lupton, J.E., Sylva, S.P., Kelley, D.S., 2008. Abiogenic hydrocarbon production at lost city hydrothermal field. Science 319, 604–607. doi:10.1126/science.1151194

Ramsey, M.S., Christensen, P.R., 1998. Mineral abundance determination: Quantitative deconvolution of thermal emission spectra. J. Geophys. Res. 103, 577. doi:10.1029/97JB02784

Rice, M.S., Cloutis, E. a., Bell, J.F., Bish, D.L., Horgan, B.H., Mertzman, S. a., Craig, M. a., Renaut, R.W., Gautason, B., Mountain, B., 2013. Reflectance spectra diversity of silica-rich materials: Sensitivity to environment and implications for detections on Mars. Icarus 223, 499–533. doi:10.1016/j.icarus.2012.09.021

Rinaudo, C., Gastaldi, D., Belluso, E., 2003. Characterization of Chyrsotile, antigorite, and lizardite by FT-Raman Spectroscopy. The Canadian Mineralogist, 41, 883-890

Rogers, A.D. and Bandfield, J.L., 2009. Mineralogical characterization of Mars Science Laboratory candidate landing sites from THEMIS and TES data. Icarus, 10.1016/j.icarus.2009.04.020

Rogers, A. D. and H. Nekvasil, 2015. Feldspathic rocks on Mars: Compositional constraints from infrared spectroscopy and possible formation mechanisms, Geophys Res Lett, 42(8), 2619-2626, doi: 10.1002/2015GL063501.

Rogers, A. D., Christensen, P.R., 2007. Surface mineralogy of Martian low-albedo regions from MGS-TES data: Implications for upper crustal evolution and surface alteration. J. Geophys. Res. E Planets 112, 1–18. doi:10.1029/2006JE002727

Rogers, A.D., Aharonson, O., 2008. Mineralogical composition of sands in Meridiani Planum determined from Mars Exploration Rover data and comparison to orbital measurements. J. Geophys. Res. Planets 113, E06S14. doi:10.1029/2007JE002995

Ruff, S.W., Christensen, P.R., Barbera, P.W., Anderson, D.L., 1997. Quantitative thermal emission spectroscopy of minerals: A laboratory technique for measurement and calibration. J. Geophys. Res. Solid Earth 102, 14899–14913. doi:10.1029/97JB00593

Ruff, S.W., Christensen, P.R., 2002. Bright and dark regions on Mars: Particle size and mineralogical characteristics based on Thermal Emission Spectrometer data. J. Geophys. Res. 107, 5127. doi:10.1029/2001JE001580

Ruff, S.W., Farmer, J.D., Calvin, W.M., Herkenhoff, K.E., Johnson, J.R., Morris, R. V., Rice, M.S., Arvidson, R.E., Bell, J.F., Christensen, P.R., Squyres, S.W., 2011. Characteristics, distribution, origin, and significance of opaline silica observed by the Spirit rover in Gusev crater, Mars. J. Geophys. Res. 116, E00F23. doi:10.1029/2010JE003767

Russell, M.J., and Martin, W., 2004. The rocky roots of the acetyl-CoA pathway, TRENDS in Biochemical Sciences, 29, 7, doi: 10.1016/j.tibs.2004.05.007.

Russell, M.J., Hall, A.J., Martin, W., 2010. Serpentinization as a source of energy at the origin of life. Geobiology 8, 355–371. doi:10.1111/j.1472-4669.2010.00249.x

Russell, M.J., Barge, L.M., Bhartia, R., Bocanegra, D., Bracher, P.J., Branscomb, E., Kidd, R., Mcglynn, S., Meier, D.H., Nitschke, W., Shibuya, T., Vance, S., White, L., Kanik, I., 2014. The Drive to Life on Wet and Icy Worlds. Astrobiology 14, 308–343. doi:10.1089/ast.2013.1110

Saper, L., Mustard, J.F., 2013. Extensive linear ridge networks in Nili Fossae and Nilosyrtis, Mars: Implications for fluid flow in the ancient crust. Geophys. Res. Lett. 40, 245–249. doi:10.1002/grl.50106

Schrenk, M.O., Kelley, D.S., Bolton, S.A., Baross, J.A., 2004. Low archael diversity linked to subseafloor geochemical processes at the Lost City Hydrothermal Field, Mid-Atlantic Ridge. Environmental Microbiology. 6(10), 1086-1095. doi:10.1111/j/1462-2920.2004.00650.x

Schulte, M., Blake, D., Hoehler, T., McCollom, T., 2006. Serpentinization and Its Implications for Life on the Early Earth and Mars 6, 364–376.

Schultz, R.A., Frey, H.V., 1990. A new survey of multiring impact basins on Mars. J. Geophys. Res. 95, 14,175–14,189. doi:10.1029/JB095iB09p14175

Smith, M.R., Bandfield, J.L., 2012. Geology of quartz and hydrated silica-bearing deposits near Antoniadi Crater, Mars. J. Geophys. Res. 117, 1–24. doi:10.1029/2011JE004038

Smith, M.R., Bandfield, J.L., Cloutis, E. a., Rice, M.S., 2013. Hydrated silica on Mars: Combined analysis with near-infrared and thermal-infrared spectroscopy. Icarus 223, 633–648. doi:10.1016/j.icarus.2013.01.024

Sojo, V., Herschy, B., Whicher, A., Camprubi, E., Lane, N., 2016. Review Article. Astrobiology 16, 181–197. doi:10.1089/ast.2015.1406

Stueken, E.E., Anderson, R.E., Bowman, J.S., Brazelton, W.J., Colangelo-Lillis, J., Goldman, A.D., Som, S.M., Baross, J.A., 2013. Did life originate from a global chemical reactor ? Geobiology 11, 101–126. doi:10.1111/gbi.12025

Thomas, N.H. and J.L. Bandfield, 2013. Identification of spectral endmembers in CRISM data using factor analysis and target transformation. 44th Lunar and Planetary Science Conference, Abs#1325.

Thomas, N.H. and J.L. Bandfield, 2016. Identification and refinement of martian surface mineralogy using factor analysis and target transformation of near-infrared spectroscopic data, Icarus, in revision.

Thomas, N.H., Bandfield, J.L., and E.S. Amador, 2014. Identification and characterization of martian serpentine using target transformation and CRISM data. 45th Lunar and Planetary Science Conference, Abs#1909.

Thomson, J.L., Salisbury, J.W., 1993. The mid-infrared reflectance of mineral mixtures (7-14 microns). Remote Sens. Environ. 45, 1–13. doi:10.1016/0034-4257(93)90077-B

Tornabene, L.L., Moersch, J.E., McSween, H.Y., Hamilton, V.E., Piatek, J.L., Christensen, P.R., 2008. Surface and crater-exposed lithologic units of the Isidis based as mapped by coanalysis of

THEMIS and TES derived data products. J. Geophys. Res. E Planets 113, 1–30. doi:10.1029/2007JE002988

Tosca, N.J., Knoll, A.H., 2009. Juvenile chemical sediments and the long term persistence of water at the surface of Mars. Earth Planet. Sci. Lett. 286, 379–386. doi:10.1016/j.epsl.2009.07.004

Vance, S., Harnmeijer, J., Kimura, J.U.N., Hussmann, H., Demartin, B., Brown, J.M., Al, V.E.T., 2007. Research Paper. Astrobiology 7. doi:10.1089/ast.2007.0075

Vincent, R.K., Thomson, F., 1972. Spectral compositional imaging of silicate rocks. J. Geophys. Res. 77, 2465–2472. doi:10.1029/JB077i014p02465

Viviano-Beck, C.E., Seelos, F.P., Murchie, S.L., Kahn, E.G., Seelos, K.D., Morgan, M.F., 2014. Revised CRISM spectral parameters and summary products based on the currently detected mineral diversity on Mars. J. Geophys. Res. Planets 119, 1403–1431. doi:10.1002/2014JE004627.Received

Viviano-Beck, C.E., S.L. Murchie, A.W. Beck, J.M. Dohm., 2017. Compositional and structural constraints on the geologic history of eastern Tharsis Rise, Mars. Icarus, 284, 43-58, doi: 10.1016/j.icarus.2016.09.005

Viviano, C.E., Moersch, J.E., McSween, H.Y., 2013. Implications for early hydrothermal environments on Mars through the spectral evidence for carbonation and chloritization reactions in the Nili Fossae region. J. Geophys. Res. Planets 118, 1858–1872. doi:10.1002/jgre.20141

Walter, L.S., Salisbury, J.W., 1989. Spectral Characterization of Igneous Rocks in the 8- to 12- micron Region. J. Geophys. Res. 94, 9203–9213.

Wichman, R.W., Schultz, P.H., 1989. Sequence and Mechanisms of Deformation Around the Hellas and Isidis Impact Basins on Mars. J. Geophys. Res. 94, 17, 333–17,357.

Williams, K.B., Sonzogni, Y., Treiman, A.H., 2014. Amphibole in the Tissant Martian Meteorite: Composition and Implication for Volatile Content of Parental Magma. 45th Lunar and Planetary Science Conference, Abs #1435.

Wray, J.J., Ehlmann, B.L., Squyres, S.W., Mustard, J.F., Kirk, R.L., 2008. Compositional stratigraphy of clay-bearing layered deposits at Mawrth Vallis, Mars. Geophysical Research Letters, 35, L12202.

Wray, J. J., S. T. Hansen, J. Dufek, G. A. Swayze, S. L. Murchie, F. P. Seelos, J. R. Skok, R. P. Irwin Iii, and M. S. Ghiorso (2013), Prolonged magmatic activity on Mars inferred from the detection of felsic rocks, Nature Geosci, 6(12), 1013-1017, doi: 10.1038/ngeo1994.

Wray, J.J., Murchie, S.L., Bishop, J.L., Ehlmann, B.L., Milliken, R.E., Wilhelm, M.B., Seelos, K.D., Chojnacki, M., 2016. Orbital evidence for more widespread carbonate-bearing rocks on Mars. Journal of Geophysical Research: Planets, 121, 652-677. Doi:10.1002/2015JE004972

SUPPLEMENTARY MATERIAL

Table 5.8. Initial THEMIS Day IR DCS 8-7-5 images visually inspected for compositional variability and Purple

THEMIS Product ID
I01283009
I01308005
I01308005
I01595009
I01645007
I01770008
I01982006
I01982006
I02007009
I02032005
I02057002
I02319008
I02344005
I02519006
I02681006
I02756002
I03430002
I04566009
I05727011
I09609022
I10283010
I11094006
I11743007
I13278010
I13303004
I13565008
I13927007
I17908015
I18195011
I18457007
I18532009
I18769007
I19106013
I19755006
I27043033
I28216011
I28478006
I28528002
I35390009
I35677010
I35964015
I35989015
I36226026
I36251026
I36276032
I36301013
I36326013
I36351028
I36426026
I36538025
I36613020
I36688013
I36925042
I37237015
I37499019
I37549006
I37786007
I38360010
I39296009
I39533002
I39608004
I43901003
I44263002
I44288005
I44413003
I44750003
I45087012
I45137009
I45499019
I45549047
I45811018
I45861011
I46173009
I46223006
I47484014
I47796006
I47896005
I48208013
I52029004
I52054004
I01570009
I01857006
I01932008
I02194005
I02244005
I02394009
I02444002
I02469002
I02494006
I02631005
I02706002
I02731002
I02781003
I03505002
I03555002
I04491005
I04741008
I05215009
I05490020
I05515022
I05827010
I07974020
I08798006
I10158009
I10258011
I10308046
I10470015
I10645014
I11668005
I11843005
I12467007
I12492006
I12679004
I13253008
I13690011
I17072009
I17471015
I17783020
I17808018
I18095022
I18145014
I18220006
I18270012
I18295015
I18320008
I18357015
I18432016
I18607041
I18744008
I18919007
I19006009
I19031010
I19056011
I19081013
I19181014
I19206009
I19543016
I19830005
I22251040
I26057010
I26606030
I26631016
I26831012
I27018033
I27093046
I33468008
I35240010
I35602005
I35727009
I35752006
I35777009
I35802012
I35864010
I35889015
I35914015
I35939015
I36014018
I36039022
I36064012
I36089015
I36114022
I36151021
I36176021
I36201025
I36376029
I36401029
I36488026
I36513026
I36638042
I36713013
I36775013
I36800017
I36875018
I36900022
I37062019
I37087020
I37112002
I37187009
I37262020
I37287050
I37349016
I37374015
I37524007
I37811010
I37861031
I38173010
I38410010
I38460008
I38485006
I38622040
I38909007
I38934013
I39009007
I43876003
I44001007
I44026005
I44238003
I44500002
I44600002
I44675009
I44725002
I44912007
I45012009
I45112007
I45374016
I45424044
I45686010
I45836007
I45886016
I45911007

I45936008
I46011010
I46298007
I46348016
I46373018
I46435017
I46872007
I47097024
I47646011
I47821006
I47871005
I51292006
I52491007
I52741007
I52853010
I52903017
I52978009
I53003013
I53153006
I53540006

Table 5.9. Down-selected high quality THEMIS images with Purple and Yellow/Amber Units in regional proximity. These THEMIS images were atmospherically correct and used for all further TIR analyses.

THEMIS Image ID
I01308005
I01595009
I01982006
I02007009
I02319008
I02681006
I02731002
I03430002
I09609022
I18532009
I35390009
I36613020
I39296009
I39533002
I39608004
I44288005
I47484014

Table 5.10. THEMIS line and sample numbers used for spectra in **Figure 2.6**.

THEMIS ID	Spectral Type	X-axis Pixel Numbers	Y-axis Pixel Numbers	Bands
I36613020	Typical terrain	41-44	413-416	3-9
I36613020	Amber	106-107	523-526	3-9
I36613020	Yellow	141-148	838-848	3-9
I36613020	Purple	123-131	516-525	3-9
I36613020	Phyllosilicate-bearing (typical terrain)	52-58	409-415	3-9
I35390009	Fuchsia/Orange	161-216	1086-1113	3-9

Table 5.11. CRISM Multispectral Product images (IDs listed below) were visually inspected for 8 phase and/or hydration index maps. A qualitative and subjective characterization of “yes” or “no” was assigned to each index if high index values were, or were not, present in a structurally coherent formation.

CRISM Product ID	OLINDEX	BD1900	BD2100	SINDEX	BD2210	BD2250	D2300	BD2500
0000366C_01	yes	yes	no	no	no	no	yes	no
000037E8_03	yes	no	no	no	no	no	no	no
0000397F_05	yes	yes	no	no	no	no	yes	no
00004FD2_01	yes	no	no	no	no	no	no	no
000052D4_01	yes	no	no	no	no	no	no	no
000058B0_01	yes	yes	no	no	no	no	yes	no
00005AC1_01	yes	no	no	no	no	no	no	no
000062D3_01	yes	yes	no	no	no	no	yes	no
000070A8_05*	x	x	x	x	x	x	x	x
00007526_07	yes	yes	no	no	no	no	yes	no
00007C18_01	yes	yes	no	no	no	no	yes	no
000080AF_03	yes	no	no	no	no	no	no	no
0000902D_01	yes	yes	no	no	no	no	yes	no
0000C752_01	yes	yes	no	no	no	no	yes	no
000106BC_03	yes	yes	no	no	no	no	yes	no
00012518_01	no	no	no	no	no	no	no	no
00013755_01	yes	yes	no	no	no	no	yes	no
00014007_01	yes	yes	no	no	no	no	yes	no
00015218_01	yes	no	no	no	no	no	no	no
0001582D_05	yes	yes	no	no	no	no	yes	no
0001969A_01	yes	no	no	no	no	no	no	no
0001A9F9_01	yes	yes	no	no	no	no	yes	no
0001ACED_01	yes	yes	no	no	no	no	yes	no
00026F8F_01	no	no	no	no	no	no	no	no

*Dusty or noisy image

Table 5.12. CRISM Multispectral Image IDS used in **Figure 2.7**. Images were cropped between 19.0 and 25.0 ºN.

CRISM Product ID
MSP00002F1D_01_IF214L_TRR3
MSP00002F1D_03_IF214L_TRR3
MSP0000366C_01_IF214L_TRR3
MSP000036A9_03_IF214L_TRR3
MSP000037E8_03_IF214L_TRR3
MSP0000397F_05_IF214L_TRR3
MSP00003F2C_03_IF214L_TRR3
MSP00004FD1_07_IF214L_TRR3
MSP00004FD2_01_IF214L_TRR3
MSP0000516B_01_IF214L_TRR3
MSP000052D4_01_IF214L_TRR3
MSP000056D8_01_IF214L_TRR3
MSP000058AF_07_IF214L_TRR3
MSP000058B0_01_IF214L_TRR3
MSP00005AC1_01_IF214L_TRR3
MSP000062D3_01_IF214L_TRR3
MSP000062D3_03_IF214L_TRR3
MSP00006DD9_07_IF214L_TRR3
MSP000070A8_05_IF214L_TRR3
MSP000070A8_07_IF214L_TRR3
MSP00007526_07_IF214L_TRR3
MSP00007A27_05_IF214L_TRR3
MSP00007A27_07_IF214L_TRR3
MSP00007C18_01_IF214L_TRR3
MSP000080AF_03_IF214L_TRR3
MSP00008DEE_01_IF214L_TRR3
MSP00008E3E_01_IF214L_TRR3
MSP0000902D_01_IF214L_TRR3
MSP0000941C_01_IF214L_TRR3
MSP0000B32F_01_IF214L_TRR3
MSP0000B5AC_01_IF214L_TRR3
MSP0000C752_01_IF214L_TRR3
MSP0000CD24_01_IF211L_TRR3
MSP0000CE39_01_IF211L_TRR3
MSP0001028C_05_IF214L_TRR3
MSP000106BC_03_IF214L_TRR3
MSP00010AB0_01_IF214L_TRR3
MSP0001138D_01_IF214L_TRR3
MSP0001185D_01_IF214L_TRR3
MSP0001185D_03_IF214L_TRR3
MSP00012F58_01_IF214L_TRR3
MSP00013755_01_IF214L_TRR3
MSP0001396B_01_IF214L_TRR3
MSP0001396C_01_IF214L_TRR3
MSP00014007_01_IF214L_TRR3
MSP0001423B_03_IF214L_TRR3
MSP0001423B_05_IF214L_TRR3
MSP000148C2_01_IF214L_TRR3
MSP00014DA9_01_IF214L_TRR3
MSP00015218_01_IF214L_TRR3
MSP0001582D_05_IF214L_TRR3
MSP0001BA1F_01_IF214L_TRR3
MSP0001C6C5_01_IF213L_TRR3
MSP0001C6C6_01_IF213L_TRR3
MSP0001DE75_01_IF214L_TRR3
MSP00026F8F_01_IF213L_TRR3
MSP000271E3_01_IF211L_TRR3

Table 5.13. CRISM MSP sample and line numbers for spectra used in **Figure 2.9**

Location/Spectral Type	CRISM ID	Numerator (Target) Pixels	Denominator (null/known) Pixels	Bands
Olivine-rich Basalt	MSP0000366C_01	X: 58-61 Y:1023-1027	X: 58-61 Y: 988-992	5:
Phyllosilicate-bearing	MSP0000366C_01	X: 53-55 Y:1068-1073	X: 53-55 Y: 966-972	5:
Fuchsia/Orange	MSP000037E8_03	X: 25-37 Y: 1901- 1918	X:25-37 Y: 1754-1771	5:

Table 5.14. CRISM MSP sample and line numbers used for Yellow/Amber Unit spectrum in **Figure 2.9**.

CRISM ID	Numerator (Target) Pixels	Denominator (null/known) Pixels	Bands
MSP0000366C_01	X: 54-55 Y: 1032-1033	X: 54-55 Y: 1012-1013	5:
MSP0000366C_01	X: 54-55 Y: 1032-1033	X: 54-55 Y: 197-978	5:
MSP0000366C_01	X: 53-54 Y: 1034-1035	X: 53-54 Y:1012-1013	5:
MSP0000366C_01	X: 55-57 Y: 1033-1036	X: 55-57 Y: 981-984	5:
MSP0000366C_01	X: 56-58 Y: 1035-1036	X: 56-58 Y: 973-975	5:
MSP0000366C_01	X: 55-56 Y: 1035-1037	X: 55-56 Y: 973-975	5:
MSP0000366C_01	X: 34-35 Y: 1117-1118	X: 34-35 Y: 1147-1148	5:
MSP0000366C_01	X: 6-7 Y: 1114-1115	X: 6-7 Y: 1142-1143	5:

Table 5.15. Spectral end-member library used for thermal-infrared deconvolution modeling. Unless otherwise noted, spectra come from the ASU Spectral Library, speclib.asu.edu)

Mineral Group	Mineral Name	Mineral ID
Serpentine	Antigorite	HS-8.4B
	Antigorite	BUR-1690
	Antigorite	NMNH96917*
	Chrysotile	JB-528**
	Lizardite	ECL-SRP109
	Lizardite	NMNHR4687.b*
Phyllosilicate	Chlorite	WAR-1924
	Illite	Imt-1
	Montmorillonite	Swy-1
	Nontronite	Nau-1
	Saponite	Eb-1
	Saponite	MINUN-29
	Talc	BUR-4640C
Feldspar	Andesine	BUR-240
	Albite	WAR-0612
	Labradorite	WAR-4524
	Perthite	WAR-5802
	Bytownite	WAR-1384
	Labradorite	WAR-RGAND01
	Labradorite	BUR-3080A
	Anorthite	WAR-5759

Mineral Group	Mineral Name	Mineral ID
	Oligoclase	WAR-0234
	Microcline	BUR-3460
	Anorthoclase	WAR-0579
	Orthoclase	WAR-RGSAN01
Amphibole	Mg-Hornblende	HS-315.4B
	Anthophyllite	BUR-4760
	Actinolite	HS-116.4B
	Fe-Hornblende	HS-326.4B
	Hornblende	BUR-2660
	Tremolite	WAR-0979
	Hornblende	NMNH-R7208
	Glaucophane	WAR-0219
Carbonate	Calcite	ML-C9
	Aragonite	C11
	Dolomite	C20
	Magnesite	C60
	Siderite	C62
	Calcite	C2
	Dolomite	C17
Pyroxene	Spodumene	HS-210.4B
Pyroxenoid	Wollastonite	WAR-8884
	Pyroxmangite	WAR-6894
Orthopyroxene	Bronzite	BUR-1920

Mineral Group	Mineral Name	Mineral ID
	Enstatite	HS-9.4B
Clinopyroxene	Diopside	HS-15.4B
	Augite	HS-119.4B
	Augite	BUR-620
	Hedenbergite	NMNH-R11524
	Diopside	BUR-1820
Phosphate	Apatite	ML-P1
	Meta-Variscite	ML-P8
	Pyromorphite	ML-P6
	Turquoise	ML-P5
	Pyromorphite	ML-P3
Olivine	Forsterite	BUR-3720A
	Fayalite	WAR-RGFAY01
Mica	Muscovite	WAR-5474
	Biotite	BUR-840
	Phlogopite	HS-23.3B
Epidote	Epidote	BUR-1940
Iron Oxide	Hematite	BUR-2600
	Hematite	GTSH4-300
	Goethite	GTS4
	Magnetite	WAR-0384
	Ilmenite	WAR-4119
Quartz	Quartz	BUR-4120

Mineral Group	Mineral Name	Mineral ID
	Chert	56
Sulfate	Gypsum	ML-S5
	Barite	ML-S1
	Selenite	ML-S8
Garnet	Almandine	BUR-120A
	Pyrope	WAR-5850
Hydrous Carbonate	Malachite	C13
	Azurite	C14
Al-Silicate	Kyanite	WAR-4482
	Andalusite	WAR-0482
	Sillimanite	WAR-7362
Opal	Opal-CT	02-031
Hydroxide	Brucite	RAN-45

*Clark et al., 2007

**CRISM Library "CHRYSOTILE W15 FROM D. DYAR COLLECTION, SEEO_HANLEY & DYAR 1998, ASBESTOS FIBERS", Bishop et al., 2002B

Table 5.16. CRISM images taken after 2011, these images were not looked at by previous studies and were searched for this study.

HRS00024571_07_IF175L_TRR3
HRS0001EC8F_07_IF174L_TRR3
HRS0001EBA1_07_IF174L_TRR3
HRS0001E23E_07_IF175L_TRR3
HRL0002422E_07_IF182L_TRR3
HRL00024023_07_IF183L_TRR3
HRL00020BA3_07_IF183L_TRR3
HRL0001FC92_07_IF182L_TRR3
HRL0001E20D_07_IF183L_TRR3
HRL0001D976_07_IF183L_TRR3
HRL0001D93D_07_IF182L_TRR3
FRT000251C0_07_IF165L_TRR3
FRT00024C1A_07_IF165L_TRR3
FRT00024A87_07_IF165L_TRR3
FRT000246CF_07_IF166L_TRR3
FRT00023728_07_IF166L_TRR3
FRT00023565_07_IF166L_TRR3
FRT00021F08_07_IF165L_TRR3
FRT00021DA6_07_IF166L_TRR3
FRT00021C5A_07_IF166L_TRR3
FRT00020C77_07_IF166L_TRR3
FRT000203DE_07_IF165L_TRR3
FRT0001FD76_07_IF166L_TRR3
FRT0001FB74_07_IF166L_TRR3
FRT0001ECBA_07_IF166L_TRR3
FRS00039936_01_IF168L_TRR3
FRS00038CD4_01_IF168L_TRR3
FRS00038C02_01_IF168L_TRR3
FRS00038BC9_01_IF168L_TRR3
FRS00037F03_01_IF168L_TRR3
FRS00037D63_01_IF168L_TRR3
FRS00036666_01_IF168L_TRR3
FRS00036634_01_IF169L_TRR3
FRS000364CA_01_IF168L_TRR3
FRS000355D1_01_IF168L_TRR3
FRS000328A0_01_IF168L_TRR3
FRS00032837_01_IF166L_TRR3
FRS0003166F_01_IF168L_TRR3
FRS0003161E_01_IF168L_TRR3
FRS0003161D_01_IF169L_TRR3
FRS00031442_01_IF168L_TRR3
FRS00031260_01_IF168L_TRR3
FRS00031204_01_IF168L_TRR3
FRS00030232_01_IF168L_TRR3
FRS000301CF_01_IF168L_TRR3
FRS0002FE75_01_IF168L_TRR3
FRS0002FE20_01_IF168L_TRR3
FRS0002F056_01_IF168L_TRR3
FRS0002EE3C_01_IF168L_TRR3
FRS0002EC89_01_IF168L_TRR3
FRS0002DE3A_01_IF168L_TRR3
FRS0002DC3A_01_IF168L_TRR3
FRS0002DA94_01_IF168L_TRR3
FRS0002DA46_01_IF168L_TRR3
FRS0002CABF_01_IF168L_TRR3
FRS0002C92B_01_IF168L_TRR3
FRS0002C8E9_01_IF168L_TRR3
FRS0002BB98_01_IF168L_TRR3
FRS0002BA97_01_IF168L_TRR3
FRS0002B58A_01_IF168L_TRR3
FRS0002B44A_01_IF168L_TRR3
FRS0002B2F2_01_IF168L_TRR3
FRS0002AF61_01_IF168L_TRR3
FRS0002AE17_01_IF168L_TRR3
FRS0002ADC4_01_IF168L_TRR3
FRS0002AC52_01_IF168L_TRR3
FRS0002A9B2_01_IF168L_TRR3
FRS00029FDB_01_IF168L_TRR3
FRS00029EEC_01_IF168L_TRR3
FRS00029EA8_01_IF168L_TRR3
FRS00029DA6_01_IF168L_TRR3
FRS00028DFB_01_IF168L_TRR3
FRS0002842A_01_IF168L_TRR3
FRS00028280_01_IF168L_TRR3
FRS000281D1_01_IF168L_TRR3
FRS0002762C_01_IF168L_TRR3
FRS0002753B_01_IF168L_TRR3
FRS00027508_01_IF169L_TRR3
FRS000273E6_01_IF168L_TRR3
FRS000272AC_01_IF168L_TRR3

Table 5.17. Thermal-infrared deconvolution model results for the non-carbonate rocks used for this study. Rows highlighted in green indicate abundances well within the detection limits for this study. Rows highlighted in red fall within known limits of the technique and can be noted but should not be used quantitatively.

"Talc -rich Fault Rock"	*Pyllosilicates excluding Serpentine	
Endmember	**Group**	**Normalized Abundance (%)**
Talc	Phyllosilicate*	41.87
Saponite	Phyllosilicate*	20.64
Chrysotile	Serpentine	6.98
Goethite-derived Hematite	Iron Oxide	6.9
Antigorite	Serpentine	6.08
Serp ECL (Lizardite)	Serpentine	5.98
Biotite	Phyllosilicate*	3.41
Hornblende	Amphibole	3.36
Wollastonite	Pyroxenoid	1.54
Opal-CT	Opal	1.22
Azurite	Hydrous carbonate	0.9
Malachite	Hydrous carbonate	0.82
Actinolite	Amphibole	0.21
Kyanite	Al-silicate	0.08
"Gabbro"		
Endmember	**Group**	**Normalized Abundance (%)**
Labradorite	Feldspar	24.44
Tremolite	Amphibole	17.27
Hornblende	Amphibole	11.01
Chrysotile	Serpentine	7.22
Gypsum	Sulfate	6.9
Goethite	Iron Oxide	6.03
Anthophyllite	Amphibole	5.43
Pyromorphite	Phosphate	3.82
Calcite	Carbonate	3.57
Magnesiohornblende	Amphibole	3.48
Barite	Sulfate	2.56
Forsterite	Olivine	2.29
Anorthite	Feldspar	1.95
Quartz	Quartz	1.67
Wollastonite	Pyroxenoid	1.64
Epidote	Epidote	0.27
Aragonite	Carbonate	0.26
Enstatite	Orthopyroxene	0.18

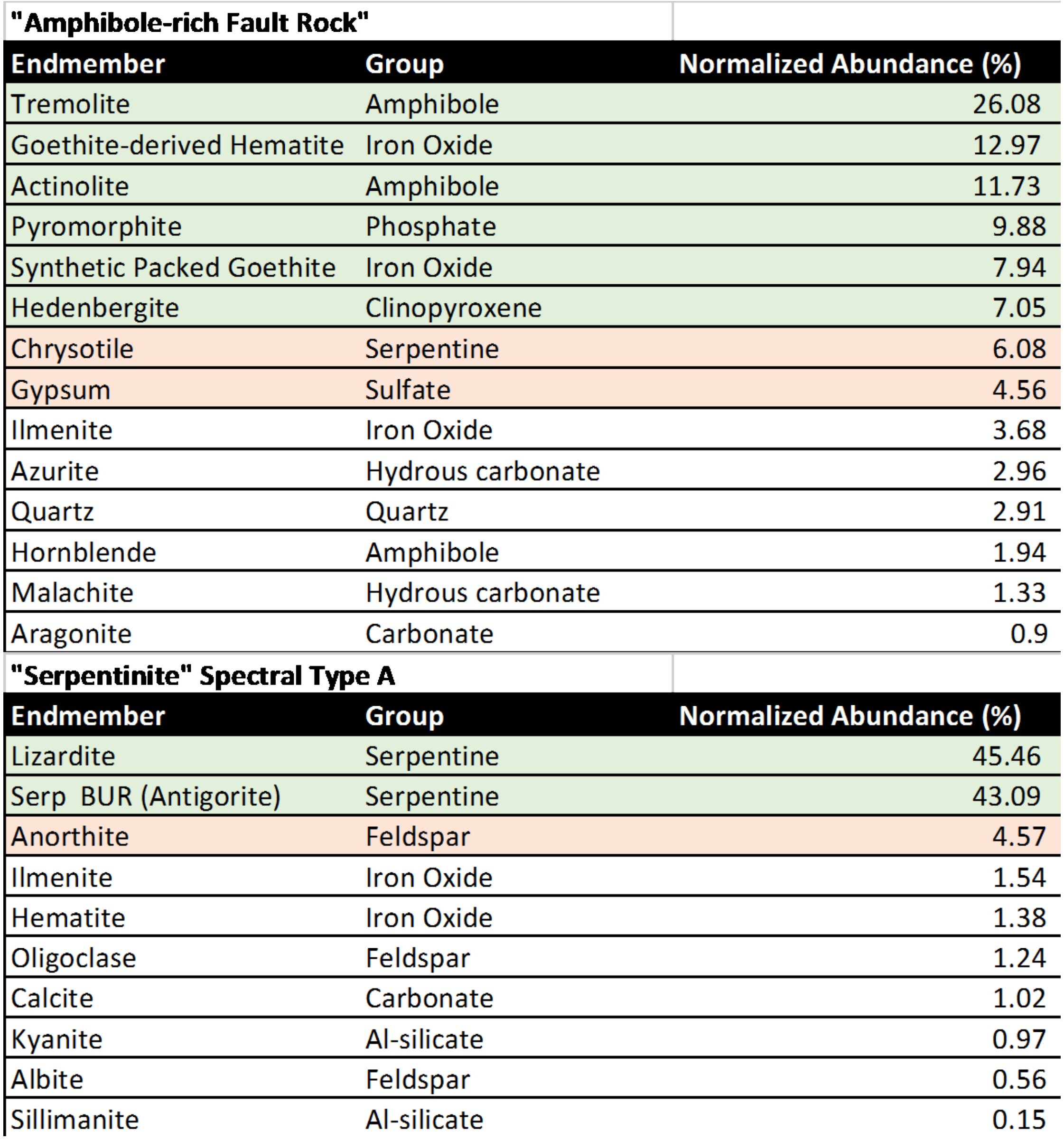

"Amphibole-rich Fault Rock"

Endmember	Group	Normalized Abundance (%)
Tremolite	Amphibole	26.08
Goethite-derived Hematite	Iron Oxide	12.97
Actinolite	Amphibole	11.73
Pyromorphite	Phosphate	9.88
Synthetic Packed Goethite	Iron Oxide	7.94
Hedenbergite	Clinopyroxene	7.05
Chrysotile	Serpentine	6.08
Gypsum	Sulfate	4.56
Ilmenite	Iron Oxide	3.68
Azurite	Hydrous carbonate	2.96
Quartz	Quartz	2.91
Hornblende	Amphibole	1.94
Malachite	Hydrous carbonate	1.33
Aragonite	Carbonate	0.9

"Serpentinite" Spectral Type A

Endmember	Group	Normalized Abundance (%)
Lizardite	Serpentine	45.46
Serp BUR (Antigorite)	Serpentine	43.09
Anorthite	Feldspar	4.57
Ilmenite	Iron Oxide	1.54
Hematite	Iron Oxide	1.38
Oligoclase	Feldspar	1.24
Calcite	Carbonate	1.02
Kyanite	Al-silicate	0.97
Albite	Feldspar	0.56
Sillimanite	Al-silicate	0.15

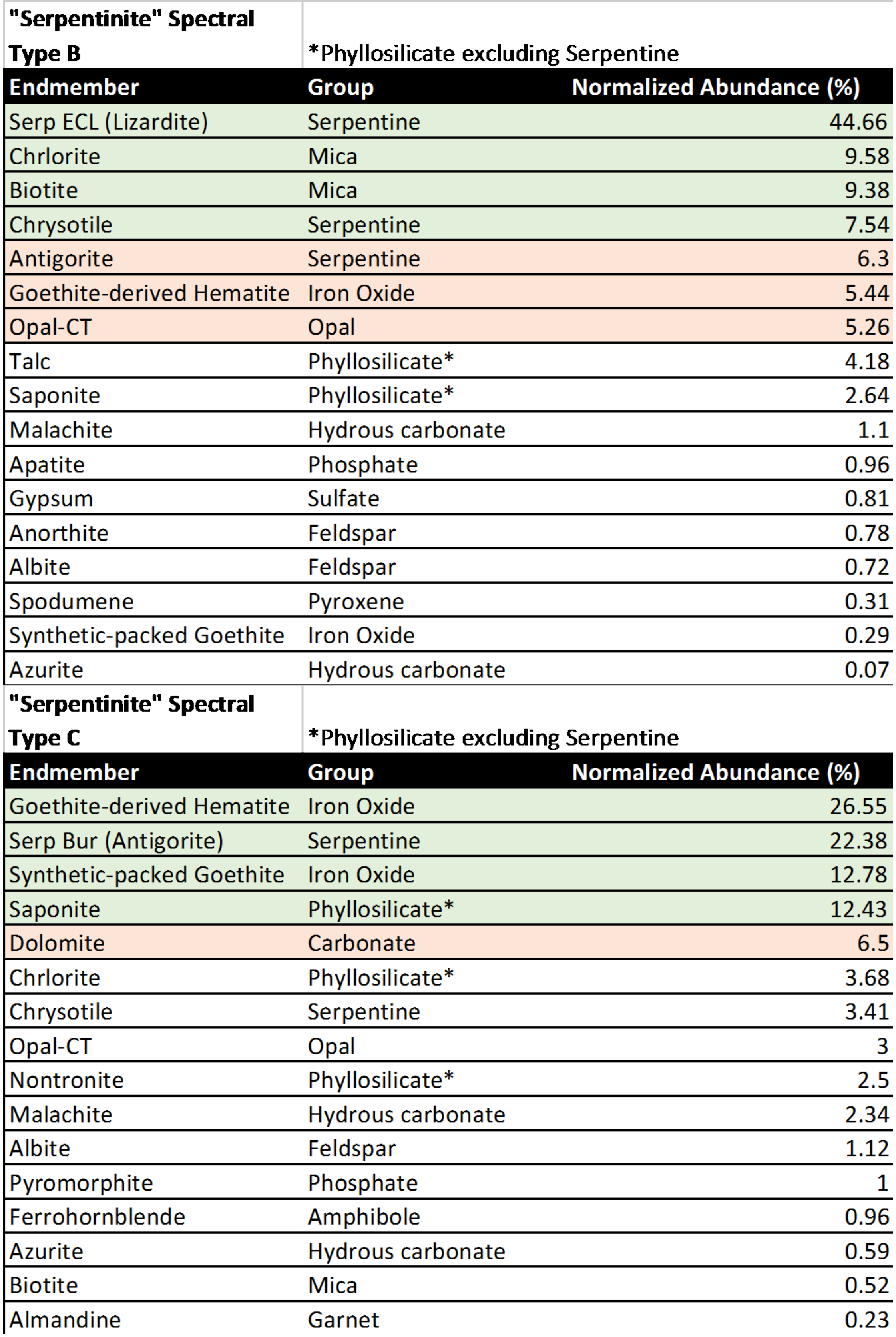

"Serpentinite" Spectral Type B

*Phyllosilicate excluding Serpentine

Endmember	Group	Normalized Abundance (%)
Serp ECL (Lizardite)	Serpentine	44.66
Chrlorite	Mica	9.58
Biotite	Mica	9.38
Chrysotile	Serpentine	7.54
Antigorite	Serpentine	6.3
Goethite-derived Hematite	Iron Oxide	5.44
Opal-CT	Opal	5.26
Talc	Phyllosilicate*	4.18
Saponite	Phyllosilicate*	2.64
Malachite	Hydrous carbonate	1.1
Apatite	Phosphate	0.96
Gypsum	Sulfate	0.81
Anorthite	Feldspar	0.78
Albite	Feldspar	0.72
Spodumene	Pyroxene	0.31
Synthetic-packed Goethite	Iron Oxide	0.29
Azurite	Hydrous carbonate	0.07

"Serpentinite" Spectral Type C

*Phyllosilicate excluding Serpentine

Endmember	Group	Normalized Abundance (%)
Goethite-derived Hematite	Iron Oxide	26.55
Serp Bur (Antigorite)	Serpentine	22.38
Synthetic-packed Goethite	Iron Oxide	12.78
Saponite	Phyllosilicate*	12.43
Dolomite	Carbonate	6.5
Chrlorite	Phyllosilicate*	3.68
Chrysotile	Serpentine	3.41
Opal-CT	Opal	3
Nontronite	Phyllosilicate*	2.5
Malachite	Hydrous carbonate	2.34
Albite	Feldspar	1.12
Pyromorphite	Phosphate	1
Ferrohornblende	Amphibole	0.96
Azurite	Hydrous carbonate	0.59
Biotite	Mica	0.52
Almandine	Garnet	0.23

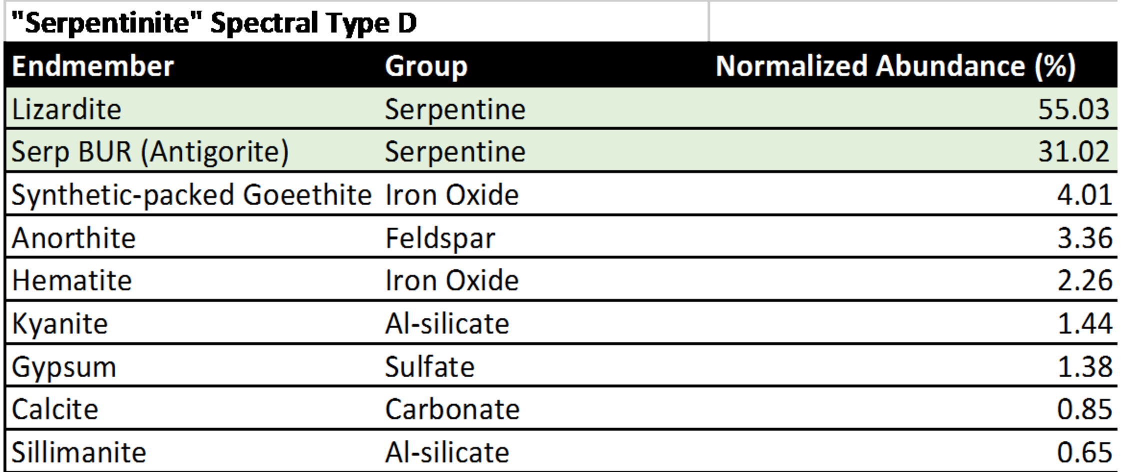

"Serpentinite" Spectral Type D

Endmember	Group	Normalized Abundance (%)
Lizardite	Serpentine	55.03
Serp BUR (Antigorite)	Serpentine	31.02
Synthetic-packed Goeethite	Iron Oxide	4.01
Anorthite	Feldspar	3.36
Hematite	Iron Oxide	2.26
Kyanite	Al-silicate	1.44
Gypsum	Sulfate	1.38
Calcite	Carbonate	0.85
Sillimanite	Al-silicate	0.65

"Serpentinite" Spectral Type E

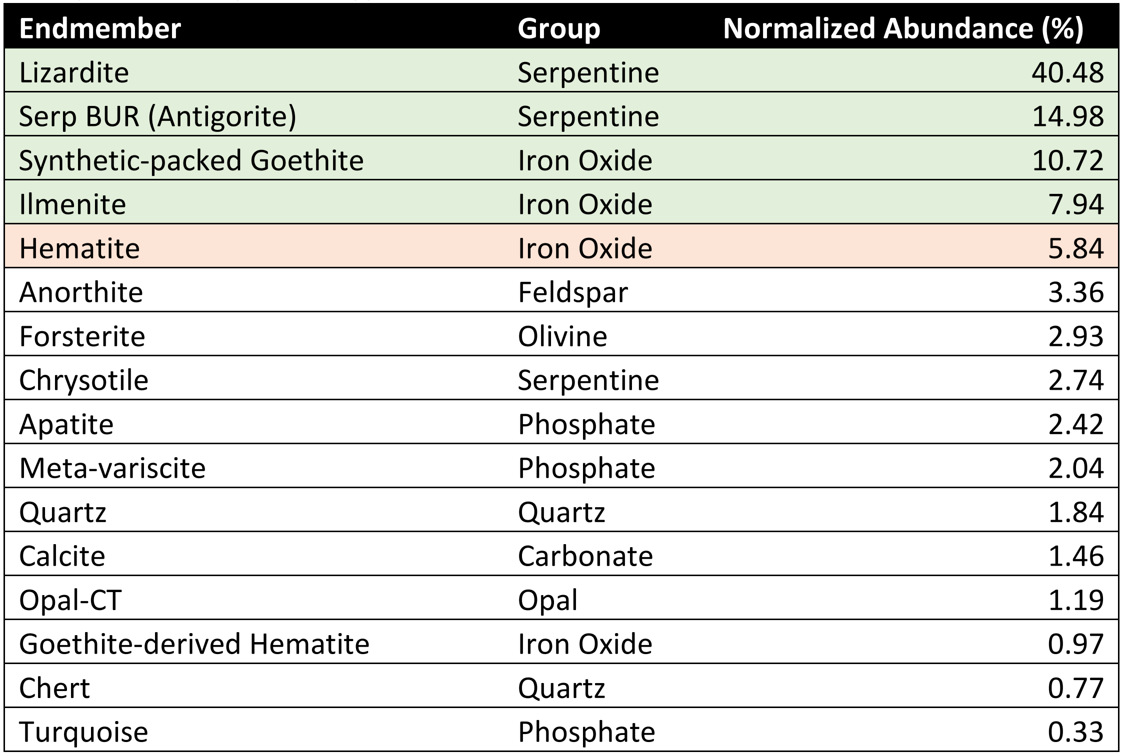

Endmember	Group	Normalized Abundance (%)
Lizardite	Serpentine	40.48
Serp BUR (Antigorite)	Serpentine	14.98
Synthetic-packed Goethite	Iron Oxide	10.72
Ilmenite	Iron Oxide	7.94
Hematite	Iron Oxide	5.84
Anorthite	Feldspar	3.36
Forsterite	Olivine	2.93
Chrysotile	Serpentine	2.74
Apatite	Phosphate	2.42
Meta-variscite	Phosphate	2.04
Quartz	Quartz	1.84
Calcite	Carbonate	1.46
Opal-CT	Opal	1.19
Goethite-derived Hematite	Iron Oxide	0.97
Chert	Quartz	0.77
Turquoise	Phosphate	0.33

Table 5.18. New CRISM detections of Mg-carbonate, Talc and/or saponite, and serpentine in Nili Fossae from this study. Images correspond to stamps mapped in **Figure 3.8**.

New Mg-Carbonate Detections	New Talc/Saponite Detections	New Serpentine Detections
FRT00003F75_07	FRT00023728_07	FRS0002AE17_01
FRT0000527D_07	FRS0002AE17_01	
FRT00005A3E_07	FRS00027639_01	
FRT000067E1_07	FRS0003161D_01	
FRT000069CA_07	FRS00036666_01	
FRT0000722C_07		
FRT00007D61_07		
FRT00008530_07		
FRT00009971_07		
FRT0000B1B5_07		
FRT0000BEEB_07		
FRT0000C62B_07		
FRT0000C968_07		
FRT000107A7_07		
FRT0001182A_07		
FRT00012149_07		
FRT000161EF_07		
FRT000165F7_07		
FRT00016A73_07		
FRT00017103_07		
FRT000174F4_07		
FRT0001821C_07		
FRT00018524_07		

New Mg-Carbonate Detections	New Talc/Saponite Detections	New Serpentine Detections
FRT000186FA_07		
FRT00021F08_07		
FRT00023565_07		
FRT00023728_07		
FRS00029EEC_01		
FRS0002AE17_01		
FRS0002B2F2_01		
FRS0002BA97_01		
FRS0002FE75_01		
FRS00031260_01		
FRS00031442_01		
FRS00036666_01		
FRS00037F03_01		
HRL00006408_07		
HRL000086CA_07		
HRL0000A8EC_07		
HRL0000AB0A_07		
HRL0000CC16_07		

Table 5.19. CRISM sample and line numbers for spectra shown in **Figure 3.9** and **Figure 3.10**.

FIGURE Number	**CRISM Image ID**	**Label**	**Numerator (column; row)**	**Denominator (column; row)**
3.9	FRT00003E12_07	Olivine-rich	(133-137; 274-278)	(133-137; 258-262)
		Mg-carbonate-bearing	(136-140; 103-107)	(136-140; 211-215)
	FRT0000ABCB_07	Mg-serpentine-bearing	(253-257; 60-62)	(253-257; 17)
	FRT0000A053_07	Talc/saponite-bearing	(104-108; 409-413)	(104-108; 416-421)
3.10	FRS0002AE17_01	CRISM Talc	(151-156; 175-181)	(151-156; 155-147)
		CRISM Serpentine	(79-82; 129-131)	(79-82; 142-143)
		CRISM Carbonate	(489-497; 120-126)	(489-497; 107-113)

Table 5.20. Reference Spectra for Library Spectrum for **Figure 4.1**

Endmember	**Reference**	**Sample ID**
Serpentine	Bishop et al., 1995	LACR01
Talc	JPL/ASTER Spectral Library	PS-14A
Saponite	Bishop et al., 1995	LASA51
Mg-Carbonate	Mustard and Pieters, 1989	CACB06
Ca-Carbonate	Mustard and Pieters, 1989	E95-15A
Fe-Carbonate	Mustard and Pieters, 1989	CBCC07

VITA

Elena Sophia Amador

Esamador (at) uw.edu
(831) 295-1117

Education

Ph.D. in Earth and Space Sciences and Astrobiology
University of Washington (UW) (2017)
Dissertation: *Characterizing Habitable Environments on Mars using Infrared Spectroscopy From Orbit*

B.S. in Earth and planetary sciences, concentration in planetary sciences, **minor** in astrophysics
University of California, Santa Cruz (2010)

Grants

2016-2020	**NASA Planetary Science and Technology Through Analog Research (Co-I)** *Field Exploration and Life Detection Sampling for Planetary and Astrobiology Research (FELDSPAR)*; current
2014-2015	**NASA Mars Data Analysis Program (Student Co-I)** *Integrated Analyses of Martian Surface Compositions Using Near-Infrared through Thermal-Infrared Spectroscopic Data*; past
2013	**American Philosophical Society Lewis and Clark Fund for Research (PI; $5 K)** *Towards Revealing the Habitability, Productivity, and Microbial Diversity of Icelandic Lava Fields: An Interdisciplinary Approach*

Manuscripts in Preparation

Amador, E.S., Bandfield, J.L., and N.H. Thomas. A search for minerals associated with serpentinization across Mars using CRISM spectral data, *Icarus*

Salvatore, M.R., Goudge, T.A., Bramble, M.S., Edwards, C.S., Bandfield, J.L., **Amador, E.S.,** Ehlmann, B.L., Mustard, J.F., and P.R. Christensen, Bulk mineralogy of the NE Syrtis and Jezero crater regions of Mars derived through thermal-infrared spectral analyses, *Icarus*

Manuscripts in Review/Revision

Amador, E.S., Bandfield, J.L., Brazelton, W.J., and D.S. Kelley. The Lost City Hydrothermal Field as a spectroscopic and astrobiological Analog for Nili Fossae, Mars, *Astrobiology*, **in revision.**

Gentry, D.M., **Amador, E.S.,** Cable, M.L., Chaudry N., Cullen, T., Jacobsen, M.B., Murukesan, G., Schwieterman, E.W., Stevens, A.H., Stockton, A., Tan, G., Yin, C., Cullen, D.C., Geppert, W., Correlations between life-detection techniques and implications for sampling site selection in planetary analogue mission, *Astrobiology*, **in revision.**

Cloutis, E.A., Jonatanson, V., Bandfield, J.L., **Amador, E.S.,** Rivera-Hernández, F., Mann, P., and S.A. Mertzman, Hydrothermally-altered dacite terrains in the Methana peninsula Greece: Relevance to Mars, *Planetary and Space Sciences,* **in revision.**

Published Manuscripts

Amador, E.S., and J.L Bandfield, Elevated bulk-silica exposures and evidence for multiple aqueous alteration episodes in Nili Fossae, Mars, *Icarus*, doi:10.1016/j.icarus.2016.04.015, 2016.

Bandfield, J.L. and **E.S. Amador**, Extensive aqueous deposits at the base of the dichotomy boundary in Nilosyrtis Mensae, Mars, Icarus, doi: 10.1016/j.icarus.2016.04.002, 2016.

Amador, E.S., et al., Synchronous in-field application of life detection techniques in planetary analog missions. *Planetary and Space Science*, http://dx.doi.org/10.1016/j.pss.2014.11.006, 2014.

Bandfield, J.L., **Amador, E.S.**, and N. Thomas. Extensive Hydrated Silica Materials in western Hellas Basin, Mars, *Icarus*, 10.1016/j.icarus.2013.08.005, 2013.

McKeown N., Bishop J., Cuadros J., Hillier S., **Amador E. S.**, Makarewicz H., Parente M., and E. Silver. Interpretation of Reflectance Spectra of Clay Minerals- Silica Mixtures: Implications for Martian Clay mineralogy at Mawrth Vallis, *Clay and Clay Minerals*, 2011.

Oral Presentations

Invited

2017 Searching for habitable environments on Mars: Using Serpentinization as a Tracer. Western Washington University, Department of Geology Colloquium, Jan. 10, 2017.

2016 Spectral Evidence for Serpentinization on Mars: Implications for Habitability. Centro de Astrobiologia, Madrid, Spain, Sept. 23, 2016.

2015 What can the surface of Mars tells us about ancient habitability? University of Washington, NASA Space Grant Research Seminar, May 1, 2015.

2014 Water and Weathering Profiles on Mars: Implications for Ancient Habitability. University of Washington, Department of Forestry Water, Soils and Watersheds Seminar, Jan. 10, 2014

Conferences

2016 The Lost City Hydrothermal Field: A Spectroscopic and Astrobiological (?) Analog for Nili Fossae, Mars. 4th International Serpentine Days Conference, Sete, France.

2016 Spectral Characteristics of Dark Slope Streaks on Mars: A Global Survey with CRISM. Lunar and Planetary Science Conference, XLVII, 2696.

2014 Alteration of Olivine-rich Basalts on Mars: A THEMIS/CRISM Joint Investigation. Lunar and Planetary Science Conference, XLV, 1521.

2013 The Lost City Hydrothermal Field: A Spectroscopic and Astrobiological Analog for Nili Fossae Mars. Lunar and Planetary Science Conference, XLIV, 2742.

2012 Elevated Bulk Silica Deposits in Nili Fossae, Mars: Implications for Habitability. Astrobiology Science Conference, Atlanta, Georgia.

Conference Poster Presentations

2015 Localized Alteration of the Capping Unit in Nili Fossae, Mars: Evidence for Multiple Episodes of Aqueous Alteration. Lunar and Planetary Science Conference XLVI, 1189.

2012 Elevated Bulk Silica Compositions Associated with Olivine-rich Basalts in Nili Fossae, Mars. Lunar and Planetary Science Conference XLIII, 2508.

2011 Mars Aqueous Mineralogy: A Comparison of Thermal Infrared and Visible/Near-Infrared Spectral Data. European Space Agencies: Exploring Mars Habitability, Lison, Portugal

2010 Regional Mapping and Spectral Analysis of Mounds in Acidalia Planitia, Mars. Lunar and Planetary Science Conference XLI, 1037.

2009 Detection of Kaolinite at Mawrth Vallis, Mars: Analysis of Laboratory Mixtures and Development of Remote Sensing Parameters. Lunar and Planetary Science Conference XXXX, 2188.

Honors and Awards

2016 David A. Johnston Award for Research Excellence presented by the Dept. of Earth and Space Sciences, University of Washington, $5,000.

2016 SETI Institute and NASA Astrobiology Institute Travel Award, $600.

2016	Best Overall Planetary or Space Science Presentation at the ESS Dept. Gala, $250.
2015	Distinguished Graduate Student Research Fellowship presented by the UW Earth and Space Science Department, 1 quarter RA.
2014	Distinguished Graduate Student Research Fellowship presented by the UW Earth and Space Science Department, 1 quarter RA.
2014	Lunar and Planetary Institute's Career Development Award, $1,000.
2013	Stephen E. Dwornik Award for "Best Graduate Oral Presentation" presented by the Planetary Geology Division of the Geological Society of America at LPSC XLIV, $500.
2013	Geochemical Society Student Travel Grant to 2013 Goldschmidt Conference, Florence, Italy, $1,400.
2013	Best Overall Oral Presentation presented by the UW Earth and Space Sciences Dept. Research Gala, $200.
2012	*Coombs Fellowship* presented by UW Earth and Space Sciences Department, 1 quarter RA.
2012	Chevron Graduate Field Support Award
2012	NSF Graduate Research Fellowship, *Honorable Mention.*
2011	NSF Graduate Research Fellowship, *Honorable Mention.*
2011	*Best Research Poster in Climate, Planets and Space* presented by the UW Earth and Space Sciences Department, $100.
2010	NSF IGERT *Astrobiology Research Fellow,* 1 year RA.

Teaching and Professional Experience

2016	Teaching Assistant, ASTROBIO 115, "Introduction to Astrobiology", UW
2016	Teaching Assistant, ESS 421, "Introduction to Remote Sensing", UW
2015	Field Instructor, Nordic-NASA Astrobiology Summer School, Iceland
2012	Teaching Assistant, ESS 421, "Introduction to Remote Sensing", UW
2009	Lunar and Planetary Institute Intern, NASA Johnson Space Center under Dr. Carl Allen and Dr. Dorothy Oehler
2008-2010	Undergraduate Research Assistant, SETI Institute under Dr. Janice Bishop

Workshops Attended

2014	Jet Propulsion Laboratory's Planetary Science Summer School
2012	Nordic-NASA Summer School *"Water, Ice and the Origin of Life in the Universe".*
2011	NAI and Centro de Astrobiologia, Madrid, Spain Astrobiology Summer School "*Mars Exploration: Unveiling a Habitable Planet".*

Academic Service and Leadership

2016	Workshop Organizer for UW Astrobiology Workshop to Mt. Rainier. "Life Detection Techniques in Analog Field Environments". September 2016
2015	Executive Secretary, NASA Solar System Workings Panel
2014	Executive Secretary, NASA PDART Panel
2014	Executive Secretary, NASA PSTAR Panel
2013/14	Graduate Student Representative to the Faculty, UW Earth and Space Sciences Department
2011-	Science Communications Fellow**,** Pacific Science Center, Seattle, WA